Calibration of NGA-East GMMs and Site Amplification Models Against CENA Ground Motions

A report on collaborative research by the University of California, Los Angeles, University of Illinois, Urbana-Champaign, and University of Texas that was supported by the USGS External Research Program under contract numbers

G21AP10370 (University of California, Los Angeles)
G21AP10368 (University of Illinois)
G21AP10367 (University of Texas)

Dylan Centella, University of Illinois, Urbana Champaign

Meibai Li, University of Texas, Austin (now at UCLA)

María E. Ramos-Sepúlveda, University of California, Los Angeles

Okan Ilhan, Ankara Yildirim Beyazit University, Türkiye

Youssef M.A. Hashash, University of Illinois, Urbana Champaign

Ellen M. Rathje, University of Texas, Austin

Jonathan P. Stewart, University of California, Los Angeles

September 30, 2023

Abstract

This collaborative project investigates bias in earthquake ground motions predicted for Central and Eastern North America (CENA) using the Next Generation Attenuation-East (NGA-East) ground motion models and site amplification models. Model development in NGA-East project included two components: (1) earthquake ground motion models (GMM) that predict the median and aleatory variability of various intensity measures conditioned on magnitude and distance, derived for a reference hard-rock site condition with an average shear-wave velocity in the upper 30 meters (V_{S30}) = 3000 m/s; and (2) site amplification model that modify intensity measures for softer site conditions. Bias is anticipated because of the de-coupled procedures used in the development of NGA-East GMMs and site amplification models. In particular, the NGA-East GMMs were calibrated by correcting CENA data to a reference site condition using a site amplification model appropriate for active tectonic regions (such as California), which is different than the site amplification model that was ultimately recommended for CENA (Stewart et al. 2020). The NGA-East site amplification model recommended for hazard applications is not known to be biased, but a term in this model (denoted F_{760}) for amplification between the reference condition and V_{S30}=760 m/s has substantial uncertainty and has to this point not been calibrated against data.

Using the NGA-East database supplemented with ground motions from recent earthquakes and recently-obtained site condition data, we establish the period-dependent bias of NGA-East GMMs when applied in combination with the CENA site amplification model. Moreover, to enable appropriate partitioning of the bias (i.e., model adjustment), we perform data-driven and simulation-based investigations of amplification for 760 m/s sites to better constrain the F_{760} component of the site amplification model.

For the bias analysis, we compute residuals using 17 NGA-East GMMs and three data selection criteria. Mixed-effects regression of the residuals reveals a persistent pattern of bias in which ground-motions are overpredicted at short periods (0.01 to 0.6 sec, including PGA) and underpredicted at longer periods. The bias varies regionally, particularly in Texas-Oklahoma-Kansas, which has larger absolute biases than other parts of CENA. Two factors potentially influencing the bias are: (1) differences in the site amplification models used to adjust the data to the reference condition during NGA-East GMM development relative to current CENA amplification models, and (2) potential bias in F_{760}. We provide bias adjustment factors and their epistemic uncertainties, as well as provide recommendations for their application.

A data-driven assessment of F_{760} for the Texas, Oklahoma, and Kansas (TOK) region was undertaken based on analysis of recordings from recent earthquakes. The TOK region has seen significant seismicity over the last 10+ years, and the site conditions are dominated by moderate to larger V_{S30} (~600-1000 m/s). We compute residuals relative to the weighted median NGA-East GMM for the reference condition of V_{S30} = 3000 m/s. Mixed-effects regression of the residuals is used to develop region-specific adjustments for magnitude, distance, and site effects. After applying these adjustments, the overall bias shows systematic overprediction of ground motions at periods less than 0.1 sec and underprediction at longer periods. The levels of bias for TOK are

generally much larger (as absolute values) than those for the overall CENA region. The bias at short periods suggests a fundamentally different spectral shape that is consistent with a high-frequency spectral decay parameter (κ_0) between 0.01 and 0.03 sec. The significant bias at long periods is too large to be solely attributed to differences in the site amplification models, and may reflect issues with **M** determination and magnitude scaling in the NGA-East GMM.

A suite of 30 simulation-based F_{760} models is developed based on linear elastic, equivalent linear and nonlinear one-dimensional (1D) site response analyses (SRA) using (1) generic site profiles developed as part of a large-scale parametric study for CENA and (2) measured profiles at sites in the Texas, Oklahoma, and Kansas (TOK) region. For the first set of profiles, those with V_{S30} values between 700-800 m/s are selected to develop F_{760} models, and for the TOK profiles, V_{S30} range is between 600 m/s and 900 m/s. Two values of small-strain damping parameters or high-frequency spectral decay parameter (κ_0) are considered, (a) κ_0 < 0.01 s as used in prior studies, and 0.01 s< κ_0 <0.05 s, based on TOK data. A total of 6 F_{760} weighted models are then developed based on grouping by κ_0 (4 models, κ_0 < 0.01 s, κ_0 ≈ 0.01 s, κ_0 ≈ 0.02 s, κ_0 ≈ 0.03 s) and by impedance versus gradient Vs profiles (2 models). The gradient F_{760} model exhibits higher amplification between T ≈ 0.025 s and T ≈ 0.45 s, and lower amplification at long periods (> 0.5 s) compared to previously published gradient model. The impedance F_{760} model is similar to the prior F_{760} impedance model, but is slightly smaller at some short periods and larger at long periods.

Acknowledgements

Funding for this study was provided by the US Geological Survey under contract numbers G21AP10370 (UCLA), G21AP10368 (University of Illinois), and G21AP10367 (University of Texas). Partial support for the first three authors was also provided by the University of Illinois, University of Texas, and UCLA.

This support is gratefully acknowledged. The work presented here represents the views and opinions of the authors and does not reflect the policy, expressed or implied, of the US Government.

Helpful input was received during the project from Grace Parker, Eric Thompson, Scott Brandenberg, Tristan Buckreis, Christine Goulet, and journal paper reviewers: Sanaz Rezaeian, Behzad Hassani, Norman Abrahamson, and one anonymous reviewer, whose comments helped us improve the technical content and the clarity of presentation.

Contents

List of Tables

List of Figures

1 Introduction

1.1 Background

In the 2018 U.S. Geological Survey (USGS) National Seismic Hazard Model (Petersen et al., 2020), ground-motion intensity measures for central and eastern North America (CENA) were evaluated using ground motion models (GMMs) and site amplification models developed as a part of the Next Generation Attenuation-East (NGA-East) project (Goulet et al. 2021a; Youngs et al. 2021). These GMMs and site amplification models were developed by different teams of investigators and under different organizational frameworks. In the case of GMMs, 17 models and a weighted median (referred to as "central branch" below) were recommended by Goulet et al. (2021a) with the aim of capturing epistemic uncertainties related to the overall ground-motion space, including magnitude scaling, distance scaling, and other attributes. These recommended GMMs do not include individually developed "seed" GMMs by independent modelers (Pacific Earthquake Engineering Research Center, 2015; hereafter PEER 2015), although some of those seed models are considered in the NSHM (Rezaeian et al. 2021), as those GMMs were argued to represent physical features that were not present in the 17 NGA-East models. The GMMs apply for a hard-rock reference site condition defined as having average shear-wave velocity in the upper 30 meters V_{S30} = 3000 m/s and site decay parameter (κ_0) of 0.006 sec (Hashash et al. 2014) which is often used as the reference site condition for applications in which site-specific site response is applied. The model development was conducted as a Senior Seismic Hazard Analysis Committee (SSHAC) Level 3 project (Budnitz et al. 1997; Nuclear Regulatory Commission 2012), which is a formal process involving extensive review and documentation.

Because of the hard-rock reference site condition, development of the seed GMMs required adjustments to be made to recorded ground-motions in the NGA-East database (Goulet et al. 2021b), all of which were from sites with softer-than-reference site conditions (average shear-wave velocities in the upper 30 meters, V_{S30} ~150 to 2000 m/s). The adjustments occurred relatively early in the project (Pacific Earthquake Engineering Research Center, 2015), generally using V_{S30}-based site amplification models for active tectonic regions. The adjusted ground-motions were used in GMM development as a constraint on scaling relations (with distance and magnitude), but also to set constant terms in the models that control the overall model amplitudes. The GMM developers realized that the V_{S30}-scaling models could be in error (e.g., C. Goulet, personal communication, 2023), and it was later demonstrated by Hassani and Atkinson (2017), Parker et al. (2019), and Boore (2020) that CENA has weaker V_{S30} scaling (i.e., smaller slope in absolute value terms), which means that V_{S30} has less predictive power in CENA than in active regions.

The site amplification models used in the 2018 NSHM for CENA were developed by an expert panel based on a synthesis of available research (Stewart et al. 2020; Hashash et al. 2020). This synthesis drew heavily upon research products from the NGA-East Geotechnical Working Group (GWG) (Parker et al. 2019; Harmon et al. 2019a,b). The GWG site amplification model development was reviewed extensively but this occurred outside of the NGA-East SSHAC process. The GWG site amplification models (F_S) are intended to represent site amplification

relative to V_S = 3000 m/s and κ_0 = 0.006 sec. The reference condition was not defined relative to the NGA-East GMMs; hence, if the GMMs are biased with respect to the assumed reference condition, that bias would propagate through the GWG site amplification model when used with the NGA-East models to predict ground-motions at other V_{S30} values.

The model has a linear (F_{lin}) and nonlinear (F_{nl}) component:

$$F_S = F_{lin} + F_{nl} \quad (1.1)$$

The linear component of the model has two terms:

$$F_{lin} = F_V + F_{760} \quad (1.2)$$

where F_V describes the scaling of ground-motion with V_{S30} relative to V_{S30}=760 m/s and F_{760} describes the amplification of ground-motions for 760 m/s sites relative to 3000 m/s sites. F_{760} carries significant parametric uncertainty in κ_0 due to the lack of empirical data at the reference site condition (e.g., Atkinson, 2012; Boore and Campbell, 2017) and the assumption that κ_0 reflects only material damping (Al Atik et al. 2022). Two components are used in Eq. (1.2) because they were derived using different procedures. F_V is empirically constrained from NGA-East data (Parker et al., 2019), while F_{760} is derived from ground response simulations (Frankel et al., 1996; Silva et al., 2015; Boore and Campbell, 2017; Harmon et al., 2019a,b). This two-tier approach was required because it was not possible to empirically derive site amplification relative to 3000 m/s conditions.

1.2 Project Need

Because the site adjustments applied during GMM development used a modeling approach different from how the NGA-East GMMs are now applied, this study was undertaken to assess whether the combined use of NGA-East GMMs and site amplification models has biases for the region as a whole as well as a portion of the region with a high concentration of recent events induced by resources extraction related activities (Texas-Oklahoma-Kansas, hereafter denoted TOK). Such biases, if present, are important to characterize for seismic hazard analyses in these regions.

1.3 Project Overview

This collaborative project consisted of three sets of coordinated research tasks. The first set of tasks entailed expanding the ground-motion database for CENA relative to NGA-East (Goulet et al. 2021b), making this data publicly available, performing residuals analyses to assess model performance for the broader CENA region, and providing a model for bias removal. The second set of tasks focused on data compilation and analysis within the TOK region with the aim of identifying regional features of ground-motions from the induced events that occur there. This work used an expanded data set (relative to the publicly accessible CENA-wide dataset), applied some different metadata protocols, and produced adjustment factors to the NGA-East central branch model related to bias and distance-scaling. The third set of tasks focused on improved

simulations to evaluate the F_{760} component of the model (Eq. 1.2), including compilation of profiles with V_{S30} near 760 m/s, ground response analyses of those profiles, and engineering assessments of mean results and their regional variations.

Chapter 2 of this report describes the processing of ground-motions performed as part of this study, both CENA-wide and for the TOK region. Chapter 3 describes the metadata compilation and the relational database in which the data has been organized and through which public access is facilitated. Chapter 4 discusses the analyses of CENA-wide model bias, including consideration of regional variations for TOK and coastal plain regions. Chapter 5 discusses the TOK-specific data analyses, including results demonstrating different path and bias effects. Chapters 6 and 7 describe the data collection and simulations for F_{760} and provide recommendations for adjustments of this parameter.

2 Ground-Motion Processing

2.1 Processing Procedures

2.1.1 NGA/PEER Procedures

The Next Generation Attenuation (NGA) program developed a manual method to systematically process ground-motions, with the most recent procedures described by Goulet et al. (2021b) and Kishida et al. (2020). This procedure was coded into R and required visual inspection to screen waveforms, indicate wave arrivals and select corner frequencies. This process is time-intensive and subjective since it depends on manual inspection. The steps are listed below with a brief description.

1. Screening of time series to select which ground-motions will be processed: This step relies on visual inspection and judgment. Records with indiscernible p- or s-wave (indicator that noise prevails over the ground-motion signal) are rejected. Furthermore, any odd shapes like spurious spikes, multiple arrivals, and gradual intensity increase outside the p- or s-wave windows are rejected. At least 2 horizontal components are needed.
2. Application of window functions that will reduce the intensities down to zero outside of the range of time of interest: The p-wave arrival, as well as the s-wave arrival, are selected manually by the user based on their visual inspection and judgment of the time series. The duration of each window will depend on different models and assumptions (Kishida et al., 2020).
3. Computation of Fourier amplitude spectra (FAS)
4. Corner frequency selection to filter-out noise-dominated features: The selection of high-pass corner frequency (f_{cHP}) is informed by multiple criterias and ultimately chosen based on the user's judgment. The initial guess of the f_{cHP} is based on the theoretical acceleration decay at low frequency, f^2 model (Brune, 1970; Boore and Bommer, 2005), which prevents the f_{cHP} to be located where the FAS ordinates have an average slope of zero. Also taken into consideration is the FAS ratio of the entire signal to the noise window (i.e., signal to noise ratio, SNR). The typical threshold value of SNR used in practice is 3. Additionally, the waveforms are evaluated to make sure no unphysical displacements or unusual long-period fluctuations (referred to as "wobble" herein) are present (Boore and Bommer, 2005). If wobble is observed, the user goes back, chooses a higher f_{cHP} and evaluates the displacement again. The user continues this iterative process until the displacement waveform seems acceptable to the user's judgment. The low-pass corner frequency (f_{cLP}) is selected based on various conditions as well. The f_{cLP} is not needed if the ratio between the maximum FAS and the FAS at the 75% of the Nyquist frequency is greater than 10 (Douglas and Boore, 2011). If a f_{cLP} is needed, it must fall in FAS ordinates with negative slope and the SNR should be greater than 3.

5. Apply a baseline correction: The acceleration is integrated in the time domain (Nigam and Jennings 1969) to obtain velocity and integrated a second time to obtain displacement, with initial values assumed to be zero. The baseline drift that is sometimes encountered by assuming initial values of zero is later corrected with the baseline correction procedure explained in Boore et al., 2012.

2.1.2 USGS gmprocess

Originally, the ground-motion data utilized in this project was going to be processed following the procedures developed for the NGA projects and using the recommended R tools. Nonetheless, the number of records exceeded 73,000 and the time needed to manually process these records could have compromised the completion of the project during the contract period. Therefore, implementing an automated code was considered. The U.S. Geological Survey (USGS) developed an open-source software, gmprocess (Hearne et al., 2019), to facilitate repeatable and rapid automated ground-motion processing while following the standards of NGA's procedure. The nature of the manual procedure (i.e., rely on human judgment) became a challenge in the automatization, resulting in differences in the selection of filter corner frequencies, window durations, and p-wave arrival times (Rekoske et al., 2020). Differences relative to the NGA procedure are explained below.

Difference to step # 1: Time series are first screened to ensure they meet the following configurable requirements: (1) free-field stations, (2) a minimum of two horizontal components, (3) minimum sampling rate of 20 Hz, (4) minimum of 0.1 zero crossings per second after demeaning the raw time series, and (5) SNR must be greater than 3 from the Brune (1970) corner frequency to 5 Hz.

Difference to step # 2: The p-wave arrival is estimated from a travel-time calculation using the velocity model of Kennet et al. (1991). The signal window duration is estimated as the mean plus two standard deviation 5-95% significant duration from Afshari and Stewart (2016), and 60 seconds of pre-event noise is included for the purpose of computing SNR.

Difference to step # 4: By default, f_{cHP} is set as the lowest frequency where SNR = 3. This is configurable and other methods were also available (e.g., Dawood et al., 2016), but ultimately deemed deficient and were not considered in this study. For f_{cLP}, the options are either not applying a f_{cLP} value or choosing the minimum between SNR = 3 and the 75% of the Nyquist frequency.

2.1.3 Revisions to gmprocess

An important aspect of NGA processing that is not included in previous versions of gmprocess is the inspection for displacement wobble. In this section, we present the procedures adopted to address this issue, which are now implemented in an updated version of gmprocess. These procedures have previously been presented by Ramos-Sepulveda et al. (2023a).

The default algorithm to select f_{cHP} in gmprocess is based solely on the SNR. It sets f_{cHP} equal to the lowest frequency where the SNR exceeds a threshold, generally set equal to 3. Figure 2.1 shows an example ground-motion where SNR criteria produce a low f_{cHP} of 0.013 Hz. Panel (a) depicts the location of the f_{cHP} with respect to the FAS of the unfiltered record (signal), pre-event signal (noise), and the SNR. Panel (b) shows the displacement time series with wobble after filtering. Similar results were found for various records, and show that SNR-only criteria do not always remove low-frequency noise adequately. Additional adjustments were needed to remove undesired artifacts in the displacement record.

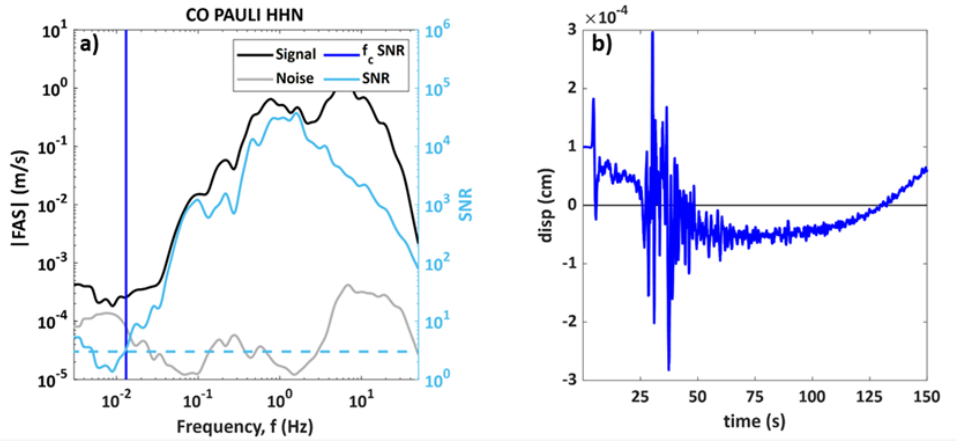

Figure 2.1 Example record in which SNR-only criteria for selecting fcHP produce displacement wobble: (a) FAS and SNR, (b) displacement time series after high-pass filtering at fcHP.

A displacement polynomial fit method was developed to first selects a trial f_{cHP}, filter the record, compute the displacement time series, fit a polynomial (with configurable order; 3th order is used herein) to the filtered displacement record, and iterate on f_{cHP} until the ratio of the polynomial fit maximum amplitude to that of the displacement record matches a specified target within a tolerance. Iterations are performed using Ridders' (1979) method. The procedure is illustrated in Figure 2.2 using a target of 0.01 and tolerance of 0.001. These target and tolerance values were selected based on engineering judgment informed by application of the approach to recordings from multiple earthquakes. In panel (a) of Figure 2.2, the record is under-filtered because the amplitude ratio is larger than 0.01; in panel (b), the record is properly filtered because the amplitude ratio is 0.01; and in panel (c), the record is over-filtered because the amplitude ratio is smaller than 0.01. If these criteria are not met for $f_{cHP} < 0.5$ Hz within 30 iterations, the record is rejected. This iterative method is coded by Brandenberg and Yang (2022).

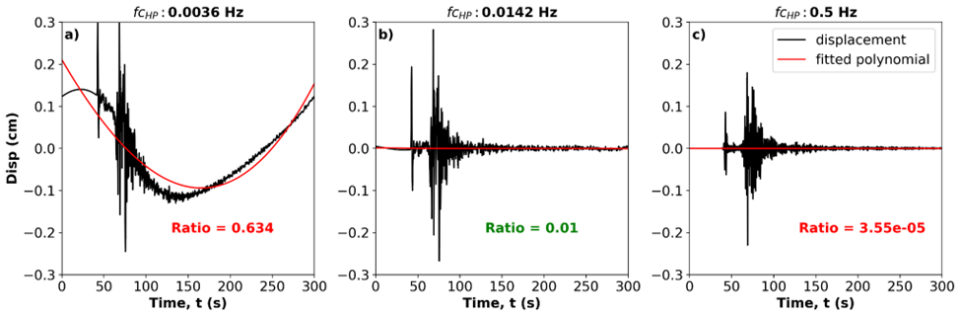

Figure 2.2 Processed displacement record with different f_{cHP} (increasing from left to right) along with the fitted polynomial and the corresponding maximum amplitude ratio for an under-filtered record (a), properly processed record (b), and over-filtered record (c).

In the gmprocess implementation of the polynomial fit method (merged into the repository on March 23 of 2022, and released in version 1.2.0), the baseline correction step prior to filter application consists only of a mean subtraction (i.e., a 0th order polynomial) rather than a higher-order polynomial subtraction as used for the SNR-only criteria. Moreover, the integration to velocity and displacement is applied in the frequency domain because time-domain integration utilizing zero initial velocity and displacement was found to introduce low-frequency artifacts into displacement traces, rendering artificially high polynomial fit amplitudes.

While the polynomial fit method can be applied in an automated mode in gmprocess (it is an option that can be selected in the configuration file – it must be deliberately selected by the user as the default criterion is SNR-only), we preferred to have human inspection of records to ensure that filtered records are reasonable with respect to FAS shape, Sa shape, and displacement wobble. These visual inspections check for the same features considered in NGA procedures (Section 2.2.1). To facilitate this checking, a GUI was developed by collaborator Scott Brandeberg that allows the salient features to be observed and for users to adjust f_{cHP} as needed. Once a record is approved, the GUI allows records to be saved in an .h5 file format that is compatible with the database discussed in Chapter 3. Figure 2.3 shows an example record as visualized in the GUI. This record has a high-pass corner frequency of 0.68 Hz and no low-pass filter.

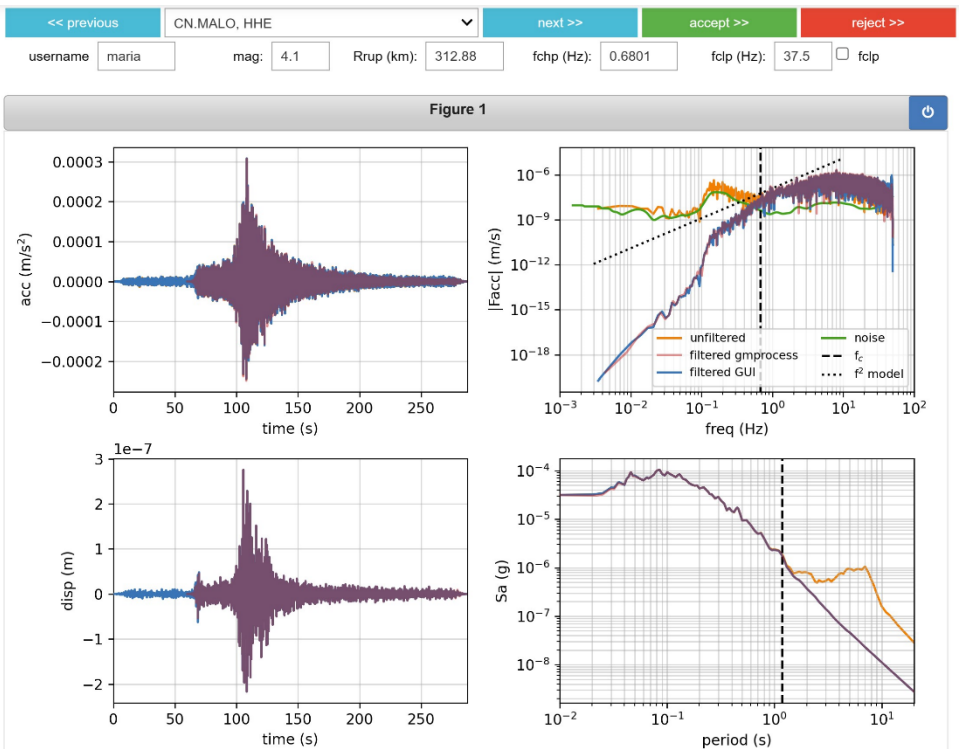

Figure 2.3 Processed ground-motion record as visualized in GUI developed to interact with gmprocess output. The left side of the figure shows three acceleration and displacement records – unfiltered (orange), filtered using automated routines in gmprocess (purple), and processed in the GUI (blue). The right side of the figure shows FAS (top) and Sa (bottom). Results are shown for the unprocessed, auto-procesed with gmprocess, and GUI-procesed, along with the noise spectra (green).

For the present application, gmprocess was configured so that no low-pass filtering was applied in the automated mode. When the record is checked in the GUI, no low-pass filter is applied when the response spectrum saturates to PGA and there are no unrealistic high-frequency spikes, for example as shown in Figure 2.3 (i.e., if the response spectra is flat at short periods). However, where such spikes occur, we low-pass filter with f_{cLP} taken as the smaller of $0.75 \times f_{Nyq}$ or the frequency where SNR =3. An example of this type of record is shown in Figure 2.4, where the Sa spike at about 0.02 sec (also visible as an FAS spike at 35-40 Hz) was removed with a 35 Hz low-pass filter.

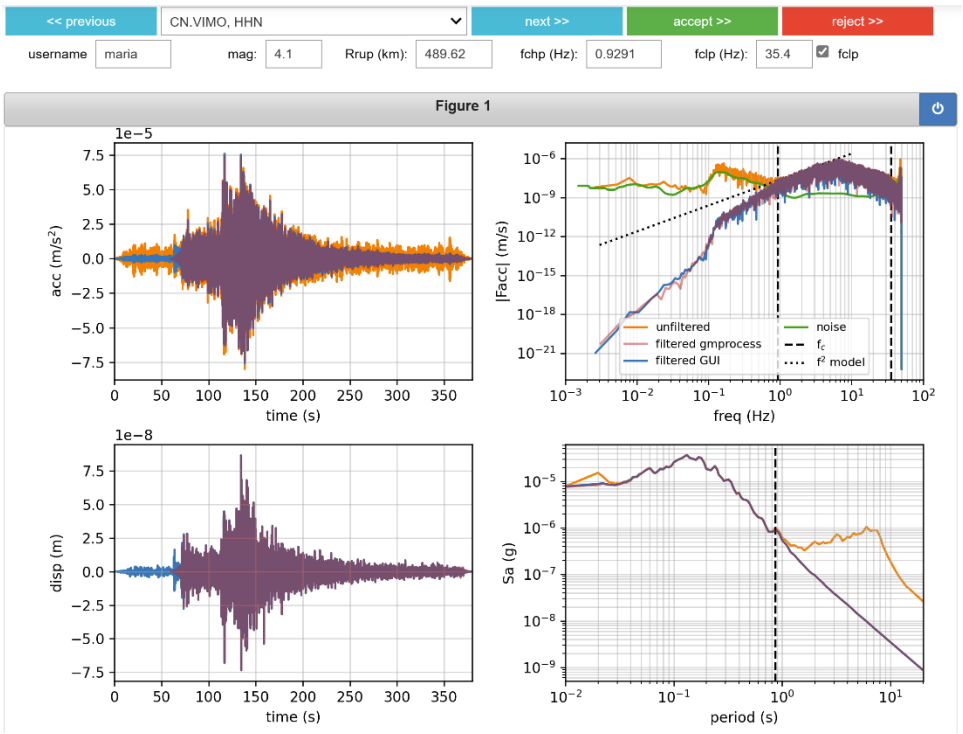

Figure 2.4 Processed ground-motion record, as visualized in GUI, in which a short-period Sa spike at 0.02 sec lead to the application of a low-pass filter.

2.2 Data Accessed

This report presents the results of a series of coordinated studies performed by different research groups. As a result, different databases were produced. One of the databases was developed to adhere, as closely as possible, with NGA procedures for data preparation and dissemination (e.g., as presented in Goulet et al. 2021b). That database was used for the research presented in Chapter 4 and is publicly accessible at Buckreis et al. (2023a). The second database was developed in a similar manner to prior work for Texas (Zalachoris and Rathje 2019) and is specific to that state along with Kansas and Oklahoma. While the procedures used in that data compilation are broadly similar to those used in NGA procedures, there are minor differences. The data are partially disseminated in tables, but the time series are not published and the data is not included in the national database of Buckreis et al. (2023a). This database was used for the work presented in Chapter 5.

Both databases include information from the Texas-Oklahoma-Kansas (TOK) region. The first database (used for Chapter 4) includes a few, essentially randomly selected, recent events in TOK. The second (used for Chapter 5) contains a larger and more complete TOK data compilation.

2.2.1 Expanded NGA-East Dataset

The database used in Chapter 4 is an expanded version of the NGA-East ground-motion database (Goulet et al., 2021b). The NGA-East portion of the database consists of ground-motion intensity measures and metadata (event locations, magnitude, distance, V_{S30}) provided in the electronic supplements to Goulet et al. (2021b). The NGA-East data were merged into a relational database developed for ground-motion studies (Buckreis et al., 2023a) and expanded to include events in CENA since November 2011 (date of the latest event in NGA-East). Complete data files, including intensity measures and site, path, and source metadata are provided in Ramos-Sepulveda et al. (2023b).

The database expansion considered all non-TOK events with moment magnitude $\mathbf{M} \geq 4$ in CENA from November 2011 to December 2022, based on event hypocenter locations east of the boundary between the active tectonic and stable continental regions as provided by Dreiling et al. (2014). This boundary has been recently updated (Moschetti et al., 2023) as shown in Figure 2.5. All of the events we processed remain within the updated region This comprises 187 earthquakes at the locations shown in Figure 2.5. Unprocessed ground-motions from these events were downloaded as miniseed files from IRIS (see Data Resources section). The number of records was over 73,111. The data were processed using the procedures described in Section 2.1 for low-frequency issues (high-pass corner frequency selection and baseline correction).

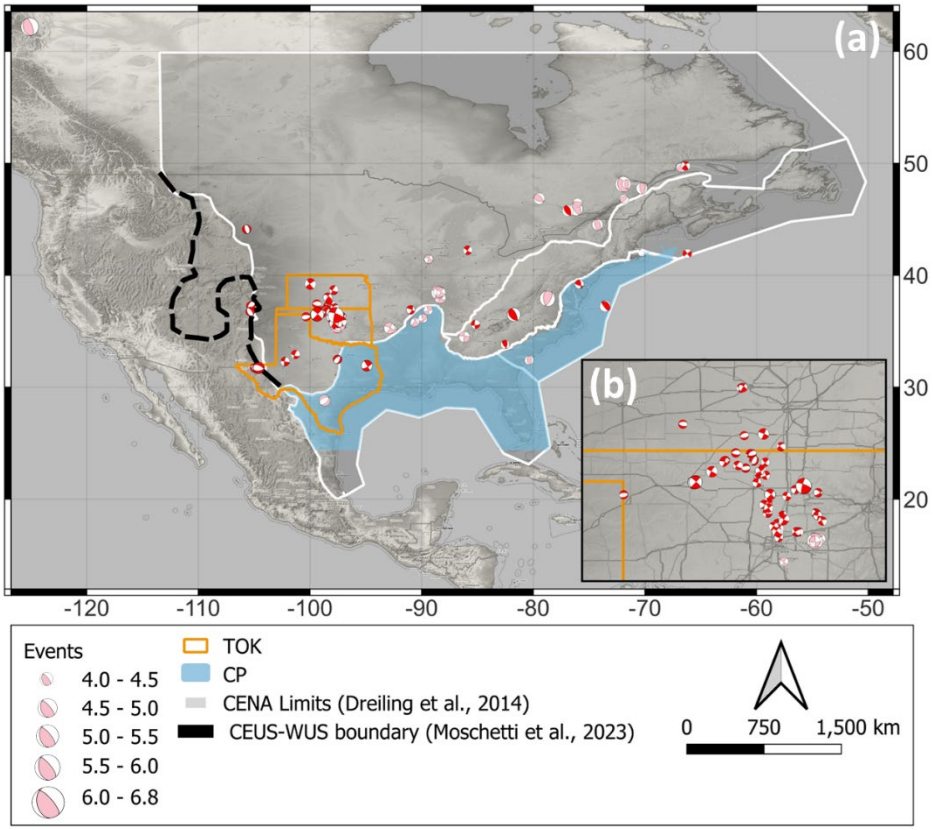

Figure 2.5 (a) Locations of CENA earthquakes and ground-motion recording stations considered in the present study. Boundaries of Texas-Oklahoma-Kansas (TOK) and coastal plain (CP) regions (Boyd et al., 2023) are shown. (b) Detailed view of Oklahoma where a high event density occurs. Pink symbols correspond to events documented by NGA-East while red symbols are newly added events.

The recent events typically have a greater density of recordings relative to the NGA-East events, which is a consequence of the growth of seismic instrumentation in CENA. The more recently installed instruments also have broader usable frequency ranges. Ground-motion intensity measures (peak ground acceleration, peak ground velocity, and response spectra from 0.01 to 10 sec) from these events and information on their component-specific usable frequency ranges were uploaded to the relational database.

Figure 2.6 shows data distributions as functions of rupture distance, V_{S30}, and **M**. The added data are mostly applicable for **M** < 5.1, rupture distance > 10 km, and V_{S30} = 200 to 2000 m/s. The new data significantly increases the number of recordings per event and per station relative to what was available from the original NGA-East database, although it does not extend the parameter range. This database expansion is useful in the context of the present study.

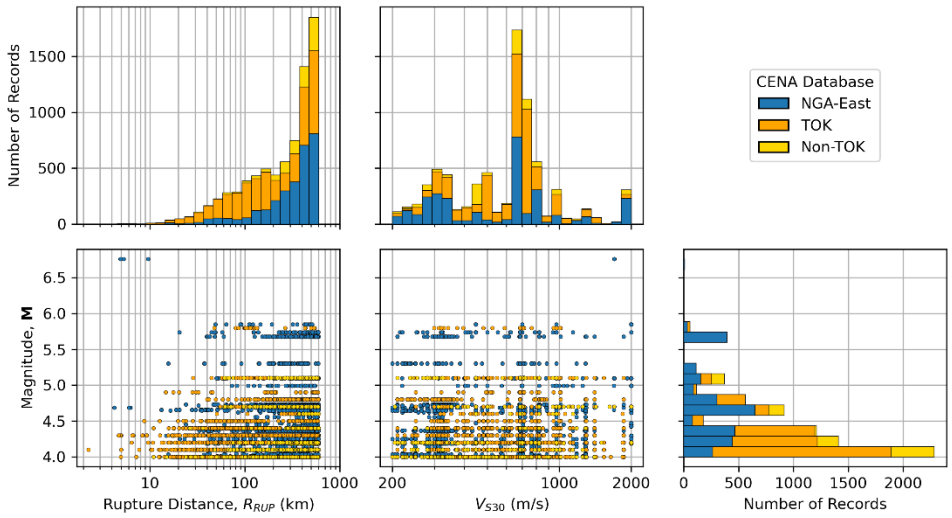

Figure 2.6 Distributions of CENA dataset with respect to rupture distance, V_{S30}, and magnitude, showing differences between NGA-East and added data.

Figures 2.7 and 2.8 depict the number of records and events as a function of oscillator period. The upper bound of the usable period range is set at $1/(1.25 \times f_{cHP})$. No lower limit on the period range is applied if a low-pass filter is not used and the Nyquist frequency is 40 Hz or greater. The rationale for this is that 40 Hz should be a fast enough sample rate to capture the effects of potential high-frequency features of ground shaking that might affect PGA. If a low-pass filter is applied, the lowest usable period was set as $1/(0.8 \times f_{cLP})$. If the Nyquist frequency is < 40 Hz and no low-pass filter is applied, the lowest usable period was set as $1/(0.8 \times f_{Nyq})$. As shown in Figures 2.7 and 2.8, the growth in database size at short periods is appreciable relative to NGA-East, which is mainly attributable to large numbers of recordings from recent events that have no need for a lowest usable period because of their relatively high Nyquist frequencies.

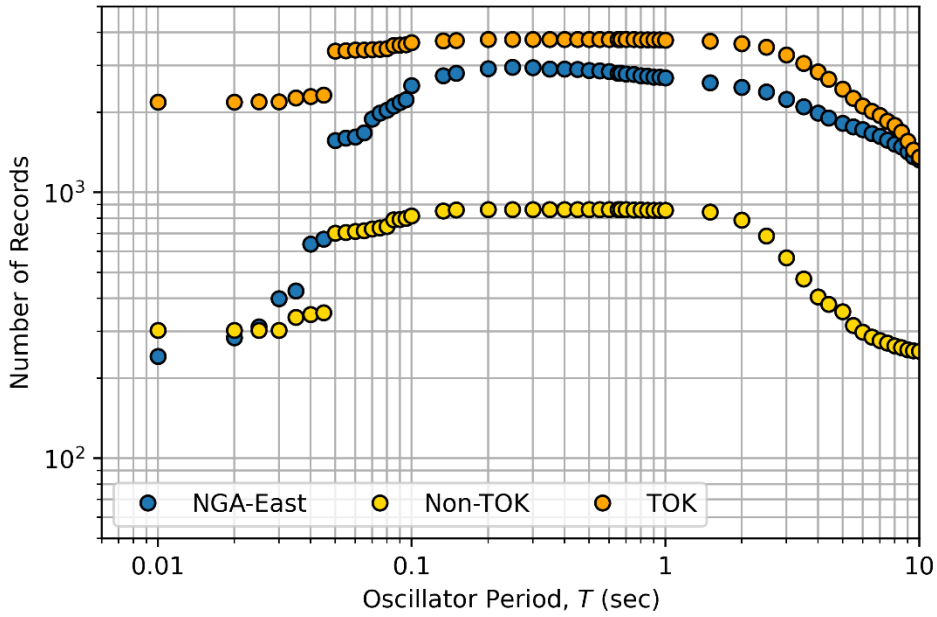

Figure 2.7 Distribution of ground-motion records within usable period range.

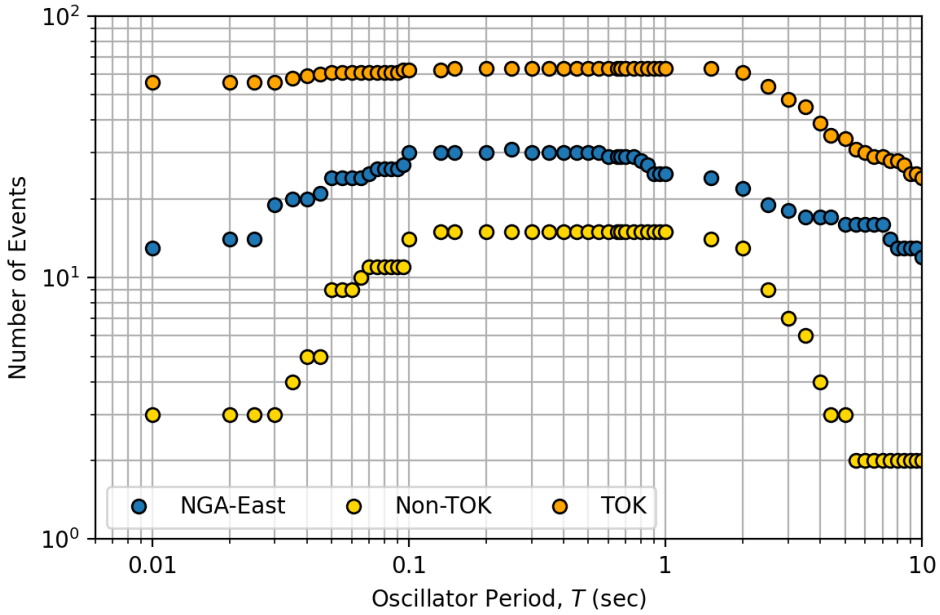

Figure 2.8 Distribution of events within the usable period range.

2.2.2 Dataset Exclusive to Texas, Oklahoma, and Kansas

Zalachoris and Rathje (2019) developed a GMM specifically for the observed and potentially induced seismicity in TOK. The GMM, denoted as ZR19, was developed using the reference empirical approach (Atkinson 2008) with the Hassani and Atkinson (2015, HA15) GMM for CENA

as the reference GMM. As part of the GMM building effort, a ground motion database of 4,528 earthquake ground motions recorded between January 2005 and November 2016 in TOK was established (Zalachoris and Rathje 2019). The database included the ground motion intensity measures of PGA, PGV, and 5% damped pseudo-acceleration (PSA) at periods between 0.05-10s for horizontal components of ground motion. With consideration of substantially different attenuation characteristics of the Gulf Coast Plain, the ground motions recorded by seismic stations within the Gulf Coast Plain were discarded. The boundary of the Gulf Coast Plain was defined based on Coleman and Cahan (2012). The data covered a moment magnitude range of **M** = 3.0-5.8 and a hypocentral distance range of 4-500 km.

We augmented the database by Zalachoris and Rathje (2019) with ground motions recorded in TOK between November 2016 and December 2022, and processed the recordings following a newly proposed automated data processing procedure, which makes use of the United States Geological Survey processing software, gmprocess (Hearne et al. 2019). The general approach described in Section 2.1 was used, except for a minor difference in that we chose to always apply the low-pass corner frequency as provided by the automated procedure of gmprocess. For the ground motion records obtained, the rotation-angle-independent ground motion intensity measures (RotD50, Boore 2010) were computed for the periods used in the NGA-East database (Goulet et al. 2021b) using the python package ucla_geotech_tools developed by Brandenberg and Yang (2021). This database was maintained as a separate series of files in the DesignSafe project (Li et al. 2023) from those for the broader CENA study (Section 2.2.1) and is not incorporated into the overall U.S. ground motion database of Buckreis et al. (2023a).

A detailed discussion of TOK data used for the analysis in TOK is provided in Chapter 5.

3 Metadata and Relational Database

3.1 Source Parameters

We assembled metadata describing the seismic sources, path, and site condition. General information such as the name and location of the instrument, hypocenter location, and event date and time were obtained from gmprocess. Newly added events include moment magnitudes from moment tensor solutions for 76 out of the 100 events, and magnitudes with their uncertainty were estimated for the remaining 24 events [NUREG-2115 (EPRI/DOE/NRC, 2012)]. If finite-fault models are not available for the event, a simulation procedure presented in Contreras et al. (2022) is used to generate approximate rupture dimensions based on magnitude, event type, hypocenter, and orientation of one or two nodal planes. Contreras et al. (2022) is a modification from a previous version presented by Chiou and Youngs (2008) which was modified even further to include the magnitude-area relationship specific to stable continental regions (Leonard 2014). The source parameters that were compiled for the general CENA database are provided in tables in Ramos-Sepulveda et al. (2023b).

For TOK, an event catalog was created for events occurring in TOK between January 2005 and December 2022. The catalog includes all events with reported magnitudes greater than 3.5 between January 2005 and February 2022, as well as events with reported magnitudes greater than 4.0 occurring between February 2022 and December 2022. The resulting catalog for TOK has 551 events in total, with 62.8% of these events having the moment magnitude reported, and the remaining events only have reported local magnitude (M_L), short-period body wave magnitude (M_b), or short-period surface wave magnitude (M_(b_Lg)). Ultimately, only events with reported moment magnitudes were used in our analysis, which resulted in a total of 346 events (62 events in Texas, 253 events in Oklahoma, and 31 events in Kansas).

3.2 Site Parameters

The data compilation described in Section 2.2 added 493 new ground-motion recording sites to the NGA-East dataset. The locations of the previous and newly added stations are shown in Figure 3.1.

For the CENA sites that are located outside of TOK, site parameters were derived from V_S profiles where available and otherwise from the Parker et al. (2017) geology-slope proxy. The V_{S30} measurements were obtained from the V_S profile database (Kwak et al. 2021). We re-examined the original NGA-East site catalog and re-assigned V_{S30} based on measurements for 5 sites. Ultimately, the number of sites with V_{S30} from V_S profiles is 71 (14%) for CENA (outside of TOK).

For the TOK sites, the V_{S30} obtained from measured V_S profiles is used where available, while for sites where measured V_{S30} is not available, proxy-based methods or the P-wave seismogram method are utilized. The V_{S30} measurements were obtained from a variety of sources, including Yust (2018), Stephenson et al. (2021), Mendoza et al. (2017), and EPRI (2013). With the exception of EPRI (2013), these V_S data have not been incorporated into the V_S profile database

of Kwak et al. (2021). The number of TOK sites with V_{S30} from V_S profiles is 79 (14%). We also considered the P-wave seismogram estimated V_{S30} by Zalachoris et al. (2017) and Tiwari (2018). A total of 149 stations (27%) have a P-wave seismogram estimated V_{S30} and the remaining 333 stations (59%) were assigned V_{S30} using a hybrid slope-geology based proxy (Li et al. 2022).

The P-wave seismogram estimated V_{S30} in TOK are validated using the dataset of V_{S30} measurements. A comparison of the V_{S30} for the 55 sites where both measured and P-wave estimates of V_{S30} are available is shown in Figure 3.2a. The residual of the P-wave estimated V_{S30} is computed as:

$$residual = \ln(V_{S30}^{mea}) - \ln(V_{S30}^{est}) \tag{3.1}$$

The mean and standard deviation of the residuals are 0.042 (~4% bias) and 0.365, respectively, suggesting that the P-wave seismogram approach provides reliable estimates of V_{S30}.

For TOK locations where neither measured nor P-wave seismogram estimated values of V_{S30} are available, we consider the hybrid slope-geology based proxy methods introduced by Li et al. (2022), which is developed using regional data from TOK. The proxy-based V_{S30} from Li et al. (2022) are compared to measurements at 79 sites where measurements are available, as shown in Figure 3.2b. The residuals are computed using Equation 3.1, and the mean and standard deviation of the residuals for the Li et al. (2022) proxy method are -0.102 and 0.314, respectively. These statistics indicate that the proxy-based V_{S30} is slightly more biased than the P-wave seismogram estimated V_{S30} (-0.102 vs. 0.042) but has smaller variability. The smaller standard deviation for the Li et al. (2022) method is likely due to its development using V_{S30} observations specific to TOK, which leads to region-specific observations such as the unique characteristics of Quaternary deposits outside of the Gulf Coast Plain.

It should be noted that Li et al. (2022) also produced a V_{S30} map of Texas, which was developed using geostatistical kriging integrated with the geologic proxy. We expect that the V_{S30} map gives more precise estimates of V_{S30} than the V_{S30} that is only based on the geology proxy, and thus we use the Li et al. (2022) map-based V_{S30} for sites inside Texas.

In summary, to assign V_{S30} values to the recording stations in the TOK dataset, we use the following protocols:

0. Assign a V_{S30} measurement wherever a measurement is available.

1. If a V_{S30} measurement is not available, assign P-wave seismogram estimated V_{S30} wherever a P-wave seismogram estimate is available.

2. If neither a V_{S30} measurement or P-wave seismogram estimate of V_{S30} is available, assign V_{S30} from the proxy methods by Li et al. (2022) for TOK sites and Parker et al. (2017) for non-TOK sites. If the site location is in Texas, assign the proxy V_{S30} using the geostatistical map-based V_{S30} of Li et al. (2022).

Li et al. (2023a) provides the V_{S30} values for each TOK station and the basis for their estimates. For the overall CENA database, the V_{S30} values are provided in a site table in Ramos Sepulveda et al. (2023b).

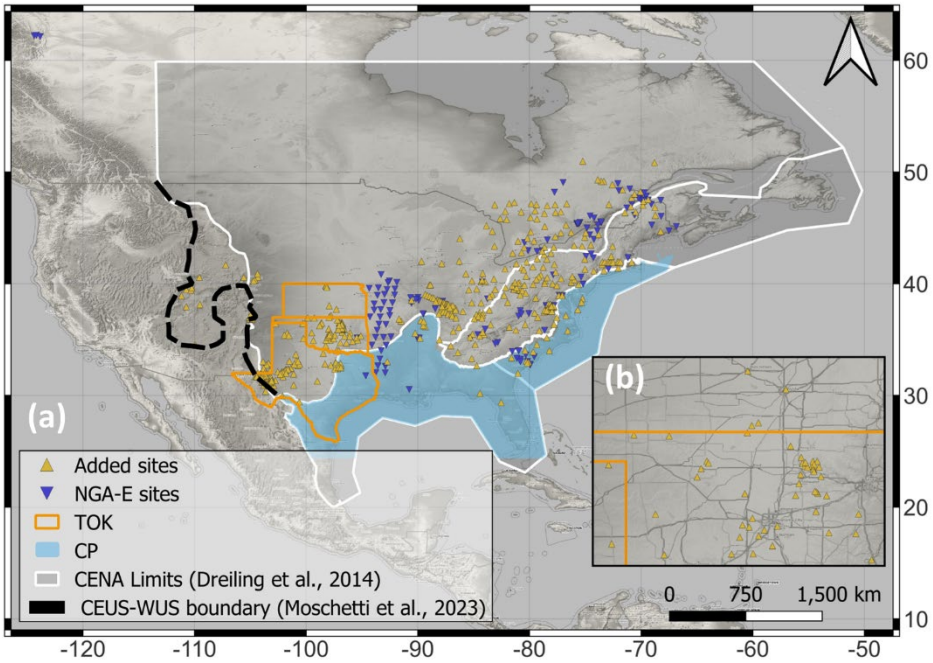

Figure 3.1 Locations of the NGA-East ground-motion recording stations considered in the present study as well as new stations added to the CENA database (b) Detailed view of Oklahoma with high station density.

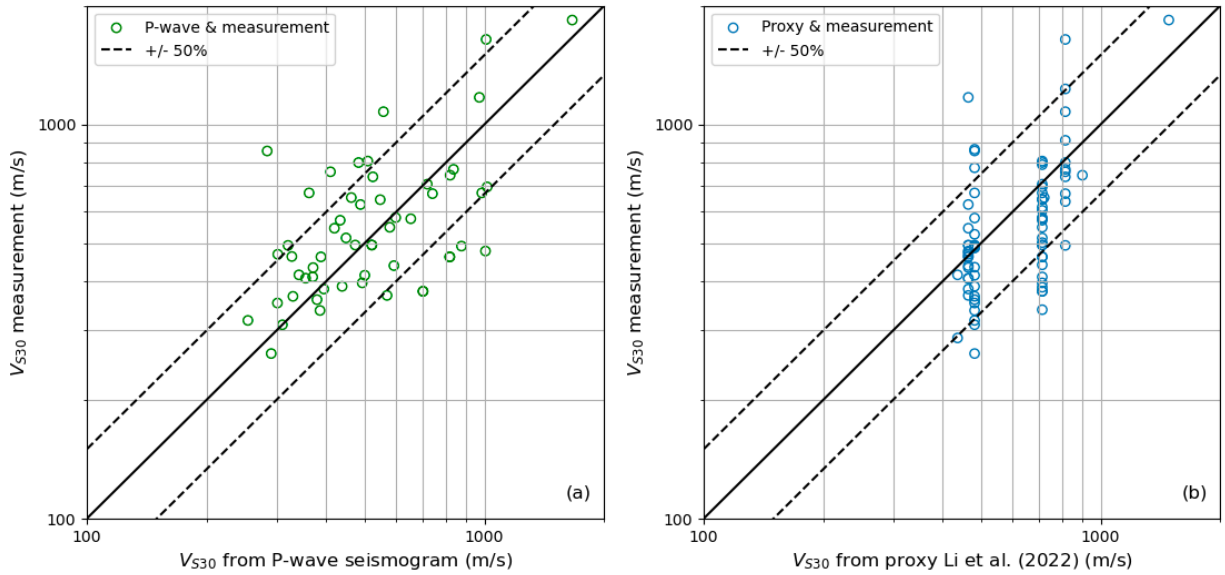

Figure 3.2 (a) Comparison between measured V_{S30} and P-wave seismogram estimated V_{S30} at 55 sites; (b) Comparison between measured V_{S30} and estimated V_{S30} based on hybrid slope-geology proxy methods by Li et al. (2022) at 79 sites.

3.3 Fields Populated in Relational Database

For the user's convenience the CENA data used in Chapter 4 has been made accessible in DesignSafe (Ramos-Sepulveda et al., 2023b) Moreover, for efficient storing purposes, the data is archived in a publically web-serviced ground-motion relational database that connects 25 tables of data, metadata and intensity measures by primary and secondary keys (Buckreis et al., 2023a). This database also includes data from previous NGA projects (NGA-West1 and NGA-West2) and recent California studies (Buckreis et al., 2023b, Nweke et al., 2022). The ground-motion database uses MySQL as the management system, and an application programming interface (API) was written to facilitate queries using URLs. Ground-motion records from NGA-East and newly added records are stored in the database under the "collection_id" of 3 and "user_id" of 2 respectively.

The database includes computed ground-motion intensity measures (e.g., peak ground acceleration, peak ground velocity, response spectra from 0.01 to 10 sec, and effective amplitude spectra) as well as the acceleration time series. However, it does not include the time series processed as part of the NGA-East project, only the intensity measures and metadata as provided in Goulet et al. (2021b). Most of the NGA-East metadata was not modified or updated with the exception of sites with recently measured V_S profiles. Additional features related to CENA that are part of the database are the Wisconsin glaciation limits, coastal plains limits, basins used in Parker et al., 2017 proxy, and coastal plain sediment depth as measured by Boyd et al., 2023. All of which can be found in the geometry table.

The data compiled as described in Section 2.2.2 for TOK is not included in the relational database. This data, which is used in Chapter 5, is partially provided in a flatfile published in DesignSafe project (Li et al. 2023) (data processed by Meibai Li and George Zalachoris). Time series data for the data processed by George Zalachoris is available in Zalachoris et al. (2020).

4 Model Bias

This chapter examines bias of the CENA GMM as provided by Goulet et al. (2021a) when combined with site factors by Stewart et al. (2020) used in the 2018 and 2023 versions of the National Seismic Hazard Model. The work presented in this chapter is also the subject of a journal paper by Ramos Sepulveda et al. (2023c).

GMM performance is assessed through residuals analyses. We define the residual as the difference between an observation (natural-log intensity measure from a recording) and a GMM estimate of the mean ground motion,

$$\delta_{ijk} = \ln(Y_{ij}) - [\mu_{ln,k}(\mathbf{M}_i,(R_{rup})_{ij},\ V_S = 3000) + F_{lin}(V_{S30})] \quad (4.1)$$

where Y_{ij} is the observed intensity measure for event *i* and station *j*, $\mu_{\ln,k}(\mathbf{M}_i,R_{rup,ij})$ is the natural-log (ln) mean estimated intensity measure at the hard-rock for magnitude $\mathbf{M}_i$ and rupture distance $R_{rup,ij}$ from GMM *k*, and F_{lin} is the CENA-specific linear site amplification (Eq. 1.2) in natural log units. The residuals are partitioned into the following terms using mixed effect regression analysis (Bates et al., 2015; R Core Team, 2019)

$$\delta_{ijk} = c_k + \eta_{E,i} + \delta W_{ij} \quad (4.2)$$

where c_k is the overall bias for GMM *k*, $\eta_{E,i}$ is the event term for event *i* and δW_{ij} is the within-event residual. Note that subscript *k* is not used for the event term and within-event residual for brevity, although these terms are specific to a GMM.

Initial residuals analyses (referred to as "baseline" below) were performed using the NGA-East central branch GMM and the CENA data set with minimal screening in which $\mathbf{M} \geq 4$ events were considered with recordings at distances $R_{rup} \leq 600$ km. The NGA-East GMMs can be used to estimate intensity measures for distances up to 1500 km, but the 600 km threshold was applied to avoid problems related to biased ground-motion sampling at larger distances. Ground-motion data was not considered beyond its maximum usable period (taken as the 80% of the inverse of the high-pass corner frequency). No lowest-usable period was applied if the low-pass corner frequency (f_{cLP}) is 40 Hz or greater since S_a is usually controlled by lower frequencies (Douglas and Boore, 2011); otherwise the lowest-usable period was taken as $1.25/f_{cLP}$. The purpose of these analyses was to examine trends in residuals with magnitude or distance and confirm that the observed bias corresponded to CENA in an overall sense, and not to the unmodeled trend of a specific region. The regions considered are TOK, Gulf Coast, the remainder of CENA, and combinations thereof (shown in Figure 2.5).

4.1 Regional Variations of Magnitude and Distance Scaling

Regional variations between TOK (Figure 4.1) and the remaining CENA data were examined. TOK was considered as a region with potentially distinct ground-motion scaling on the basis of prior studies from literature (e.g., Zalachoris and Rathje, 2017; Moschetti et al., 2019) and the concurrent work reported in Chapter 5. Results of the baseline mixed effects analyses (Eq 4.2)

were grouped based on event location into TOK and non-TOK groups using the boundaries in Figure 2.5. The non-TOK group in this case includes the coastal plain regions (regional variations for coastal plain and other non-TOK areas are considered below).

Figure 4.1 shows the resulting trends of event terms ($\eta_{E,i}$) with magnitude for the central branch GMM. We recognize the narrow range of magnitudes available in the empirical data and that our findings are bounded by this condition. For TOK, the binned means of event terms are near zero for **M** = 4 to 5 and there is not sufficient data to assess trends for larger **M**. For non-TOK in the main data range (e.g., **M** 4 to 5), binned means are positive at short periods and negative at long periods and there is no perceptible trend with **M**. The nearly zero average of TOK event terms and non-zero average of non-TOK suggests regional variations in ground-motion levels are present. This can be understood by recalling that a single bias term is computed in the baseline analyses across all data; accordingly, deviations in mean event term for a particular region indicate different ground-motion levels in that region relative to the baseline average. The near-zero mean of event terms for TOK is a consequence of that region dominating the data set (146 of 187 events), whereas the positive mean of short-period event terms for non-TOK events indicates stronger average ground-motions than the baseline average (and the TOK region).

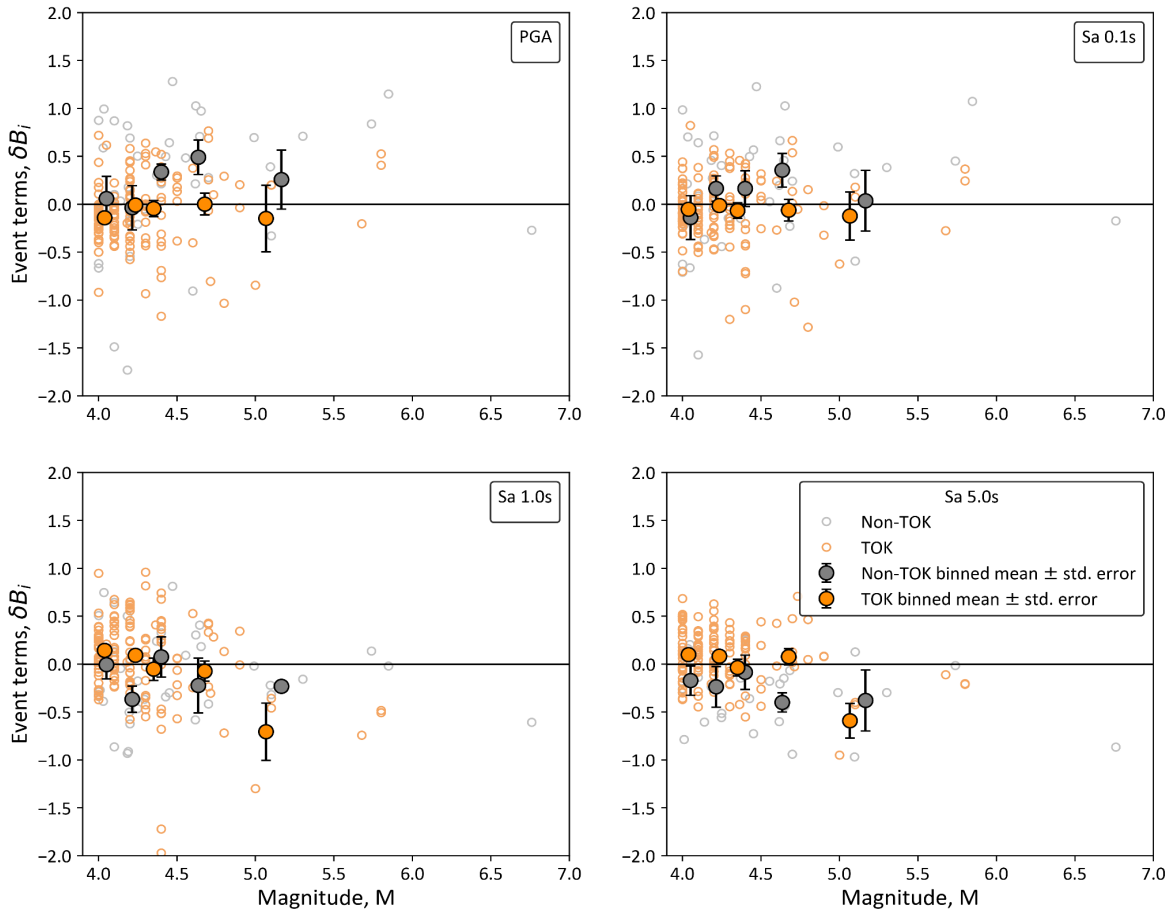

Figure 4.1 Baseline analysis event term trends with magnitude for TOK and non-TOK regions. Vertical bars through binned means indicate ± one standard error of the mean.

To further study source effects, event terms were plotted against hypocentral depth in Figure 4.2. The data is scattered for non-TOK regions, as depicted by the large error bars, hence we lack sufficient data to assess trends for a particular region. Nonetheless, subtle negative trends are perceived for the overall data at long periods for depths greater than 8 km. This could be another indicator of bias in the source model.

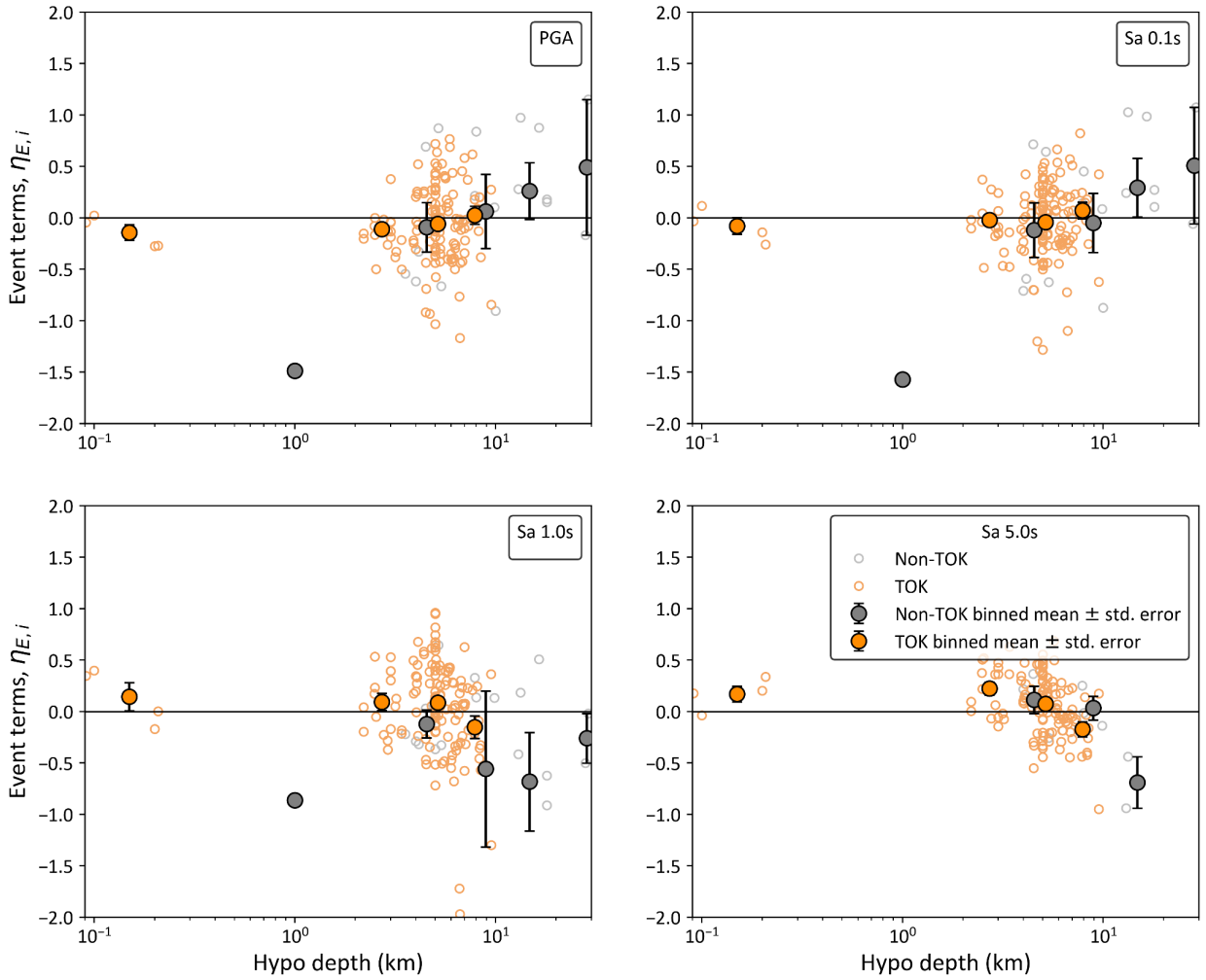

Figure 4.2 Baseline analysis event term trends with hypocentral depth for TOK and non-TOK regions. Vertical bars through binned means indicate ± one standard error of the mean.

Figure 4.3 shows the trend of within-event residuals (δW_{ij}) with respect to distance (R_{rup}). At short periods, a significant upward trend is observed in binned means as R_{rup} increases for TOK events from approximately 10 to 150 km, whereas the non-TOK trend is flat over the full distance range. Both regions have flat trends with distance for long-period intensity measures (Sa at 1.0 or 5.0 sec). These results indicate that the distance attenuation component of the NGA-East central branch GMM is biased in the TOK region but performs well elsewhere in CENA.

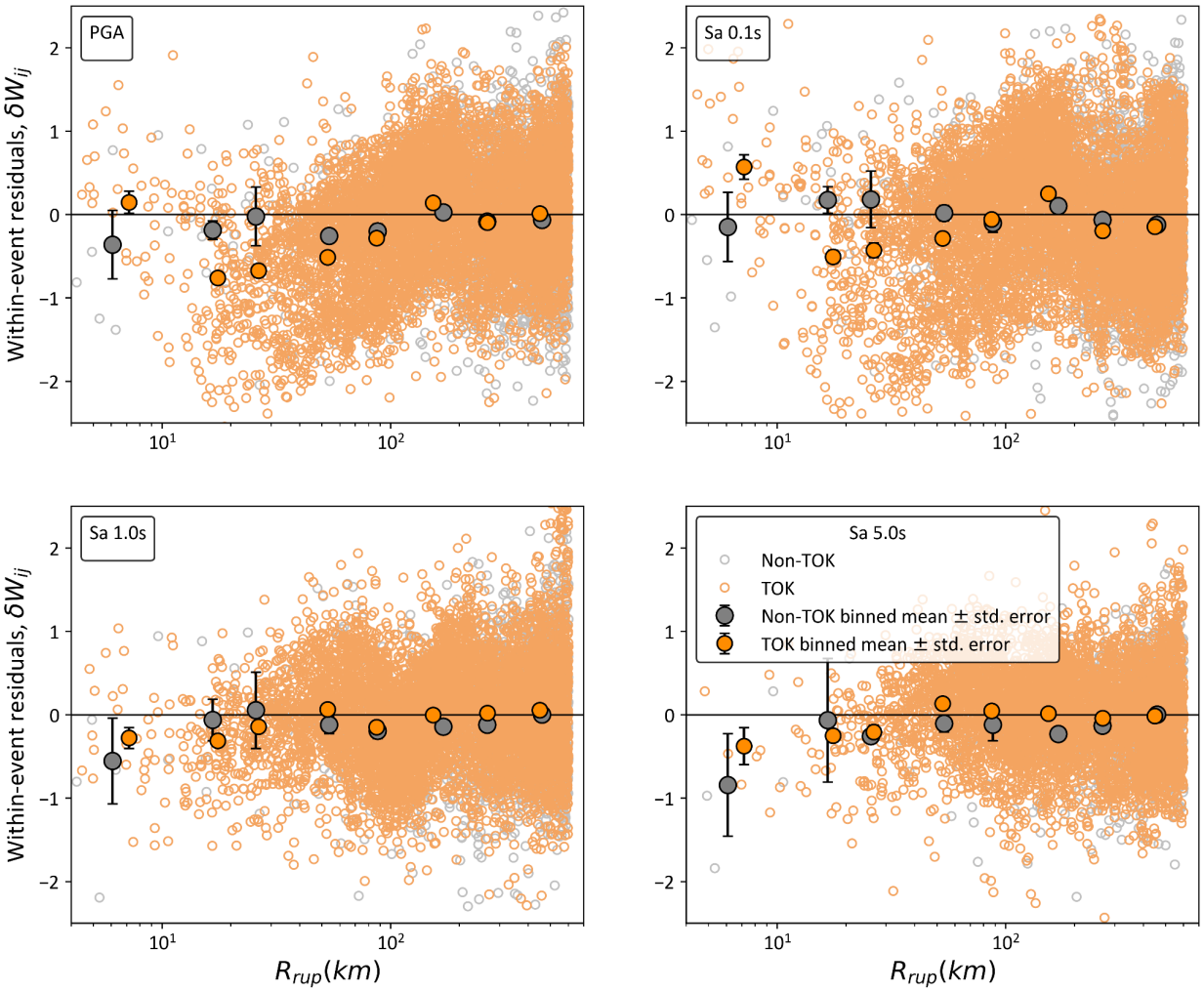

Figure 4.3 Baseline analysis within-event residuals trends with distance (R_{rup}) for TOK and non-TOK regions. Vertical bars through binned means indicate ± one standard error of the mean.

Regional variations for the coastal plain regions, marked in Figure 2.5, were also considered for two reasons: (1) distinct path effects have been observed previously in the Gulf Coast region (Goulet et al., 2021a, Pezeshk et al., 2021) and (2) the Gulf Coast and Atlantic Coastal Plain regions have relatively deep sediments that appear to affect site response in ways not considered in the Stewart et al. (2020) V_{S30}-based models (Guo and Chapman, 2019; Chapman and Guo, 2021; Schleicher and Pratt, 2021; Pratt and Schleicher, 2021). These regional effects could be anticipated to affect path effects, site effects, and potentially average ground-motion levels.

To evaluate potential regional effects in the coastal plain (CP) regions, a subset of the database without TOK events was considered, which significantly reduces the database size (41 events, 1671 recordings). Figure 4.4 shows event terms as a function of **M** for the non-TOK data grouped into CP events (identified based on boundaries in Figure 2.5) and other non-CP events. The short-period binned means are slightly smaller for CP events but their confidence intervals overlap.

Differences are essentially imperceptible at long periods. Due to similar issues with the scarce CP data, trends with hypocentral depth were not studied.

In this chapter, we do not specifically examine scaling trends and biases for the TOK region, which is the subject of Chapter 7.

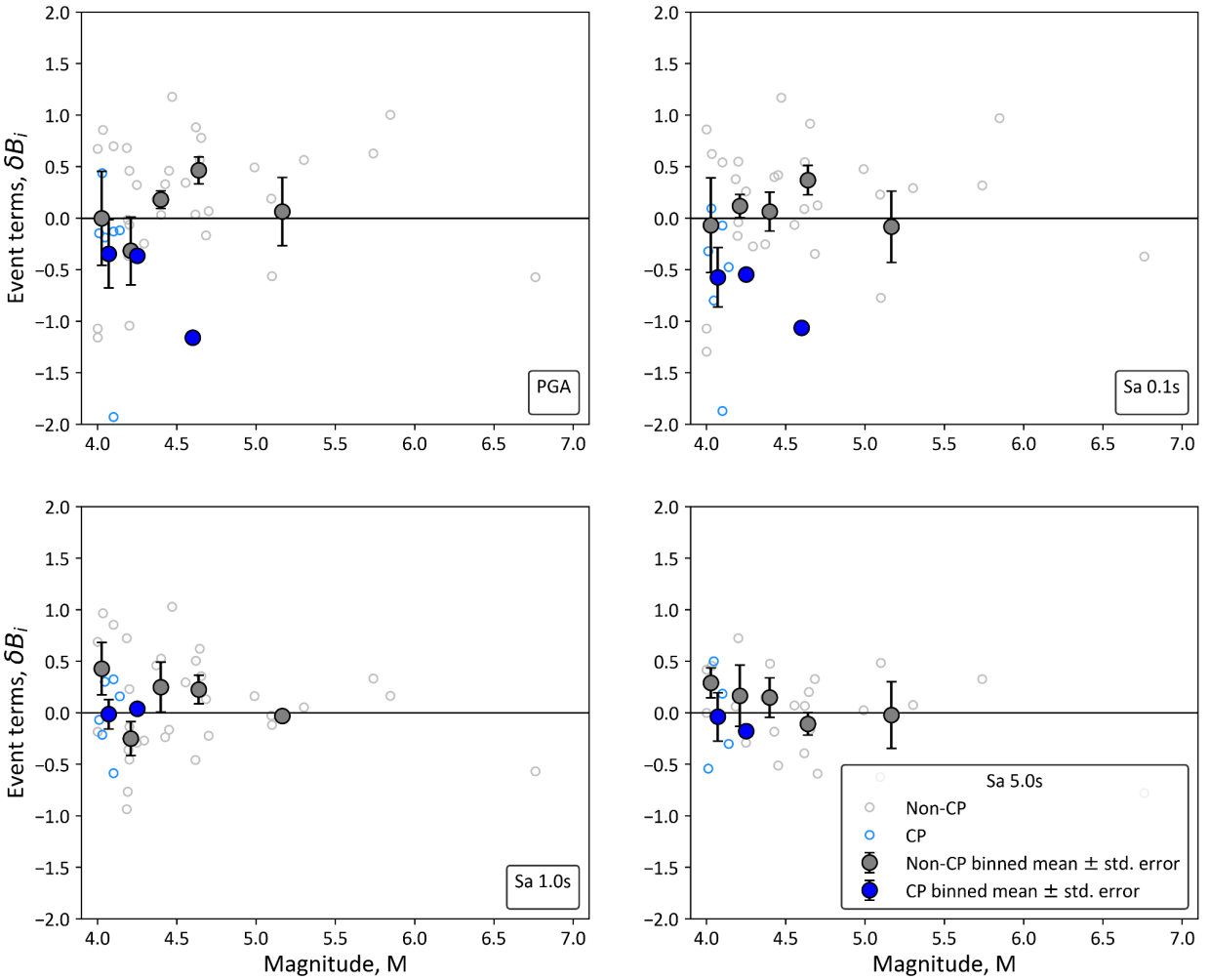

Figure 4.4 Analysis of non-TOK data showing event term trends with magnitude for CP and non-CP regions. Vertical bars through binned means indicate ± one standard error of the mean.

Figure 4.5 shows the distance trend of δW_{ij} for the non-TOK data grouped into events and sites within the CP (identified based on boundaries in Figure 2.5) and other non-CP events or sites. At short periods, a downward trend is observed in binned means for CP sites for $R_{rup} \geq 300$ km, whereas the non-CP trend of binned means is flat to 600 km. Neither region has trends with distance for long-period intensity measures (Sa at 1.0 or 5.0 sec). These results indicate that the anelastic attenuation component of the NGA-East central branch GMM lacks sufficient anelastic attenuation at short periods for CP regions. For subsequent analyses described in the next section, we only consider CP data to maximum distances of 300 km to avoid tradeoffs with misfits in the NGA-East distance-scaling model.

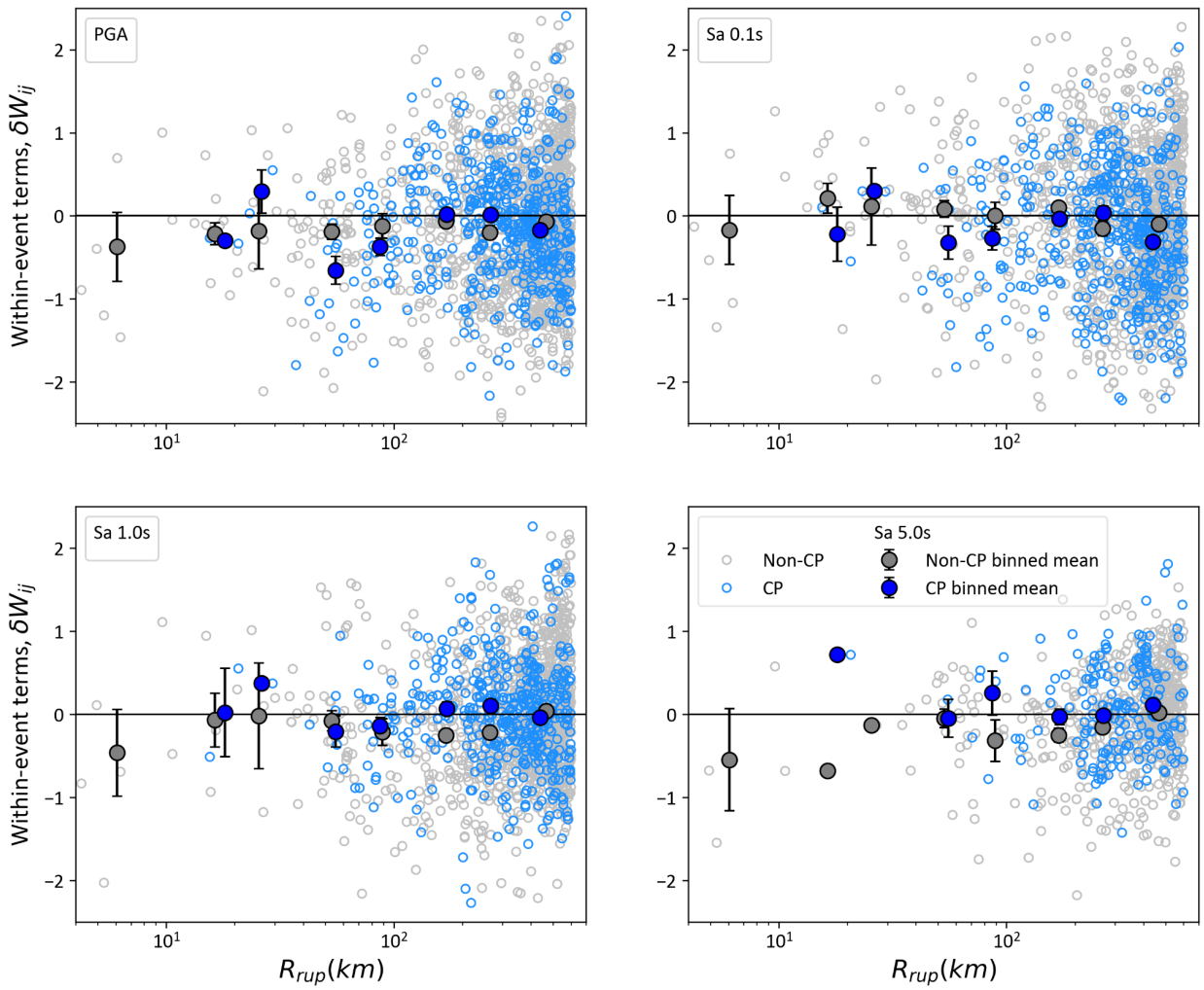

Figure 4.5 Analysis of non-TOK data showing within-event residuals trends with distance (Rrup) for CP and non-CP regions.

To evaluate the performance of the V_{S30}-dependent site amplification model (F_{lin} in Eq. 1.1), we partition the within-event residuals using mixed effects analysis to evaluate site terms (η_S) and remaining residuals (ε_{ij}),

$$\delta W_{ij} = \eta_{S,j} + \varepsilon_{ij} \tag{4.3}$$

The site terms represent the approximate misfit of the model used in the original residuals calculation (Eq. 1.1) for the given sites, after bias and event-term corrections have been applied. Figure 4.6 shows the trend of site terms with V_{S30}, from which we see no appreciable trend. This indicates that the V_{S30}-scaling component of the site amplification model is consistent with the data. The results in Figure 4.6 apply for the full non-TOK data set. We have not yet attempted to parse regional dependencies in site amplification, which will be the subject of future work.

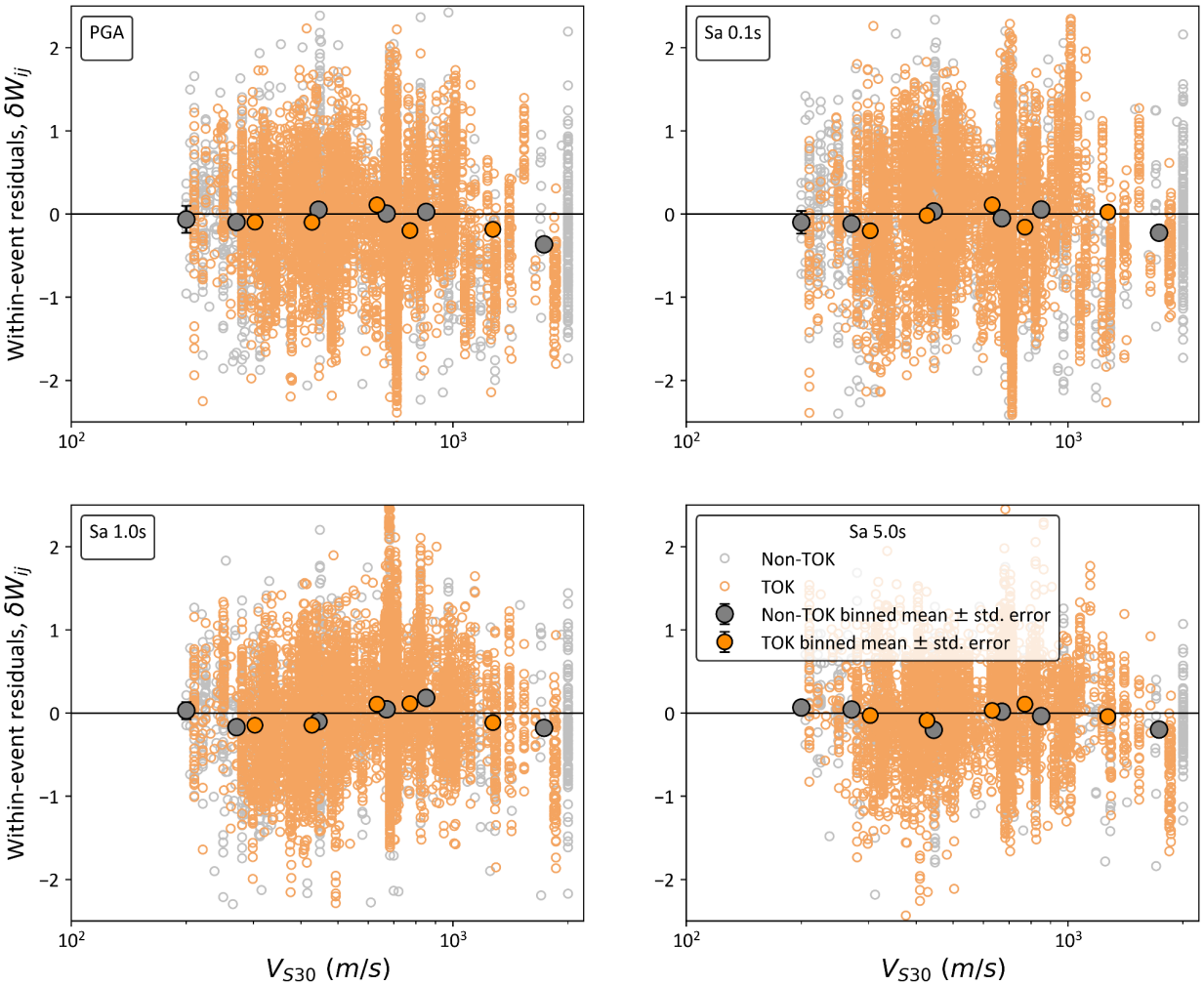

Figure 4.6 Trend of non-TOK site terms trends with V_{S30}. Vertical bars through binned means indicate ± one standard error of the mean.

4.2 Bias Analysis

The data analysis in Section 4.1 suggests that the TOK region has distinct features that affect distance attenuation and overall ground-motion levels. Moreover, as shown in Figure 2.6, TOK has a substantial event concentration (events per area) as compared to the rest of CENA, which to some extent produces results that largely reflect TOK attributes. Although less compelling, CP sites also have some different ground-motion features, mainly in relation to large-distance anelastic attenuation.

Considering the above, different subsets of the CENA data are studied for the bias analysis:

1. Partial TOK: All non-TOK events are considered. Within TOK, 9 events from the 146 are selected (randomly) so that the event density (number of events per area) is consistent with other parts of CENA.
2. Non-TOK: Only non-TOK events are considered.
3. Non-TOK and Non-CP: From the Non-TOK subset, events and sites within the CP (defined using a minimum sediment depth of 100 m) are excluded.

Mixed effects analyses (Eq. 4.2) were repeated for each of these subsets of data using the central branch NGA-East GMM. This produces three sets of bias (c_k) terms, as shown in Figure 4.7, the mean of these sets ± 1 standard error is included. For reference purposes, the c_k term for the full CENA dataset is also shown. The results show a consistent trend of negative bias at short periods (i.e., models are overpredicting the amplification) and positive bias at long periods (models are underpredicting the amplification). There are modest differences between the three data subsets, with the partial TOK producing the largest bias in terms of absolute value, non-TOK and non-CP the smallest, and non-TOK being the intermediate case.

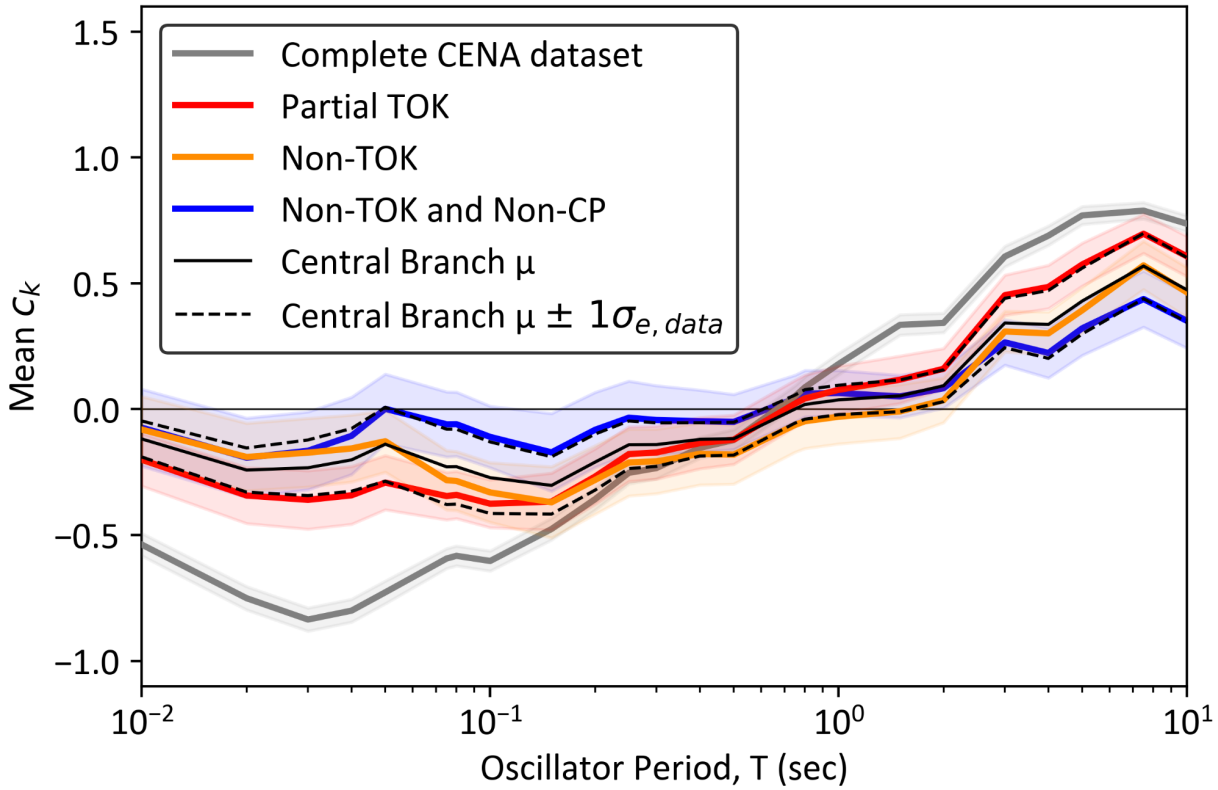

Figure 4.7 Period-dependence of bias term c_k ± standard error for NGA-East central branch GMM for alternate data sets.

Figure 4.8 shows c_k for the non-TOK subset using all 17 NGA East GMMs, along with the population weighted mean, mean ± one weighted standard deviation. The weights applied in these calculations were taken from Goulet et al. (2021a) for the 17 GMMs and were equal for the three data selection criteria. We did not evaluate potential data misfits in relation to magnitude and distance scaling for each of these 17 GMMs as was done for the central branch. It is possible

that individual GMMs with large bias in Figure 4.8 are influenced by scaling problems. Comparing Figures 4.8 and 4.7, it is clear that the uncertainty introduced by alternate GMMs substantially exceeds that from alternative data selection protocols. Although not shown here for brevity, the bias that is found when only the NGA-East data is considered is similar to that shown for the expanded data set in Figures 4.7 and 4.8 (Ramos-Sepulveda et al. 2022). Moreover, Boore (2020) observed qualitatively similar bias trends to those reported here, using the NGA-East dataset and the Boore (2018) GMM.

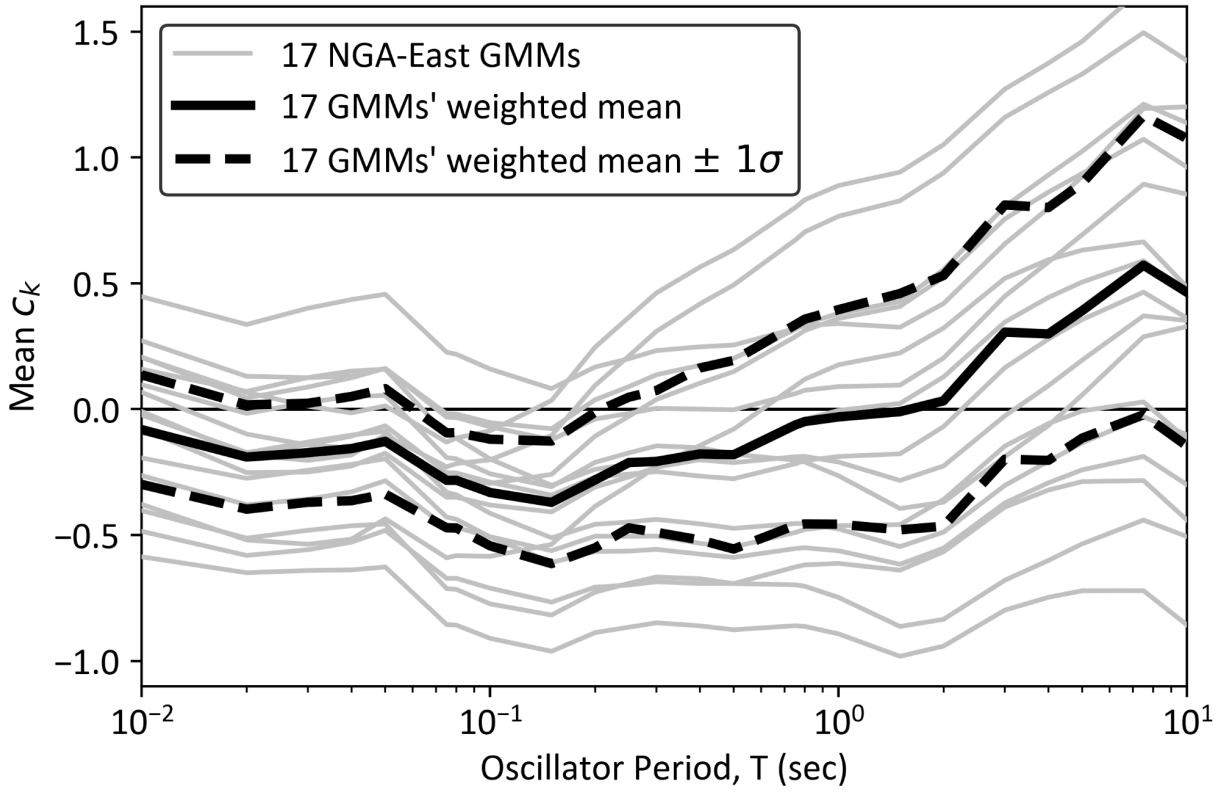

Figure 4.8 Period dependence of bias term c_k for 17 NGA-East GMMs for Non-TOK and weighted mean bias.

4.3 Bias Model

We consider the 17 alternative NGA-East GMMs (weighted as suggested by Goulet et al. 2021a) and 3 alternative data selection criteria (equally weighted) to compute 51 bias terms. Figure 4.9a shows the resulting weighted mean of the 51 bias terms (overall μ) ± one weighted standard deviation (□e). A smoothed version of the bias is also shown for use in forward applications. The weighted mean bias from the 51 values was found to be equivalent to the weighted mean bias obtained using only the single central GMM and the three alternative data sets, which confirms that the central branch model is the weighted mean of the 17 alternative NGA-East GMMs. Figure 4.9b shows the period dependence of the overall standard deviation (across the 51 bias terms) and the standard deviation from alternative data selection criteria only (□e,data). The latter standard deviation ($\sigma_{e,data}$) is computed using biases from the central branch GMM with the three data sets

(between-GMM uncertainties are not included). This standard deviation was found to be nearly identical to those obtained with other single GMMs from the group of 17.

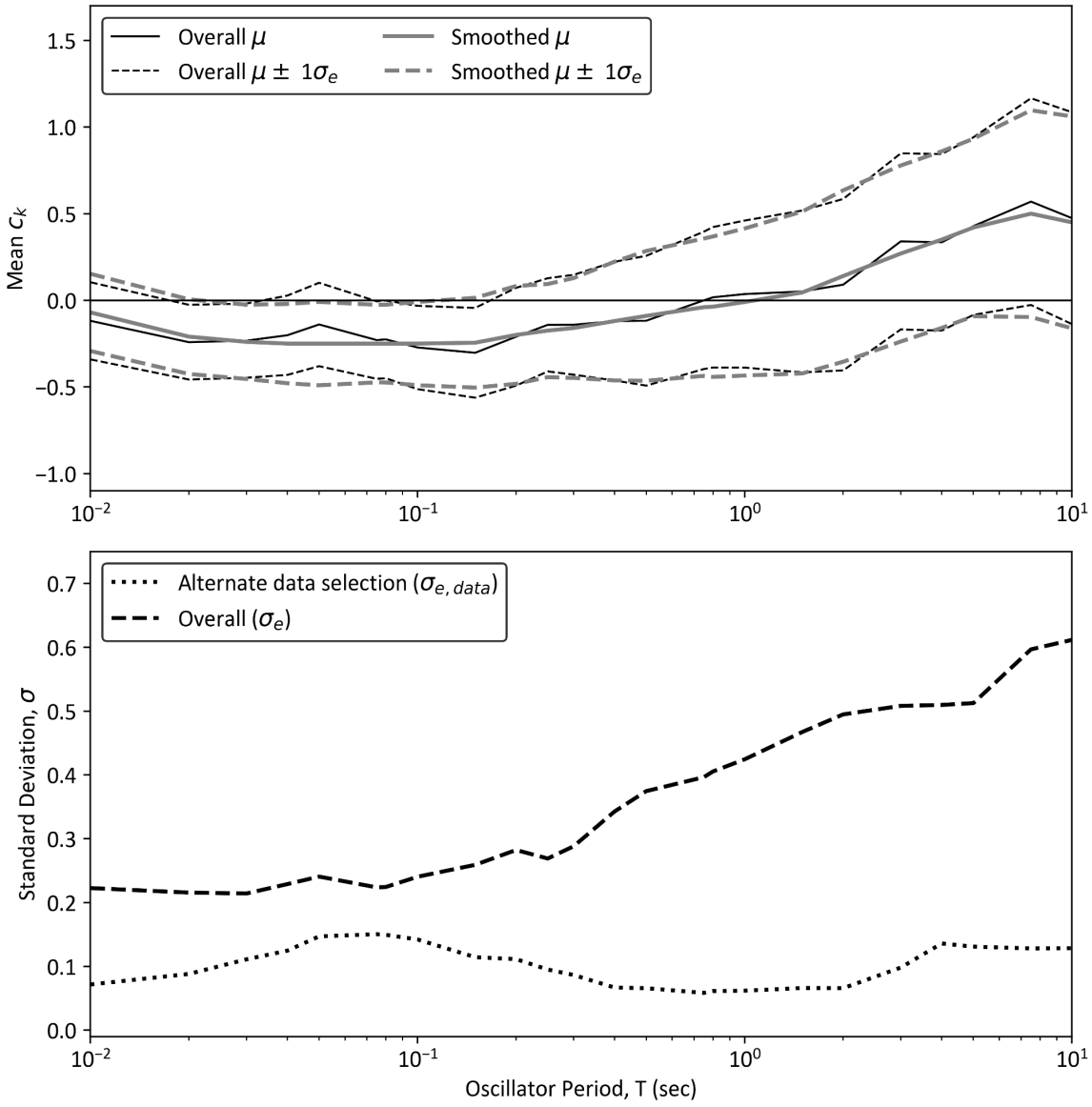

Figure 4.9 (a) Period dependence of bias term c_k for 51 bias terms and (b) standard deviation for all 51 bias terms and standard deviation across datasets.

For forward analysis in which the 17 NGA-East GMMs are considered in the logic tree, there is no need to consider the between-GMM bias uncertainty in the logic tree (to do so would double-count this uncertainty). In this case, the applicable epistemic uncertainty is labeled as “alternate data selection” in Figure 4.9b ($\sigma_{e,data}$). If only the central GMM is considered, the central branch bias and the larger epistemic uncertainty should be considered. Table 4.1 provides values of the recommended biases (after smoothing) and standard deviations representing epistemic uncertainties.

To apply the bias model in forward ground-motion analyses, the bias values are simply added to the natural-log mean ground-motions as computed from the combined models (hard-rock GMM and site response). Further recommendations on model application are provided in Chapter 8.

Table 4.1 Recommended natural-log mean biases and epistemic uncertainties (expressed in the form of a natural-log standard deviation).

Period, T (s)	**smoothed μ**	**σ_e**	**$\sigma_{e,\ data}$**
PGV	-0.153	0.372	0.203
PGA	-0.088	0.248	0.104
0.01	-0.070	0.072	0.223
0.02	-0.210	0.088	0.216
0.03	-0.240	0.111	0.214
0.04	-0.250	0.125	0.229
0.05	-0.250	0.147	0.241
0.075	-0.250	0.150	0.224
0.08	-0.250	0.149	0.224
0.1	-0.250	0.142	0.240
0.15	-0.245	0.114	0.259
0.2	-0.200	0.111	0.282
0.25	-0.175	0.095	0.269
0.3	-0.160	0.086	0.288
0.4	-0.120	0.067	0.343
0.5	-0.090	0.066	0.375
0.75	-0.040	0.058	0.396
0.8	-0.037	0.061	0.405
1	-0.010	0.062	0.424
1.5	0.045	0.066	0.467
2	0.140	0.066	0.495
3	0.270	0.098	0.508
4	0.350	0.136	0.510
5	0.420	0.131	0.512
7.5	0.500	0.128	0.597
10	0.450	0.128	0.611

4.4 Causes of the Bias

The GMM used for residuals analysis in the previous section has three components: a hard-rock GMM (i.e., in Eq. 4.1), site amplification from hard rock to V_{S30} = 760 m/s (F_{760}), and site amplification from 760 m/s to alternate V_{S30} values in the range of the data (F_V). Given the lack of trend of site terms with V_{S30} (Figure 4.6), the F_V model is unlikely to cause the bias, which instead is likely associated with some combination of the hard-rock GMM and F_{760}. In this section, we evaluate several hypotheses and present our assessments of the causes of the bias.

4.4.1 Differences in NGA-West and East Site Amplification Models

In this sub-section we investigate the degree to which differences between the site amplification models employed during NGA-East GMM development under the SSHAC process, relative to those now used in forward application, may explain some of the observed bias. Parker et al. (2019) (their Table 1) list for each of ten NGA-East seed models if CENA ground-motion recordings were adjusted to the 3000 m/s reference condition as part of the model development process, and provide information on how this was done where applicable. Two of the models use simulations to derive models for reference hard rock conditions, and hence did not perform data adjustments (Chapters 2 and 6 in PEER 2015). One of the models has an empirical V_{S30}-scaling term, but the model is not referenced to hard rock conditions (Chapter 8 of PEER 2015). One of the models is for Fourier amplitudes only (Chapter 11 of PEER 2015). Two of the models were derived by applying a hybrid empirical approach (Campbell 2003) to adjust western US GMMs for CENA for a 760 m/s reference site condition, with adjustment to 3000 m/s using F_{760} factors (Chapters 5 and 7 of PEER 2015). These hybrid empirical models were validated against CENA data using a western US ergodic site amplification model (Seyhan and Stewart 2014; hereafter SS14) to adjust CENA ground-motions to a site condition of V_{S30}=760 m/s; the comparison produced a bias of unreported size, which is expected given the different site conditions (760 m/s for adjusted data vs. 3000 m/s for GMM). These six models are not considered further here because the model development does not include clearly defined factors for adjusting ground-motions from the actual site condition to the 3000 m/s reference.

Of the remaining four models, two general approaches were applied to address site response:

1. Ground motions were adjusted from their actual site condition to approximate what would have been recorded for reference site conditions (3000 m/s) (Chapters 4 and 10 of PEER 2015). The adjustments involved two steps – adjustment of ground-motions from the actual site condition to a reference condition of 760 m/s (F_V), followed by an adjustment from 760 to 3000 m/s (F_{760}). This two-step approach was used because the adjustment to 760 m/s can be constrained by data, whereas F_{760} requires the use of simulations.
2. Use of ground response analysis to compute site responses for different site conditions (Chapters 3 and 9 of PEER 2015).

The two seed GMMs that applied the two-step process used the SS14 model for the first step. SS14 was developed for active tectonic regions and is strongly influenced by data from California. The model has relatively strong V_{S30} scaling, particularly at long periods. While the model has

linear and nonlinear components, only the linear part is needed in this case due to the generally low amplitude of the CENA data. For these GMMs, F_{760} terms were derived from one-dimensional ground-response simulations, with the versions used provided by Frankel et al. (1996), Atkinson (2012), and Boore (2015).

To investigate the potential impact of the different site amplification models, we consider differences between SS14 combined with Atkinson (2012) for the site corrections compared to Stewart et al. (2020) for the CENA site response in forward applications (e.g., as used in Petersen et al., 2020). The assumption made during NGA-East GMM development can be viewed as taking the natural log mean motion for a given V_{S30} ($\mu_{ln,k}^{dev}$[V_{S30}]) as,

$$\mu_{ln,k}^{dev}(V_{S30}) = \mu_{ln,k}(3000) + (F_V^{SS14} + F_{760}^{A12}) \quad (4.3)$$

Where $\mu_{ln,k}(3000)$ is the reference site GMM and F_V^{SS14} and F_{760}^{A12} are the SS14 and Atkinson (2012) model predictions, respectively. In contrast, the model as currently applied in the 2018 NSHM is,

$$\mu_{ln,k}^{app}(V_{S30}) = \mu_{ln,k}(3000) + (F_V^{Sea20} + F_{760}^{Sea20}) \quad (4.4)$$

where F_V^{Sea20} and F_{760}^{Sea20} are the Stewart et al. (2020) (Sea20) site factors. The difference in predicted ground-motions produced by the different site amplification models can be taken by subtracting Eq. 4.4 from Eq. 4.3 as shown in Eq. 4.5,

$$\delta\mu_{ln,k} = \mu_{ln,k}^{dev}(V_{S30}) - \mu_{ln,k}^{app}(V_{S30}) = (F_V^{SS14} + F_{760}^{A12}) - (F_V^{Sea20} + F_{760}^{Sea20}) \quad (4.5)$$

To understand the linkage between the difference in Eq. (4.5) with the residuals in Eq. (4.1), it is useful to recognize that (*i*) the central tendency of the residuals, by definition, is c_k and (*ii*) the central tendency of the NGA-East data is $\mu_{ln,k}^{dev}(V_{S30})$ because in Eq. (4.3) $\mu_{ln,k}(3000)$ is fit to the data using the F_V^{SS14} and F_{760}^{A12} models. Accordingly, Eq. (4.1) can be re-written as

$$c_k \cong \overline{\mu}_{ln,k}^{dev}(V_{S30}) - [\overline{\mu}_{ln,k}(3000) + \overline{F}_V^{Sea20} + \overline{F}_{760}^{Sea20}] \quad (4.6)$$

where the overbars represent means across the data population.

By substituting $\overline{\mu}_{ln,k}(3000) = \overline{\mu}_{ln,k}^{dev}(V_{S30}) - (\overline{F}_V^{SS14} + \overline{F}_{760}^{A12})$ from re-arrangement of Eq (4.3) into Eq (4.6) we obtain:

$$c_k \cong \overline{\mu}_{ln,k}^{dev}(V_{S30}) - [\overline{\mu}_{ln,k}^{dev}(V_{S30}) - (\overline{F}_V^{SS14} + \overline{F}_{760}^{A12}) + F_V^{Sea20} + F_{760}^{Sea20}] = \delta\mu_{ln,k} \quad (4.7)$$

Accordingly, a potentially reasonable hypothesis is that the bias evaluated from residuals in this study may be influenced by the differences between the site amplification models.

Figure 4.10a and b show mean values of site amplification for the non-TOK dataset as derived from the two models; the F_V and F_{760} values shown were obtained by exercising the models for

each site and then averaging across sites. Considering F_V first, the amplification applied during model development (SS14) is stronger at all periods, but the differences are most pronounced at long period (about 0.2 natural log units). This difference would cause positive bias (Eq. 4.7), as observed. The differences in F_{760} are negligible for $T > 0.4$ sec, but at short periods the factors applied during model development are much lower than the current factors (about 0.4 natural log units at 0.1 sec). This would tend to produce negative bias, as observed.

Amplification results relative to 3000 m/s from the two simulation-based models, denoted F_V^{sim}, are also shown in Figure 4.10(b) (Chapters 3 and 9 of PEER 2015, authored by Darragh et al., 2015 and Grazier 2015, respectively). The simulation results for Darragh et al. (2015; Dea15) apply for four site conditions; a weighted average of these was used given the V_{S30} values of the sites in the database. The Dea15 results are lower than the $F_V + F_{760}$ sum at long periods and higher at short periods, both of which are relatively consistent with current recommendations (Figure 4.10a). The simulation results for Grazier (2015; G15) were used to derive a V_{S30}-conditioned model; these results follow a different pattern with high amplification at short periods that drops off rapidly as period increases, which is different from both of the empirical models (Sea20 and SS14 + A12) and the Dea15 simulations.

Figure 4.10c compares the differenced site corrections (Eq. 4.5) to the mean bias from Figure 4.9 ± $\sigma_{e,data}$. These results demonstrate that the differences in site amplification and the observed biases have similar features; for example, the long-period underprediction bias appears to be influenced by the much stronger long-period amplification for active crustal regions than for stable continental regions (as contained in the F_V terms). Similarly, the short-period overprediction bias appears to mainly result from the differences in F_{760} models, in particular the strong peak in F_{760}^{Sea20} that is absent in the Atkinson (2012) model. However, the negative bias observed at short periods is much smaller than suggested by these model differences. The differences in F_{760} at these short periods are sensitive to variations in site decay parameter κ_0.

Also contained Figure 4.10c are values of $\delta\mu_{ln,k}$ computed using the Darragh et al. and Grazier simulation models using the following modification of Eq. (4.5),

$$\delta\mu_{ln,k} = F_V^{sim} - (F_V^{Sea20} + F_{760}^{Sea20}) \quad (4.8)$$

where F_V^{sim} is amplification for a particular site condition relative to 3000 m/s as derived from 1D ground response simulations. The Darragh et al. (2015) results indicate $\delta\mu_{ln,k}$ values that are close to zero, which is expected because of the similarity to the Sea20 models used in forward applications. The Grazier (2015) results provide strong trends in $\delta\mu_{ln,k}$ that are opposite to those observed in the bias analyses.

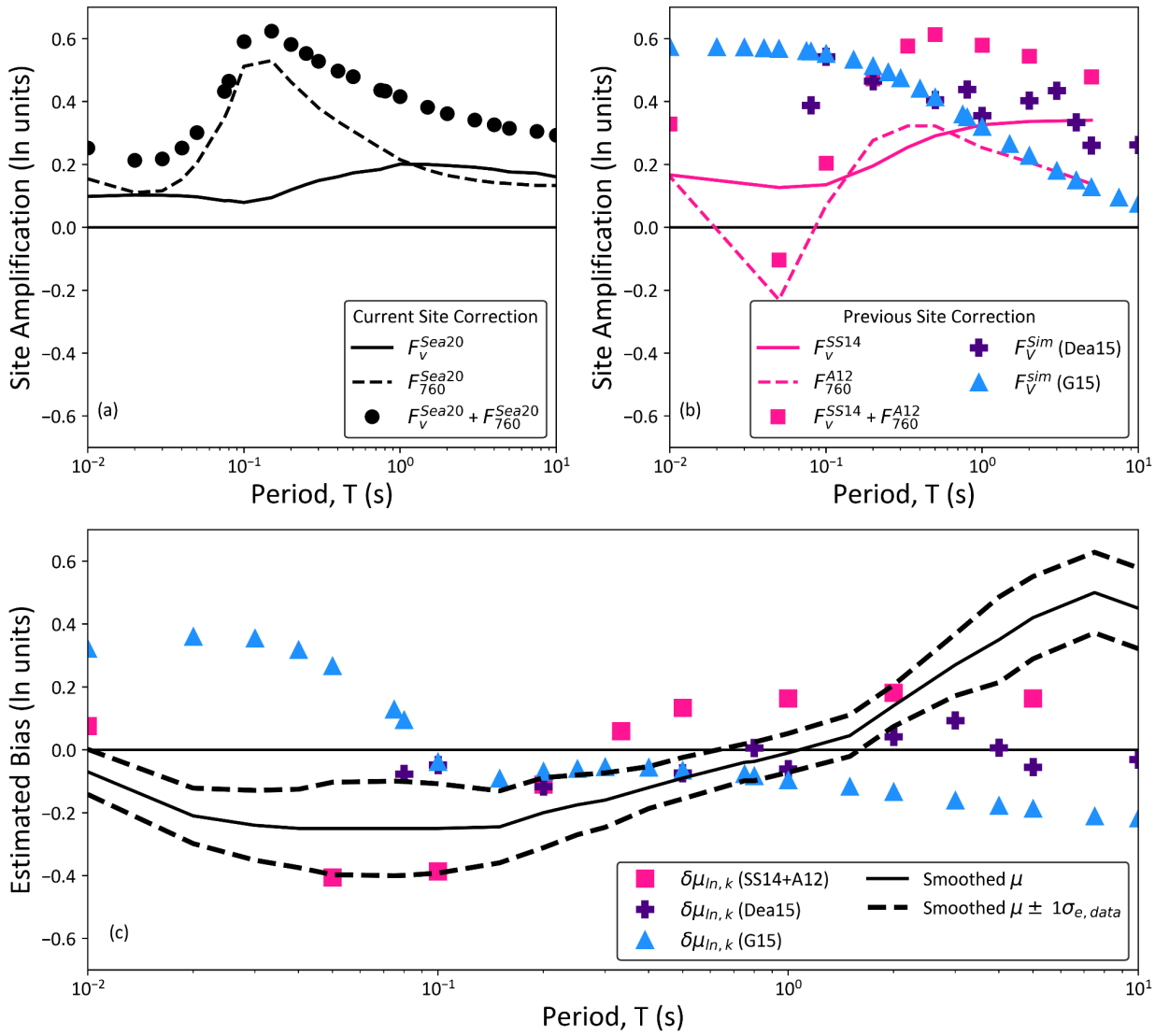

Figure 4.10 (a) Mean site amplification from F_V and F_{760} components of the Stewart et al. (2020) model across all CENA sites in the non-TOK dataset; (b) Mean site amplification from the F_V (SS14) and F_{760} (A12) models across all CENA sites in the *non-TOK* dataset, as well as mean total amplifications (F_V^{sim}) from simulation-based models of Dea15 and G15; and (c) comparison of site response differences (Eq. 4.5 and 4.8) to the recommended mean bias. A12 = Atkinson 2012; SS14 = Seyhan and Stewart (2014); Dea15 = chapter 3 in PEER 2015 by Darragh et al.; G15 = chapter 9 in PEER 2015 by Grazier.

4.4.2 Modifications to F_{760} for CENA

Since the publication of the Sea20 F_{760} factors, additional simulations of site response for sites with V_{S30} = 760 m/s have been performed by Ilhan (2020) and in Chapters 6 and 7 of this report. This work considered additional V_S profiles and additional material damping formulations. Most of the profiles apply for an impedance condition, as defined by Sea20. Figure 13 shows how F_{760} factors derived from this work compare to those in Sea20. While broadly similar, the newer results are larger at long periods and smaller at short periods (T < ~0.03 – 0.1 sec) than the mean factors

for impedance sites in Sea20. If a new F_{760} model were to be developed that reflected such changes, it would reduce the bias at both long and short periods.

The F_{760} reduction at short periods is qualitatively consistent with Ktenidou and Abrahamson (2016), who anticipated the potential for overprediction of short period site response, which they attributed to the NGA-East hard rock κ_0 = 0.006 sec being too small. However, the amount of short-period bias is smaller than anticipated by Ktenidou and Abrahamson (2016).

4.4.3 Bias Attribution

For two of the seed models, the differences between site amplification factors used in model development vs those used in application produces ground-motion changes that are generally consistent with the bias pattern (Figure 4.10c). However, it is difficult to know how much of the overall bias can be attributed to this effect, because it directly impacts only 2 of the 10 seed models and it is unclear how this effect might have influenced the 17 NGA-East GMMs.

As noted previously, we do not anticipate F_V as causing bias. Some of the bias may be from the F_{760} model; at long periods the newer V_S profiles used for 760 m/s sites produce larger amplification than was found previously for impedance conditions (Chapter 7), which if adopted for applications would reduce but not eliminate the bias. At short periods, the bias is small and could easily be accounted for with small adjustments to κ_0. The portions of the bias that cannot be attributed to the F_{760} model must be contained in the hard-rock GMMs.

5 GMM Adjustments for TOK

5.1 Introduction

To evaluate the bias and site amplification effects in the TOK portion of CENA, we make use of the rapidly growing ground motion dataset of TOK. We downloaded, processed, and compiled ground motion recordings for earthquake events in TOK between 2005-2022, as described in Chapter 2. Because a large portion of the data in TOK are from potentially induced earthquakes, and previous research by Zalachoris and Rathje (2019) demonstrated that the region has different magnitude and distance scaling as compared to the broader CENA region, it is necessary to adjust for these effects in the median NGA-East GMM before investigating the site amplification. We therefore develop a new regional GMM using the reference empirical approach (Atkinson 2008) together with the new dataset. Then, a site amplification model is developed from the new GMM and compared with previously published site amplification and F_{760} models for CENA.

This chapter is structured to first describe the methodology used to develop the reference empirical GMM for the study region. This is followed by a description of the dataset used in the study and a presentation of the reference empirical adjustments that represent the new GMM. Finally, the components of the developed empirical site amplification model are compared with previously published models.

5.2 GMM Development Method

5.2.1 Reference Empirical Approach

The same reference empirical approach used by Zalachoris and Rathje (2019) is implemented in this study to develop the GMM specific to TOK. We use the weighted median NGA-East GMM (Goulet et al. 2021a) as the reference GMM and develop adjustment factors to adjust for the magnitude scaling, distance scaling and site amplification effects reflected in the earthquake ground motion dataset for the region. The final empirical GMM is established by applying the adjustment factors and site amplification model to the weighted median NGA-East GMM.

To develop the adjustment factors, the total residuals are first computed for each spectral period as the difference (in natural log scale) between the observed ground motion intensity measure (IM) and the IM predicted using the weighted median NGA-East GMM. To develop an independent site amplification model relative to the NGA-East reference rock condition of $V_{S30} = 3000m/s$, we do not consider site amplification when computing the residuals. Therefore, the reference site condition is hard rock with V_{S30}=3000 m/s and associated kappa (κ_0) of 0.006 s. It is important to note that this reference condition is different than that used in Chapter 4, which included the Stewart et al. (2020) F_{760} in the residual calculation and thus represents a reference condition of V_{S30} = 760 m/s.

The input parameters for the weighted median NGA-East GMM include the moment magnitude (**M**) and rupture distance (R_{rup}), and the total residuals are computed as shown in the Equation 5.1:

$$lnY_{i,j} = \ln(IM_{obs})_{\,i,j} - ln(IM_{pred})_{\,i,j} \tag{5.1}$$

where $lnY_{i,j}$ represents the total residual for recording j and event i; and IM_{obs} and IM_{pred} represent the observed and predicted intensity measures for a recording, respectively. For the observed motions, the two horizontal components are combined into RotD50, the median value of the resultants of the two components as computed over each angle of rotation from 1 to 180° (Boore 2010).

A mixed-effects analysis utilizing the smf function in the Python package statsmodels (Seabold and Perktold 2010) is used to partition the computed total residual $lnY_{i,j}$ into the mean total residual c, inter (between)-event residual η_i, and intra (within)-event residual $\varepsilon_{i,j}$ as:

$$lnY_{i,j} = c + \eta_i + \varepsilon_{i,j} \tag{5.2}$$

The mean total residual c indicates the overall bias of the weighted median NGA-East GMM with respect to the dataset, η_i is the bias for each individual earthquake event (i.e., event term), and $\varepsilon_{i,j}$ is the remaining residual after the overall bias and event term are removed. The adjustment factor for magnitude scaling is derived from the event terms, η_i, while the adjustment factors for distance scaling and the site amplification model are derived from the intra-event residuals, $\varepsilon_{i,j}$.

The overall adjustment factor for the NGA-East weighted median GMM to adjust for the regional ground motion characteristics can be expressed as:

$$lnF = C_{adj} + F_M + F_R + F_V \tag{5.3}$$

where lnF represents the overall adjustment factor which consists of the adjustment factor for the overall mean bias C_{adj}, the magnitude adjustment factor F_M, the distance adjustment factor F_R, and the site amplification adjustment F_V which accounts for the site amplification effect relative to a reference site condition. The site amplification model F_V is a function of V_{S30}.

The stepwise, iterative procedure utilized by Zalachoris and Rathje (2019) is adopted to develop the adjustment factors by conducting least squares regression on the computed residuals. The procedure is implemented with 6 steps as follows:

1. The magnitude adjustment factor F_M is developed by least squares regression of the inter-event residual (η_i) as a function of moment magnitude **M**;

2. New values of the total residuals $lnY_{i,j}$ are computed using the developed F_M, and mixed-effects analysis is conducted to partition the new total residuals into inter- and intra-event residuals;

3. The distance adjustment factor F_R is developed by least squares regression of the intra-event residuals ($\varepsilon_{i,j}$) as a function of rupture distance R_{rup};

4. Updated intra-event residuals are computed using F_R, and the site amplification model F_V is developed by least squares regression of the updated intra-event residuals as a function of V_{S30};

5. New values of the total residuals $lnY_{i,j}$ are computed using the developed F_R and F_V adjustments and mixed-effects analysis is conducted to partition the new total residuals into inter- and intra-event residuals;

6. Repeat steps 1-6 until the model stabilizes, e.g., the coefficients of the models are within 1% of the values obtained from last iteration.

Using this stepwise procedure, the overlapping effects of source, distance, and site effects are avoided, and the model typically stabilizes in 4-5 iterations. After the final F_M, F_R, and F_V are obtained, a last mixed-effects analysis is conducted to compute the final C_{adj}, which is the mean total residual after correction for magnitude, distance, and site effects. The final inter- and intra-event residuals are also obtained which are assumed to be normally distributed with a mean of 0 and standard deviations of τ and ϕ, respectively. The relationship between the standard deviation of the inter- and intra-event residuals and the total standard deviation can be expressed as:

$$\sigma = \sqrt{\tau^2 + \phi^2} \tag{5.4}$$

5.2.2 Extrapolations of NGA-East GMMs

The applicable magnitude range of NGA-East GMMs is 4.0-8.2. However, to augment the dataset in TOK, we consider events with moment magnitude as small as 3.5. Thus, a small magnitude extrapolation is required for the NGA-East GMMs to compute the prediction of ground motion for the magnitude range between 3.5-4.0. We take advantage of the Yenier and Atkinson 2015 (YA15) seed median GMM, which was developed for CENA and used by the NGA-East project, for this purpose. YA15 is selected because it is applicable down to magnitudes of 3.0.

We develop a set of magnitude scaling factors, which is the ratio between the ground motion intensity measure at a magnitude between 3.5-4.0 and the ground motion intensity measure at magnitude of 4.0 for a range of distances. The magnitude extrapolation factor (M_{ext}) is computed using YA15 as follows:

$$M_{ext}(M,R) = IM_{YA15}(M,R)/IM_{YA15}(4.0,R) \tag{5.5}$$

where $M_{ext}(M,R)$ represents the magnitude extrapolation factor for magnitude M $(3.5 < M < 4.0)$ and rupture distance R, $IM_{YA15}(M,R)$ represents the ground motion intensity measure for magnitude M and rupture distance R computed with YA15, and $IM_{YA15}(4.0,R)$ is the ground motion intensity measure for magnitude 4.0 and distance R computed with YA15. We compute the magnitude extrapolation factor for various distance values because the geometrical spreading

function of YA15 has a multiplicative term of magnitude and distance, causing the magnitude scaling to be dependent on distance. Using $M_{ext}(M,R)$ from Equation 5.5, the ground motion intensity measures for magnitude between 3.5-4.0 can be calculated with the weighted median NGA-East GMM by scaling the ground motion for magnitude 4.0 and a certain distance R:

$$IM_{NGA-E}(M,R) = M_{ext}(M,R) \cdot IM_{NGA-E}(4.0,R) \tag{5.6}$$

The effect of the magnitude extrapolation is shown in Figure 5.1 for spectral periods of 0.1 and 1.0 s. By plotting the extrapolated ground motion for magnitudes 3.5-4.0 together with the non-extrapolated ground motion for magnitudes 4.0-5.0, it demonstrates that the magnitude extrapolation using the scaling factor is reasonable for the NGA-East weighted median GMM. This extrapolated NGA-East weighted median GMM is used in this study to compute the predicted ground motion intensity measures, and thus the residuals.

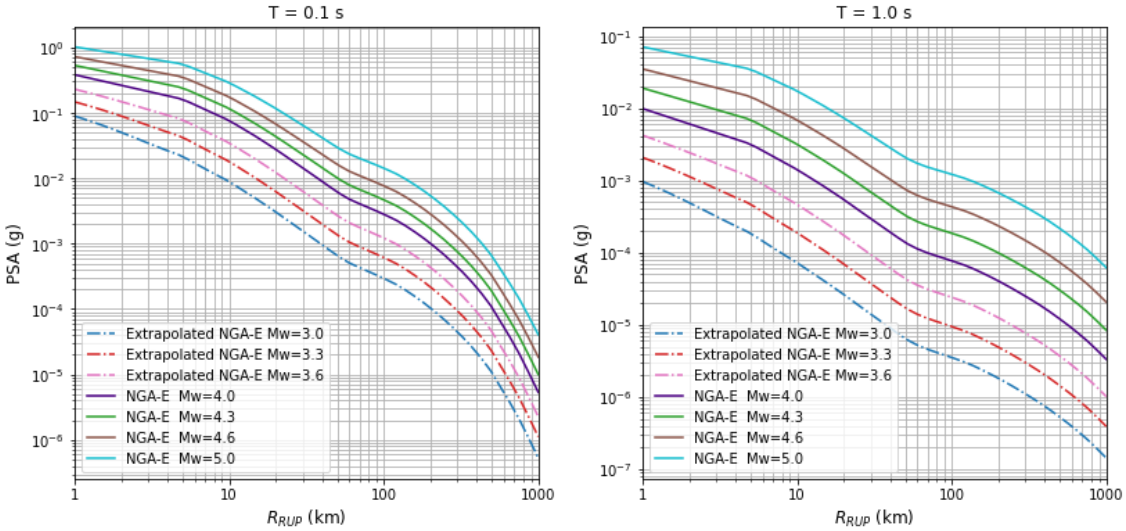

Figure 5.1 Extrapolated ground motion ($3.5 < M < 4.0$) and non-extrapolated ground motion ($4.0 \leq M < 5.0$) as a function of distance for the NGA-East weighted median GMM.

5.3 Ground Motion Database

The final analyzed TOK dataset for *M* > 3.5 includes 12,771 earthquake ground motion recordings from 344 events, occurring between January 2005 and December 2022, recorded by 561 seismic recording stations (Li et al. 2023). Tectonic and potentially induced earthquakes are not distinguished. To avoid the uncertainty associated with estimating moment magnitude from other types of magnitudes, the analyzed dataset only uses events with reported moment magnitudes. We also excluded events with fewer than 3 records. The analyzed dataset includes 3,227 records from the database developed by Zalachoris and Rathje (2019) and 9,544 records from the effort in this study. Rupture distance is not provided for the Zalachoris and Rathje (2019) data and thus we use hypocentral distance as an estimate of rupture distance, which is considered appropriate for the relatively small magnitude events.

The locations of the earthquake events and the seismic recording stations that recorded the ground motions are shown in Figure 5.2. Most of the events in the dataset occurred in Oklahoma and West Texas. Based on the criteria of assigning V_{S30} described previously, all stations have V_{S30} greater than 200 m/s. The Gulf Coast Plain as defined by Coleman and Cahan (2012) is shown in Figure 5.2 by the purple shading, and all stations located within the Gulf Coast Plain were excluded from analysis due to significant differences in geologic and attenuation characteristics of the Gulf Coast Region.

The magnitude and distance distributions of the recordings shown in Figure 5.3 indicate that the dataset spans distances from about 5 km to 500 km and is dominated by events with magnitudes smaller than 4.5. The augmented data since 2016 enhances the distribution of data at distances less than 20 km for magnitudes smaller than 4.5, but the dataset remains relatively sparse for recordings with magnitude greater than 4.5 and rupture distances less than 20 km.

The number of recordings within bins of V_{S30} for the seismic recording stations is shown in Figure 5.4. The dataset is abundant for recordings with V_{S30} between 600-1000 m/s, which composes 44% of the dataset. This suggests that the region of TOK is suitable for evaluating site amplification at relatively stiffer sites.

The number of records for various periods is shown in Figure 5.5. For all ranges of magnitudes, the number of records reduces at long periods due to presence of long period noise in the seismic recordings.

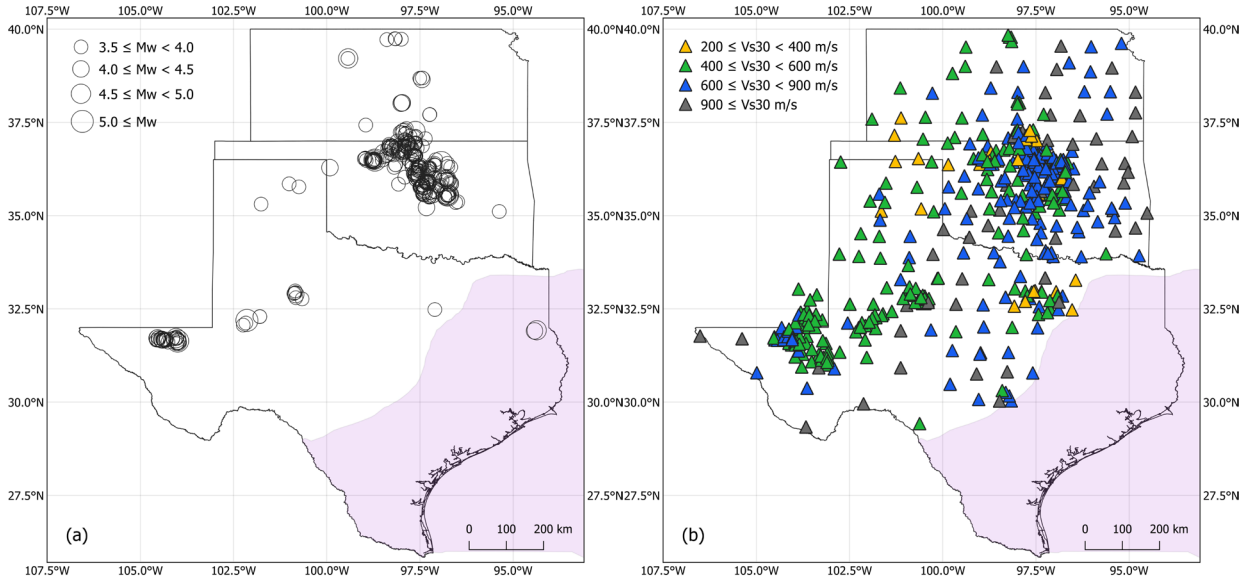

Figure 5.2 (a) Location of earthquake events in the final analyzed TOK dataset; (b) location of seismic recording stations that recorded data in the dataset.

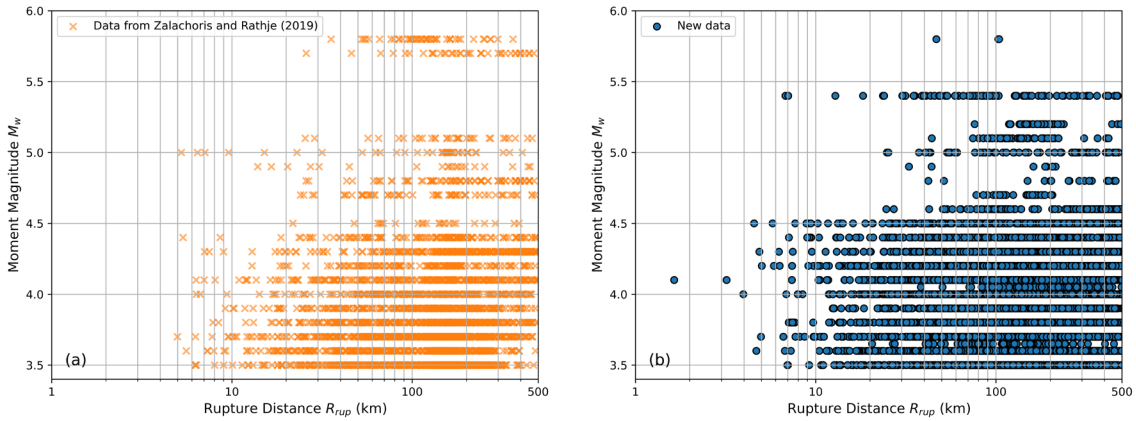

Figure 5.3 Moment magnitude versus rupture distance for ground motions used in this study (a) data from 2005-2016 included in Zalachoris and Rathje (2019) and (b) augmented data from after 2016.

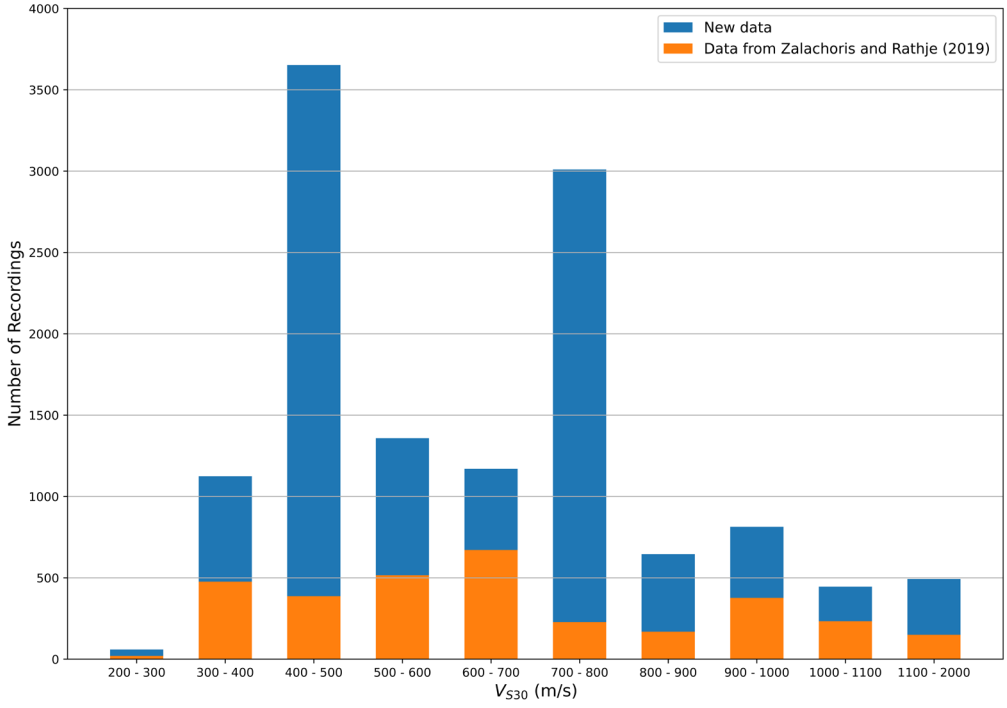

Figure 5.4 Number of recordings for binned V_{S30}.

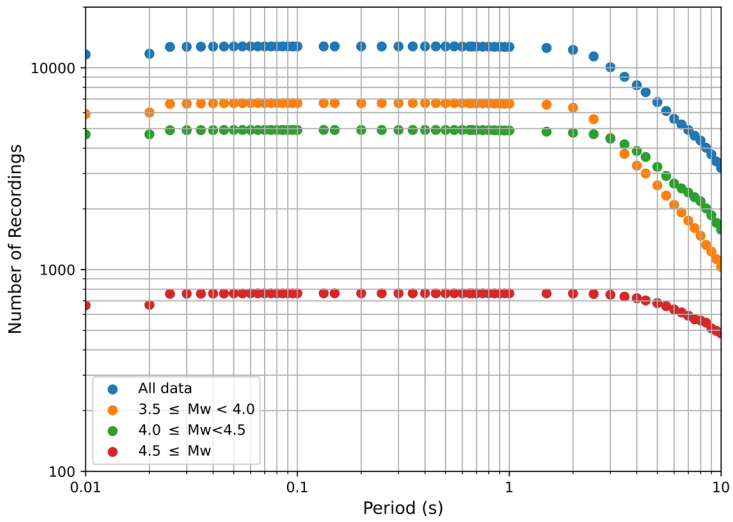

Figure 5.5 Number of recordings for different periods

5.4 Development of GMM for TOK

The reference empirical methodology detailed previously is used to develop the GMM for TOK using the dataset described above. The total residuals are first computed at various spectral periods between 0.01 and 10.0 s, with examples shown in Figure 5.6 for selected periods. Overall, the mean total residuals are not zero at most periods, suggesting that the weighted median NGA-East GMM is biased relative to the data. Negative bias (i.e., the observed IM is smaller than the predicted) is observed at shorter periods (T<0.1s) and positive bias (i.e., the observed IM is larger than the predicted) is detected at relatively longer periods (T>0.3s). Additionally, the bias shows a distance dependence at short periods for shorter distances. The adjustments for magnitude, distance, and site from the partitioned residuals are described separately below.

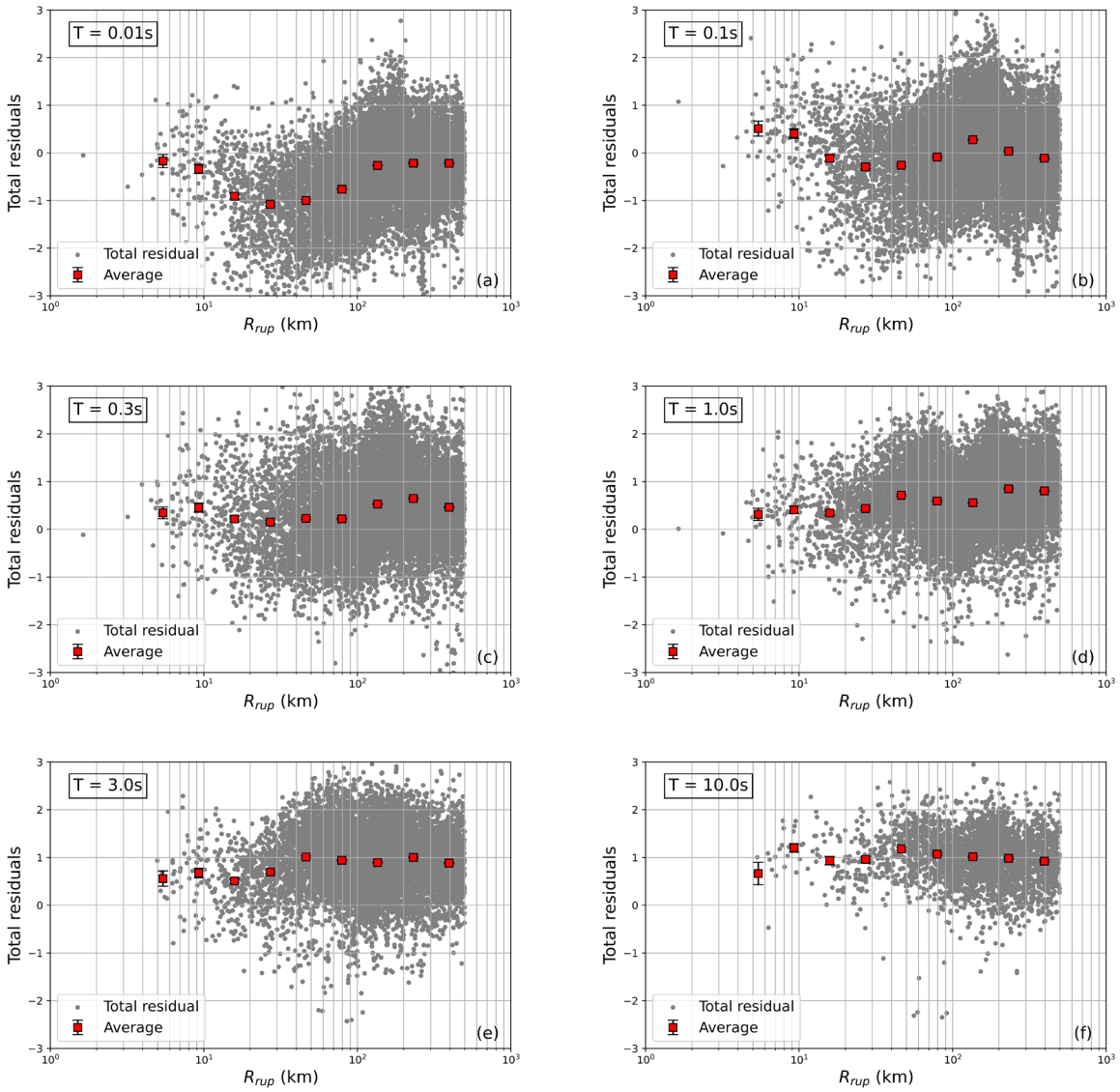

Figure 5.6 Total residual against rupture distance R_{rup} for periods T = 0.05s, 0.1s, 0.3s, 1.0s, 3.0s, and 10.0s.

5.4.1 Magnitude Adjustment

The inter-event residuals η_i (i.e., event terms) are plotted against moment magnitude for each spectral period to inspect the trend of event terms with moment magnitude, with some examples shown in Figure 5.7. The event terms center around 0 (i.e., are unbiased) for smaller magnitudes, but the binned-average event terms become non-zero at larger magnitudes. For shorter periods (T<0.05s), the event terms become positively biased at larger magnitudes, but for longer periods the event terms become negatively biased. The magnitude at which the event terms become biased is slightly different for each period. Although they used a different CENA GMM as the reference model, Zalachoris and Rathje (2019) also identified a similar trend with increasing

magnitude. We model this trend to eliminate the dependence of the inter-event residual η_i on magnitude. For periods between 0.05 s-0.25 s, the trend at larger magnitudes is not significant (i.e., 0 is enclosed by the +/-1SD error bars of the binned averages as shown in Figure 5.7) and we do not apply the magnitude adjustment for those periods.

We adopt the same linear hinge functional form of the magnitude adjustment factor F_M as used by Zalachoris and Rathje (2019):

$$F_M = \begin{cases} b_0 & \mathbf{M} \leq M_b \\ b_0 + b_1(\mathbf{M} - M_b) & M_b < \mathbf{M} < 5.8 \\ b_0 + b_1(\mathbf{5.8} - M_b) & \mathbf{M} \geq 5.8 \end{cases} \quad (5.7)$$

where b_0, b_1, and M_b are coefficients of F_M model. M_b represents the hinge magnitude below which F_M is constant and above which F_M varies linearly with $\mathbf{M}$. The regression process is conducted such that the hinge magnitude M_b is specified and the values of b_0 and b_1 are then obtained by applying least squares regression. M_b is then varied to search for the optimum M_b that produces the least squared fit. For magnitudes above 5.8 (the maximum magnitude in the dataset), F_M is assumed to constant and equal to the value at $\mathbf{M}$ = 5.8. The final F_M function for different periods is shown in Figure 5.7.

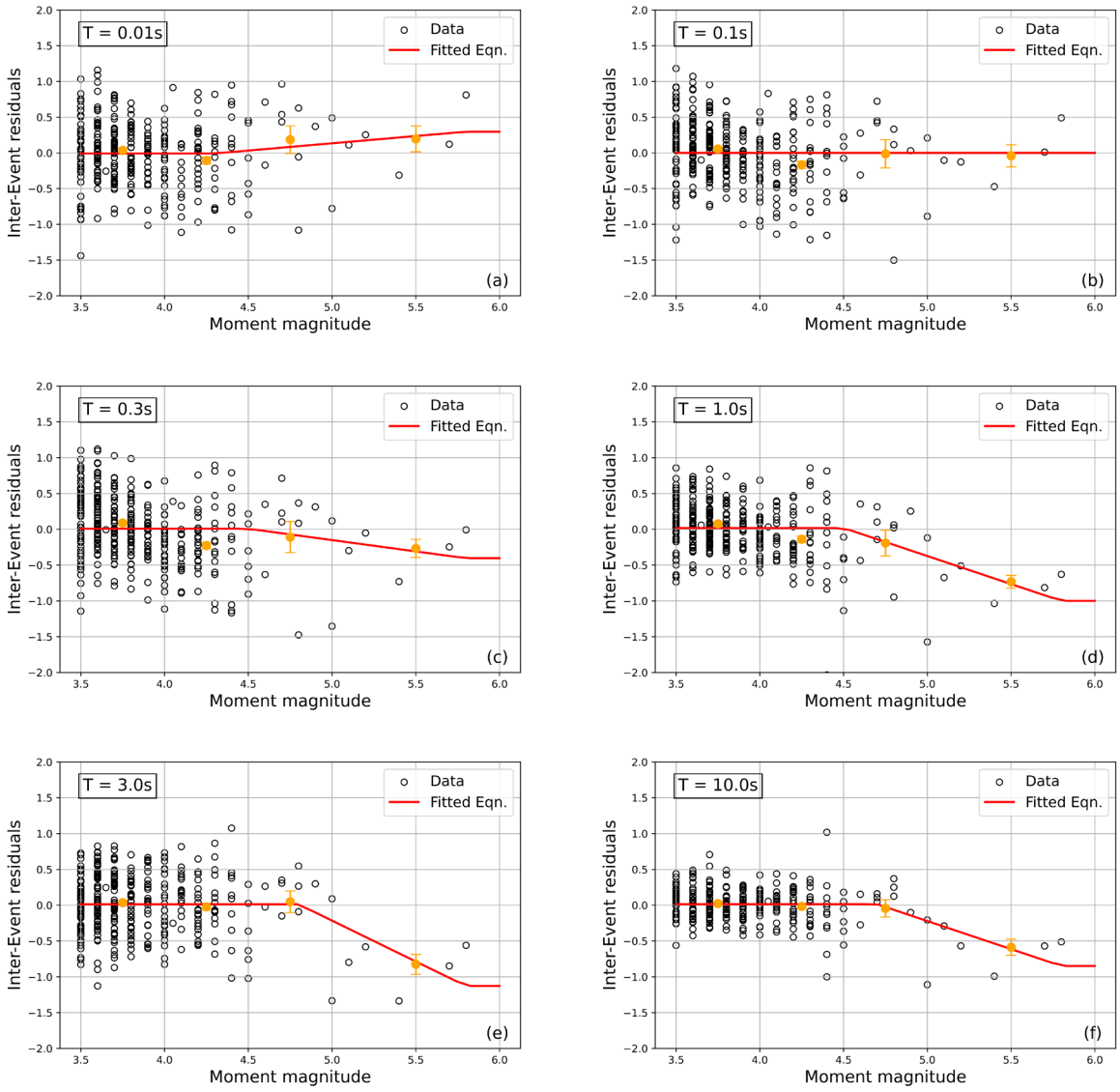

Figure 5.7 Inter-event residual against moment magnitude and fitted magnitude adjustment factor F_M for periods T=0.01, 0.1, 0.3, 1.0, 3.0, 10.0s.

5.4.2 Distance Adjustment

After correcting the trend in magnitude using the magnitude adjustment factor F_M, we investigate the distance scaling effect by plotting the updated intra-event residual $\varepsilon_{i,j}$ against rupture distance R_{rup}, as shown in Figure 5.8. For T < 0.3s, the intra-event residual becomes more positive with decreasing R_{rup} for $R_{rup} < \sim 20km$, indicating larger ground motions than predicted by the NGA-East GMM. Again, similar positive residuals at shorter periods (T=0.05-1.0s) were observed by Zalachoris and Rathje (2019). This trend is potentially associated with the shallower focal depths of the events in the study region compared to the broader CENA region (Zalachoris and Rathje 2019) or the fact that these smaller events show less near-source distance saturation. One

notable trend for the T = 0.01 s data is the systematically negative residuals between R_{rup} ~ 20 – 60 km. This negative bias decreases with increasing period and becomes insignificant at periods greater than 0.05s, but it is not modeled in the distance adjustment below. For middle periods (T ~ 0.3 s), the residuals at shorter distances become zero and for longer periods a negative trend is observed for smaller R_{rup}.

For both the positive trend at shorter periods and the negative trend at longer periods, we use a three-segment piecewise linear model to fit the distance adjustment factor F_R, as defined by Equation 5.8:

$$F_R = \begin{cases} \alpha * \ln\left(\frac{R_1}{R_2}\right) & R_{rup} < R_1 \\ \alpha * \ln\left(\frac{R_{rup}}{R_2}\right) & R_1 \leq R_{rup} < R_2 \\ 0.0 & R_{rup} \geq R_2 \end{cases} \quad (5.8)$$

where R_1, R_2, and α are regression coefficients for F_R. The parameter R_1 is the distance below which F_R is constant, R_2 is the distance above which F_R is equal to 0.0, and α represents the slope for F_R as a function of R_{rup} between $R_1$and R_2. To obtain the values of the coefficients, the hinge distances $R_1$and R_2 are first specified and a least squares regression is conducted to obtain α. Then $R_1$and R_2 are varied within a given range to search for the combination of R_1, R_2, and α that achieves the least squared error. It should be noted that the slope α is smaller than 0 for T < 0.25 s to fit the positive residuals at short distance, and α is greater than 0 for T=0.75-5.0 s to fit the negative residuals at short distances. For some periods, the intra-event residual is approximately zero for all R_{rup} values and no correction for distance is applied for those periods. The fitted F_R relationships are plotted in Figure 5.8.

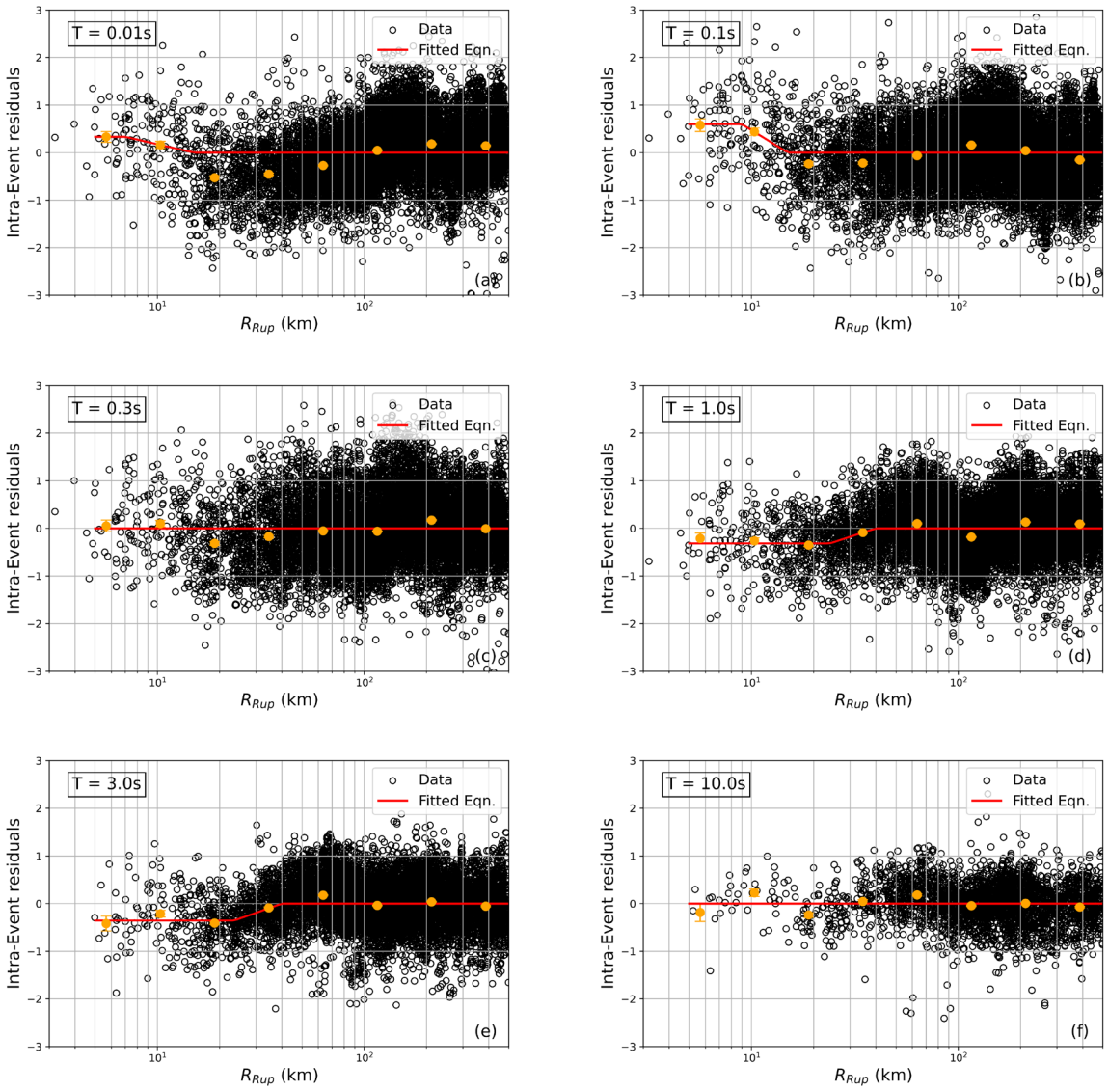

Figure 5.8 Intra-event residuals against rupture distance and fitted distance adjustment factor F_R for periods T=0.05, 0.1, 0.3, 1.0, 3.0, 10.0s.

5.4.3 Site Adjustment

To evaluate the site adjustment, the distance adjustment factor F_R is subtracted from the updated intra-event residuals ($\varepsilon_{i,j}$) and the resulting intra-event residuals are plotted against V_{S30}, as demonstrated in Figure 5.9. In general, the intra-event residuals decrease with increasing V_{S30} for all periods, but the slope of that relationship is relatively flat. Additionally, as observed by Parker et al. (2019), the site amplification effect for the CENA region does not increase with decreasing V_{S30} at the smallest V_{S30}, but rather there is a flat trend at V_{S30} less than about ~ 500 m/s. These trends are different from the general site amplification effects in active tectonic regions and

suggests that the predictive power of V_{S30} may not be as significant for sites in CENA as it is in active regions.

We utilized the same functional form as used by Parker et al. (2019) to define the site amplification factor F_V:

$$F_V = \begin{cases} c * \ln\left(\frac{V_1}{V_{ref}}\right) & V_{S30} \leq V_1 \\ c * \ln\left(\frac{V_{S30}}{V_{ref}}\right) & V_1 < V_{S30} \leq V_2 \\ c * \ln\left(\frac{V_2}{V_{ref}}\right) & V_{S30} > V_2 \end{cases} \quad (5.9)$$

where V_{ref}, V_1, V_2, and c are coefficients for the F_V relationship. V_{ref} is the reference velocity at which $F_V = 0$ and is constrained to be 760 m/s by shifting the intra-event residual with a constant, V_1 is the V_{s30} below which F_V is flat, V_2 is the V_{s30} above which F_V is flat, and c is the slope of F_V in the range of $V_1 < V_{S30} \leq V_2$. Because the dataset does not have recordings with $V_{S30} \geq 2000$ m/s, the value of V_2 is set to be 2000 m/s with reference to Parker et al. (2019). The other coefficients are fit in the manner that the value V_1 is specified and c is obtained by applying least squares regression. V_1 is then varied within the range between 280 and 500 m/s to find the optimum V_1 that gives the smallest least squared error. Examples of the fitted F_V are shown in Figure 5.9.

The F_V model obtained from the process above has a value of 0 at V_{S30} = 760 m/s, which is consistent with the definition of the F_V portion of the NGA-East site amplification model which has reference condition at V_{S30} = 760 m/s. Thus, the F_V represents the site amplification at a site V_{S30} with respect to V_{S30} = 760 m/s.

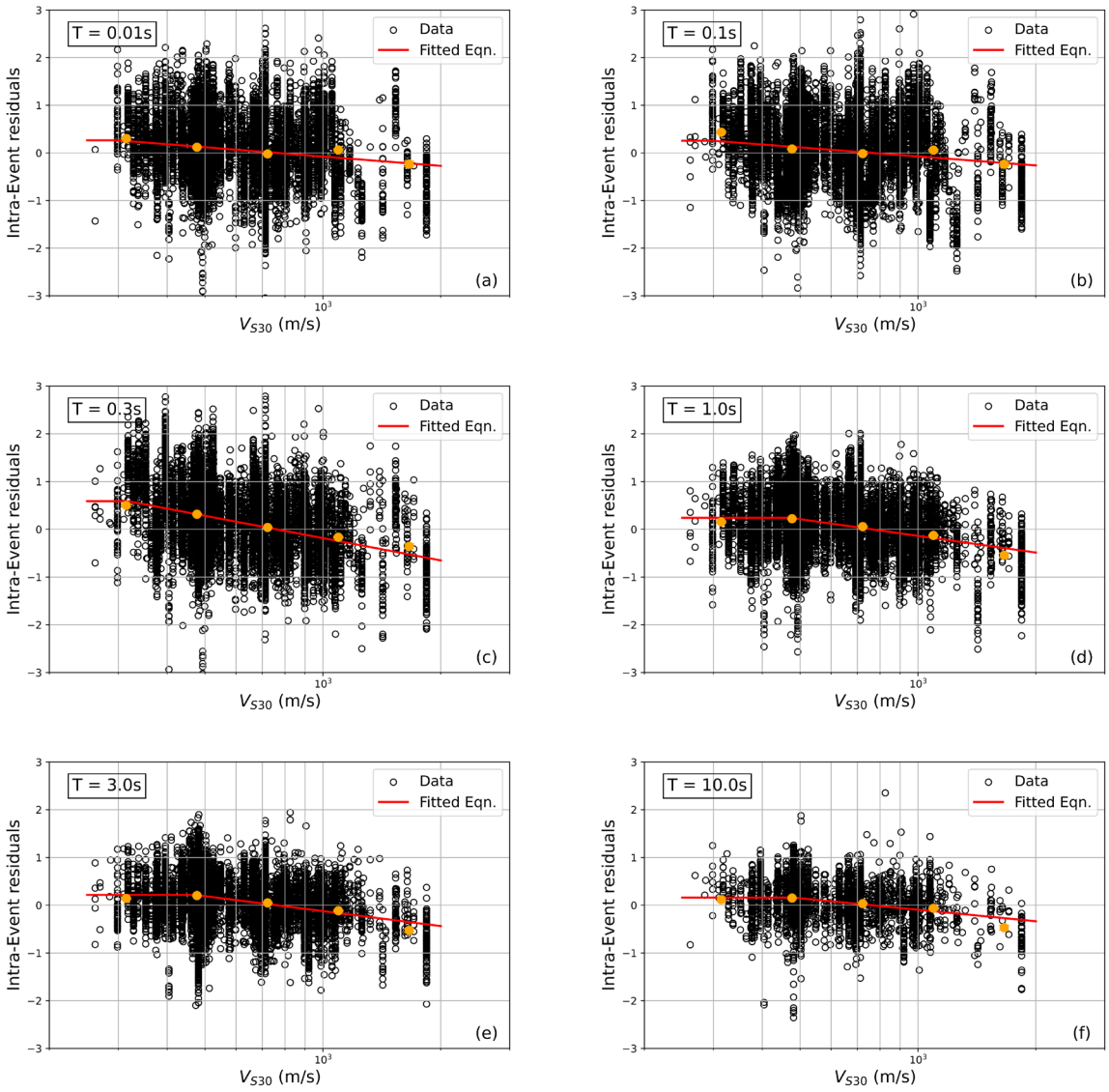

Figure 5.9 Intra-event residual against V_{S30} and fitted site amplification factor F_S for periods T=0.01, 0.1, 0.3, 1.0, 3.0, 10.0s.

5.4.4 Overall Combined Adjustments

After the iterative derivation of F_M, F_R, and F_V, we obtain the adjustment factor to the overall bias C_{adj}, as defined in Equation 5.3. Because the residual $lnY_{i,j}$ defined in Equation 5.1 is computed without consideration of the F_{760} factor, C_{adj} represents the amplification from $V_{S30} = 3000$ m/s to $V_{S30} = 760$ m/s (i.e., F_{760}) as well as the overall bias of the data relative to the NGA-East weighted mean GMM. A detailed discussion of C_{adj} is provided in the next section.

Table 5.1 summarizes the final coefficients for each of the adjustments. The overall adjustment factor lnF can be computed using Equation 5.3. The updated GMM of TOK is established by

adjusting the prediction from the NGA-East weighted mean GMM using the overall adjustment factor:

$$IM_{TOK} = exp\left(C_{adj} + F_M + F_R + F_V\right) * IM_{NGA-E} = F * IM_{NGA-E} \quad (5.10)$$

Table 5.1 Model Coefficients

Period (s)	M_b	b_0	b_1	α	R_1	R_2	V_{ref}	V_1	V_2	c	C_{adj}
0.01	4.3	-0.008	0.203	-0.435	7.0	15.0	760	298	2000	-0.282	-0.505
0.02	4.3	-0.012	0.286	-0.453	7.0	15.0	760	298	2000	-0.257	-0.845
0.025	4.1	-0.020	0.274	-0.588	7.0	15.0	760	298	2000	-0.221	-0.916
0.03	4.1	-0.020	0.276	-0.781	7.0	15.0	760	298	2000	-0.225	-0.950
0.04	4.1	-0.015	0.206	-1.305	8.5	15.0	760	298	2000	-0.236	-0.883
0.05	0.0	-	-	-1.364	8.5	15.0	760	298	2000	-0.250	-0.748
0.075	0.0	-	-	-1.414	9.0	15.0	760	298	2000	-0.180	-0.240
0.1	0.0	-	-	-1.169	9.0	15.0	760	298	2000	-0.273	-0.007
0.15	0.0	-	-	-0.790	9.0	15.0	760	298	2000	-0.354	0.250
0.2	0.0	-	-	-0.626	9.5	15.0	760	299	2000	-0.512	0.304
0.25	0.0	-	-	0.000	-	-	760	318	2000	-0.612	0.375
0.3	4.5	0.007	-0.317	0.000	-	-	760	8	2000	-0.674	0.357
0.4	4.5	0.009	-0.400	0.000	-	-	760	318	2000	-0.586	0.397
0.5	4.5	0.012	-0.533	0.000	-	-	760	439	2000	-0.558	0.445
0.75	4.5	0.017	-0.746	0.493	24.5	45.0	760	450	2000	-0.516	0.604
1.0	4.5	0.018	-0.783	0.620	24.0	40.0	760	472	2000	-0.504	0.684
1.5	4.6	0.015	-0.814	0.507	22.5	45.0	760	469	2000	-0.530	0.758
2.0	4.7	0.014	-1.014	0.569	23.0	40.0	760	471	2000	-0.442	0.700
3.0	4.8	0.012	-1.141	0.671	23.5	40.0	760	472	2000	-0.451	0.932
4.0	4.7	0.010	-0.710	1.179	27.0	35.0	760	469	2000	-0.432	0.989
5.0	4.7	0.008	-0.544	0.000	-	-	760	461	2000	-0.375	1.022
7.5	4.7	0.009	-0.565	0.000	-	-	760	457	2000	-0.321	1.029
10.0	4.7	0.014	-0.784	0.000	-	-	760	481	2000	-0.347	0.989

5.5 Discussion

5.5.1 Implications for site amplifications in CENA

The components of the adjusted TOK GMM that represent site amplification are the site adjustment F_V that represents the site amplification relative to $V_{S30} = 760$ m/s and the overall bias adjustment C_{adj}. Note that the C_{adj} does not only represent bias in the TOK data relative to the NGA-East median GMM, but it also includes any site amplification effects not captured by F_V, which is the site amplification at $V_{S30} = 760$ m/s relative to the reference hard rock site condition

of $V_{S30} = 3000$ m/s, i.e., F_{760}. We are not able to fully distinguish for C_{adj} the influence of the F_{760} factor from the influence of overall differences in TOK data that are not related to site amplification.

The period-dependent C_{adj} values are shown in Figure 5.10 along with the simulation-based F_{760} models provided in Stewart et al. (2020) for impedance ($F_{760,\mathrm{imp}}$) and gradient ($F_{760,\mathrm{gr}}$) conditions. For periods smaller than 0.1 s, the C_{adj} values show a generally similar shape as the gradient F_{760} model, where the values reach a minimum at a period of about 0.03 s and then increase as periods gets longer. However, the minimum value of C_{adj} (~ -1.0) is significantly smaller than the minimum $F_{760,\mathrm{gr}}$ (~0.0), with the values of C_{adj} indicating strong de-amplification at these shorter periods. The large negative C_{adj} in the short period range indicates that the $\kappa_0 = 0.006$ s assumed for the reference condition is not appropriate for the data, which is dominated by recordings with V_{s30} = 400 – 800 m/s (Figure 5.4). A small value of κ_0 generates a response spectrum that peaks at short periods, and if the recordings do not show the same peak at short periods, the empirical adjustment will show significant de-amplification at these periods.

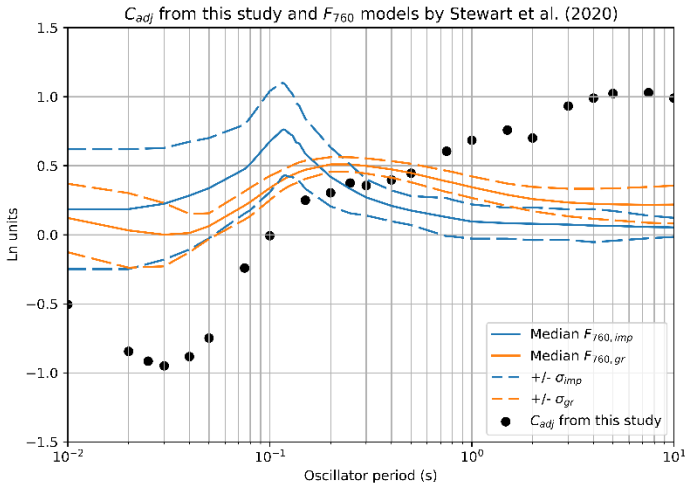

Figure 5.10 The overall bias, C_{adj}, for the reference empirical adjustment along with the simulation-based F_{760} models provided in Stewart et al. (2020).

Figure 5.11 plots response spectra for an M_W = 5.0 event at R_{rup}= 10 km based on different adjustments to the NGA-E weighted median GMM. Response spectra are shown for the NGA-E reference condition of V_{S30} = 3000 m/s, the NGA-E reference condition adjusted to V_{S30} = 760 m/s with the Stewart et al. (2020) F_{760} models for gradient and impedance conditions, and the NGA-E reference condition adjusted with the C_{adj} factors developed in this study. The spectrum for the NGA-E reference condition of V_{S30} = 3000 m/s peaks at a period of about T ~ 0.04s and after applying the Stewart et al. (2020) F_{760} models, the response spectra peak at periods of about T ~ 0.07 and 0.05 s for the gradient and impedance F_{760} models, respectively. The F_{760} adjustment is largest between 0.1 and 1.0 s (Figure 5.10), and thus the spectral accelerations are amplified

the most in this period range for the V_{S30} = 760 m/s condition in Figure 5.11. When the C_{adj} factors are applied to the NGA-E reference condition, the spectral shape changes considerably with the peak shifting to T ~ 0.1-0.15 s and the spectrum displaying a concave up shape at short periods. This spectral shape is more consistent with larger κ_0. Boore and Campbell (2017) suggested that ground motions at sites with V_{S30}= 760 m/s in CENA can be represented by κ_0 between 0.01 and 0.03 s, which indicates that the C_{adj} factors at short periods represent the F_{760} effects associated with κ_0.

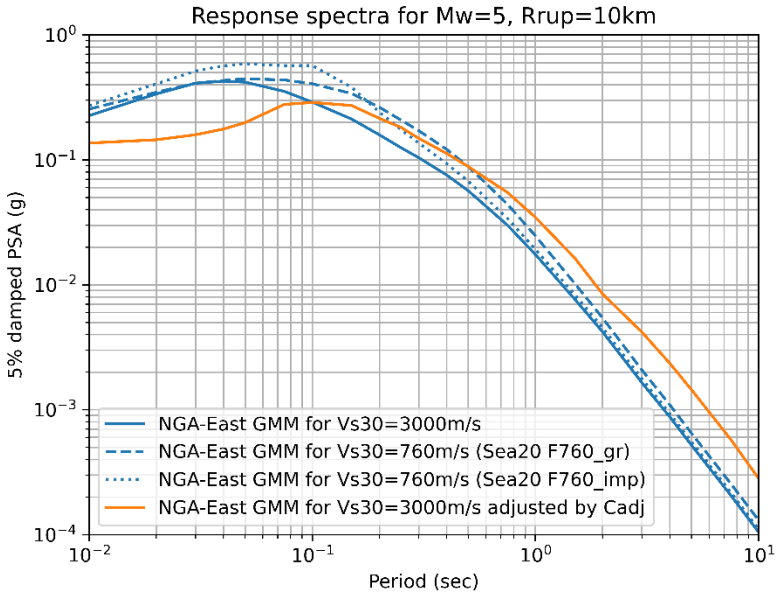

Figure 5.11 Predicted response spectra for M_w = 5 at R_{rup} = 10 km from NGA-E GMM reference condition (V_{S30}=3000 m/s), NGA-E GMM reference condition adjusted using Stewart et al. (2020) F_{760} gradient and impedance models, and NGA-E GMM reference condition adjusted using C_{adj} from this study

At longer periods the C_{adj} factors are positive, with C_{adj} ~ +0.4 between T = 0.15 and 0.5 s and increasing to C_{adj} ~ +1.0 at T > 3.0 s. The C_{adj} values between T = 0.15 and 0.5 s are similar to the simulation-based F_{760} models, but the C_{adj} values at longer periods are much larger than the F_{760} models. The F_{760} models reach a peak between periods of 0.1 s and 0.3 s and then decay towards zero, which is consistent with 1D site response in which amplification trends towards 1.0 at periods much longer than the fundamental site period. The large C_{adj} factors at long periods result in a significant increase in the spectral acceleration relative to the NGA-E reference condition (Figure 5.11).

There are various potential reasons for the large values of C_{adj} at long periods and the discrepancy with the F_{760} models. As discussed in Chapter 4, the site amplification models of Western North America (WNA) were used to correct the CENA data to reference hard rock condition when developing the NGA-East GMMs, and the difference between the WNA and CENA

site amplification models can generate a bias. This issue may explain some of the bias in Figure 5.10, but the values of C_{adj} are too large to be solely attributed to the difference in WNA and CENA site amplification models. Alternatively, issues with **M** determination may be contributing to the long period bias. Long periods are controlled predominantly by the seismic moment of the source and an increase in M_W of just 0.2 magnitude units can increase the long period response spectral ordinates by almost a factor of 2.0, such that the large C_{adj} values may indicate a bias in our **M** estimates.

Finally, we also considered if the positive C_{adj} at longer periods may be associated with sampling bias, as the weaker ground motion recordings are more likely to be rejected due to the presence of low frequency noise, leaving more ground motions with greater amplitude in the dataset and thus positive overall bias. However, because the value of C_{adj} is already large at T = 3.0 s where the influence of sampling of data is small (see Figure 5.5), we think this factor is not likely the cause for the large bias at long periods.

The F_V component of the site amplification model derived from this study is compared with the site amplification models of ZR19 and from Parker et al. (2019, Pea19) in Figure 5.12. The F_V site amplification model developed in this study compares favorably to Pea19 for most periods, with the exception at T=0.3s (Figure 5.12b) where the V_{S30} scaling from this study is more significant than that of Pea19. For the other periods the slope of the V_{S30} scaling from this study is similar to that in Pea19, but Pea19 shows that the linear scaling of amplification with V_{S30} continues to smaller values of V_{S30} (~ 300 m/s) before it goes flat. It is possible that the V_{S30} scaling for softer sites is not well captured by the dataset used in this study for TOK because of the paucity of data with V_{S30} less than 280 m/s. The site amplification represented by the ZR19 model indicates slightly steeper slopes than the other two models, this is because the ZR19 model was adjusted from the site amplification model for Boore et al. (2014, BSSA14), which is for active tectonic regions that is characterized by a stronger V_{S30} effect. Nonetheless, the overall site amplification levels suggested by the three models are similar.

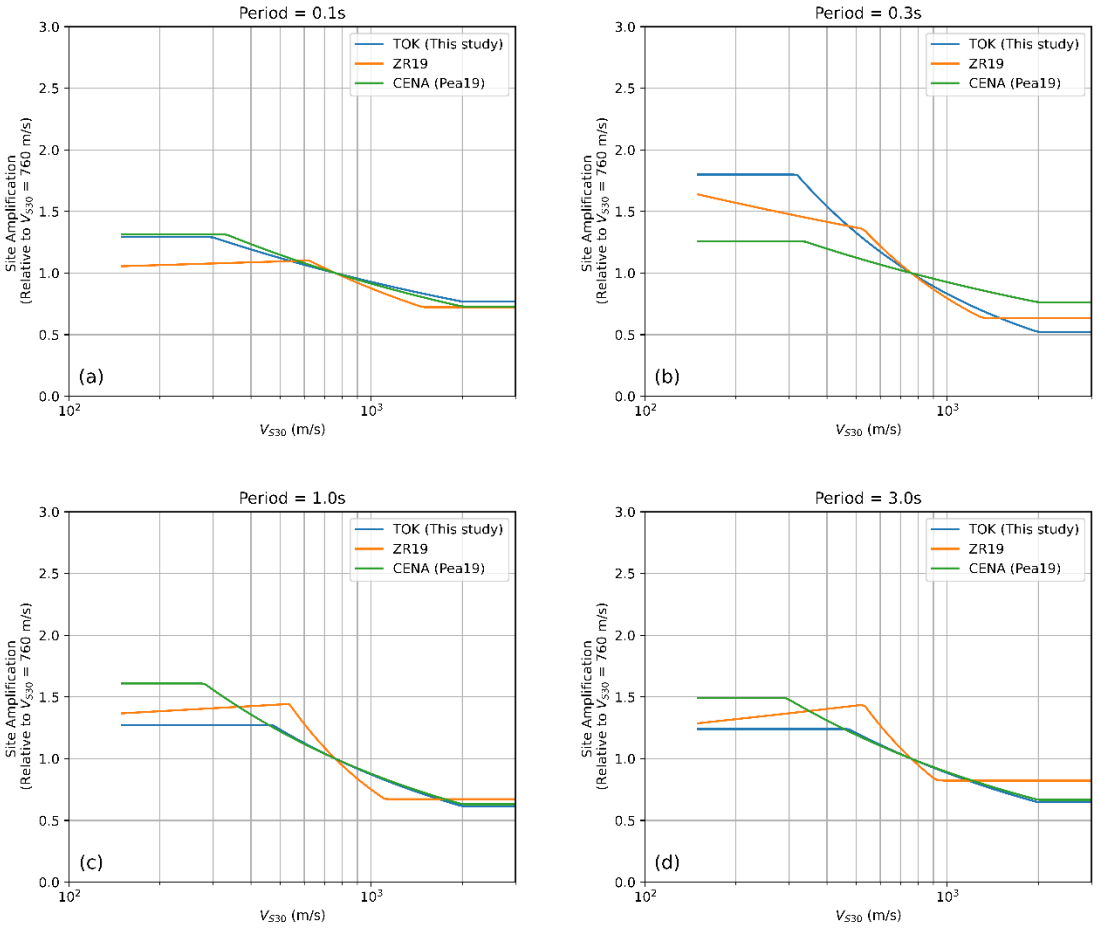

Figure 5.12 Comparison between site amplification model of the new GMM, ZR19, and NGA-East GMM linear site amplification model.

5.5.2 Comparison of proposed TOK GMM to prior models

We examine the adjusted GMM by comparing the ground motions predicted by the new GMM for TOK with predictions by ZR19 and the weighted median NGA-East GMM for **M** 4.0, which is approximately the average magnitude for the dataset. The results are shown in Figure 5.13 for $V_{S30} = 760$ m/s, with the data from the recordings also shown. The ground motion data are corrected to $V_{S30} = 760$ m/s using the F_V models developed in this study (e.g., Figure 5.9). For the NGA-East GMM prediction in Figure 5.13, the F_{760} for both the gradient and impedance conditions suggested by Stewart et al. (2020) are used to provide predictions for $V_{S30} = 760$ m/s.

The predictions from ZR19 and the GMM from this study are very similar to each other, which is at least partially explained by the overlap in data and because both models are developed using data from TOK. However, only 25% of the data from this study was used in Zalachoris and Rathje (2019), such that the overlap is relatively small. Both ZR19 and the new GMM predict weaker ground motions than the NGA-East GMM at shorter periods (0.05 s and 0.1 s) and stronger ground motions than the NGA-East GMM at longer periods (T > 1.0 s). These differences are a

result of the negative overall bias factor C_{adj} at short periods (T ≤ 0.1 s) and the positive C_{adj} at periods longer than about 0.1s (Figure 5.10). There is a slight difference between ZR19 and the new GMM at shorter distances between 5-50 km, where the new GMM predicts relatively larger ground motions than ZR19 at shorter periods (T < 1.0 s) and fits better with the trend shown by the ground motion data.

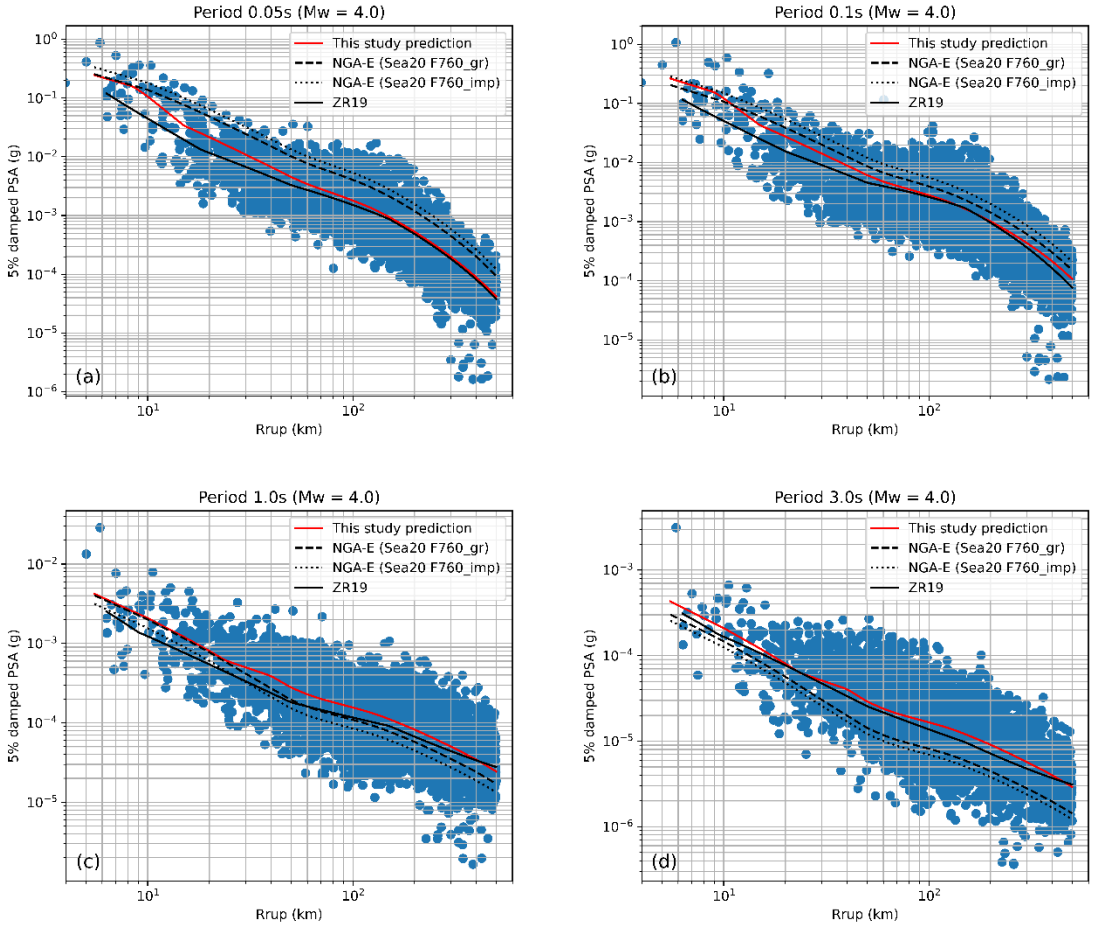

Figure5.13 Comparison between ground motion data with 3.75<M<4.25 and ground motion predicted by the new GMM, ZR19, and the weighted median NGA-East GMM for **M**=4.0 and for $V_{S30} = 760m/s$.

6 Large-scale 1D Site Response Simulations

6.1 Previous F_{760} models

This section provides an overview of previous research efforts on the development of simulation-based correction factors (F_{760}) used to adjust ground-motion intensity measures from the reference condition of V_S = 3000 m/s to V_{S30} = 760 m/s, taking into consideration the evaluation presented by Stewart et al. (2020). Stewart et al. (2020) evaluated four studies, Boore and Campbell (2017), Darragh et al. (2015), Harmon et al. (2019a, 2019b), and Frankel et al. (1996), as part of the evaluation of previously developed F_{760} models.

Boore and Campbell (2017) produced site amplification factors using the square-root impedance (SRI) method. This study used fourteen (14) sites representative of CENA conditions, with V_{S30} values within 10% of 760 m/s, to derive Fourier Amplitude Spectra (FAS) amplification factors as a function of frequency. The amplification factors were coupled with point source simulated reference site ground motion Fourier amplitudes for different magnitudes and distances, as well as different κ_0 estimates, to produce ground surface Fourier amplitudes. Both the ground surface and reference site (V_S = 3000 and κ_0 = 0.006 sec) FAS were converted to various intensity measures (Sa, PGV, PGV) using RVT and their ratios used to define the amplification (from 3000 to 2000 and 760 m/s). Boore and Campbell (2017) provide adjustment factors for sites with different reference conditions (V_{S30} = 760, 2000, and 3000 m/s) and a broad range of high-frequency spectral decay parameter (κ_0), as well as events with moment magnitudes between **M** = 2 and **M** = 8, and rupture distances ranging between 2 and 1200 km. Stewart et al. (2020) only considered κ_0 values of 0.01, 0.02 and 0.03 s and emphasized larger magnitudes and closer distances due to those conditions generally being hazard-critical.

Darragh et al. (2015), referred to as PEA (Pacific Engineering and Analysis) by Stewart et al. (2020), also calculated site amplification factors from a series of point-source stochastic ground response analyses performed in the frequency domain with RVT applied to compute intensity measures. The ground response simulations used profiles with V_{S30} values ranging from 180 m/s to 2032 m/s to reflect the structure of the crust in Western North America (WNA). These profiles were then underlain by a hard rock crustal model in order for them to be applicable to CENA conditions. 53 earthquake events with moment magnitudes ranging from **M** = 4.5 to 8.5, and rupture distances up to 1000 km were used. For evaluation of F_{760} models, Stewart et al. (2020) only considered 3 profiles from PEA, namely, the glacial till, Piedmont saprolite, and a weathered rock gradient, which are all sites where V_{S30} = 760. In terms of κ_0, these sites adopted a κ_0 value of 0.02 s.

Harmon et al. (2019a, 2019b), as part of the research efforts from the NGA-East Geotechnical Working Group, developed site amplification models that consider linear and nonlinear effects based on 1,747,278 1D linear elastic, equivalent linear, and nonlinear ground response analysis. The simulation tree was designed to capture the variability in site conditions at CENA as well as the uncertainty in soil properties at individual sites. A total of 247 rock outcrop motions were used.

For the development of F_{760} models, a subset of profiles was developed. This subset of profiles consisted of the profiles with V_{S30} ranging between 700 and 800 m/s. The simulations conducted in this study used the Campbell (2009) Q-Vs damping model, thus, no κ_0 value was specified.

Lastly, Stewart et al. (2020) re-conducted the Frankel et al. (1996) study using the square-root impedance (SRI) approach. The profile used represents a gradual increase in shear wave velocity as a function of depth. The process by which the amplification factors was derived using that profile matches what is described above for Boore and Campbell (2017). Stewart et al. (2020) re-analyzed this profile using input motions for moment magnitudes ranging from **M** = 4.5 to **M** = 6.5, and rupture distances of 10, 50, and 100 km, along with two values of κ_0 = 0.01 s and 0.02 s.

Table 6.1 summarizes the previous studies along with their characteristic features; however, there are a series of limitations associated with these studies:

- The V_S profiles used in the simulations used to calculate F_{760} should have V_{S30} values near 760 m/s, and should achieve the reference condition of 3000 m/s. The profiles from prior work were almost entirely generated through the application of judgment due to the lack of measured profiles that satisfied this condition.
- The majority of the simulations used to derive F_{760} use the square-root impedance method (Boore, 2013). More rigorous ground response analysis, such as those presented in Harmon et al. (2019a, 2019b) were only used for the impedance model because of the lack of gradient-type profiles in this study.
- The material damping used in the simulations leads to κ_0 values that may be too low considering the findings from the latest efforts on understanding κ_0, as discussed in Xu et al. (2020).

The present study continues the efforts of the NGA-East GWG and improves the previous work by:

- Using a broader range of site conditions (Ilhan, 2020) represented by a higher number of unique profiles representative of CENA conditions that aim to remove constraints in variability as well as the bias observed in the generic profiles from Harmon et al. (2019a, 2019b).
- Achieving κ_0-informed simulations by scaling small-strain damping (D_{min}) to capture a target range of κ_0 values.
- Incorporation of measured V_S profiles in the areas of Texas, Oklahoma, and Kansas as part of the parametric study tree.

Table 6.1 Prior F_{760} studies

Study	Type of Simulation	κ_0	Input Motions
Boore and Campbell (2017)	Square-root Impedance Method	κ_0 = 0.01 s, 0.02 s, and 0.03 s	Events with moment magnitudes between **M** = 2 and **M** = 8, and rupture distances ranging between 2 and 1200 km
Darragh et al. (2015)	Equivalent-linear ground response with RVT	κ_0 = 0.02 s	Events with **M** = 4.5 to 8.5, and rupture distances up to 1000 km
Harmon et al. (2019a, 2019b)	1D Linear Elastic, Equivalent Linear and Nonlinear Ground Response Analysis	Not specified but estimated from viscous damping.	Events with **M** = 4 to 7+, and rupture distances up to 100 km
Frankel et al. (1996) (Re-done in Stewart et al. (2020)	Square-root Impedance Method	κ_0 = 0.01 s and 0.02 s	**M** = 4.5 to **M** = 6.5, and rupture distances of 10, 50, and 100 km

6.2 Suite of Rock Outcrop Motions

The present work uses the rock outcrop motion dataset, which was developed in Harmon et al. (2019), and was adopted by Ilhan (2020) to perform one-dimensional (1D) nonlinear, equivalent-linear and linear site response simulations for Central and Eastern North America (CENA). This database consists of two different sets of input motions: (i) the first set is composed of 186 synthetic and recorded outcrop motions from NUREG-6729 (McGuire et al., 2001), and (ii) the second set is composed of 61 motions stochastically generated by SMSIM (Boore, 2005). A total of 247 outcrop rock motions representative of CENA were utilized to represent a broad range of ground motion intensities.

The first set of motions (NUREG-6729) were developed to be representative of Western United States (WUS) but were modified to incorporate more high-frequency content to capture the reference rock conditions at CENA, which has shear wave velocity (V_S) of 3000 m/s (Hashash et al., 2014) and $\kappa_{0,rock}$ (the high frequency spectral decay parameter for reference rock) of 0.006 sec (Campbell et al., 2014). The NUREG-6729 set consists of 93 motion pairs and 10 different moment magnitude (**M**) and rupture distances (R) pairs, namely **M** = 4.5 to 7+, and R = 0-to-100 km. The stochastically generated SMSIM motions (Boore, 2005) were produced to supplement the PGA and PGV values from the NUREG-6729 motions.

The response and Fourier Amplitude Spectra for the NUREG-6729 and SMSIM rock outcrop motions are presented in Figure 6.1. Moreover, peak ground velocity (PGV) and peak ground displacement (PGD) as a function of peak ground acceleration (PGA) are shown in Figure 6.2.

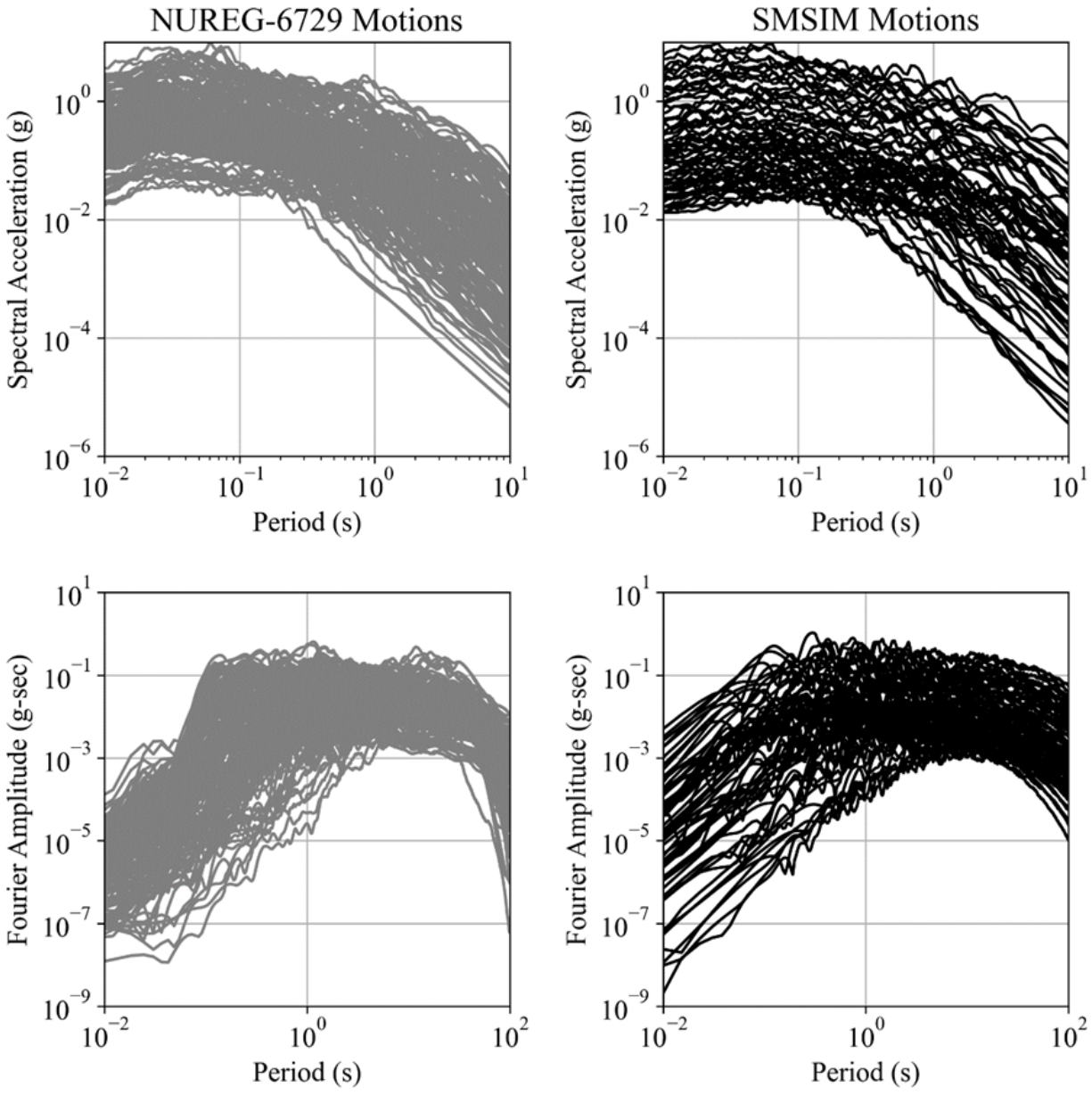

Figure 6.1 Response and Fourier Amplitude Spectra for NUREG-6729 and SMSIM motions

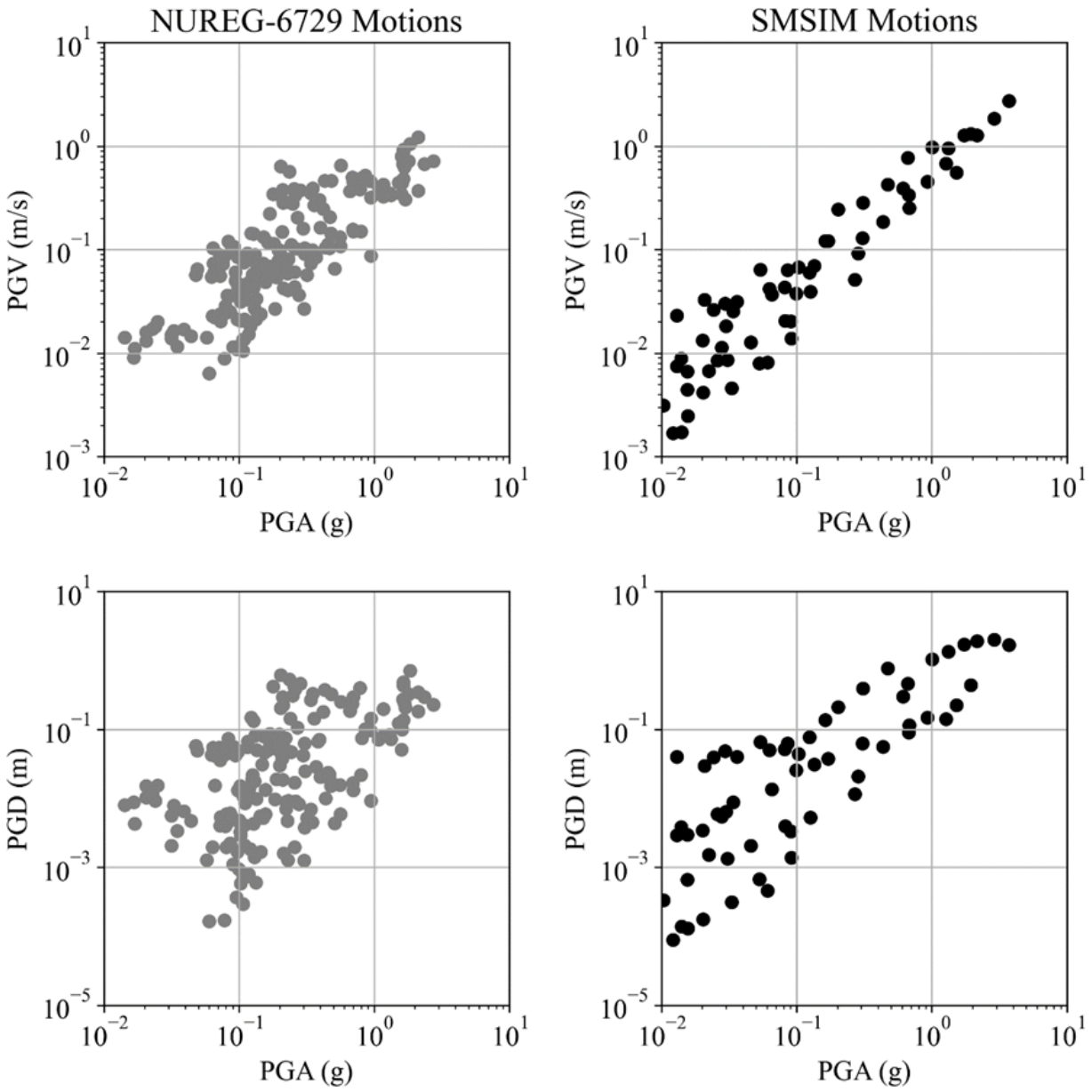

Figure 6.2 PGV vs PGA, and PGD vs PGA for NUREG-6729 and SMSIM motions

6.3 Parametric Study Tree

6.3.1 Overview of Parametric Study Tree

A large-scale parametric study of one-dimensional (1D) site response analysis (SRA) was conducted to simulate the uncertainty and variability of soil conditions in CENA. The results of these simulations were used to develop F_{760} results that can be used in model development. F_{760} is the correction factor to adjust the site amplification for V_{S30} = 760 m/s relative to a CENA reference of V_S = 3000 m/s. The parametric study tree (Figure 6.3) consists of two branches: 1)

the upper branch, which includes the 1D analyses from Ilhan (2020), and 2) the lower branch which is composed of simulations using V_S profiles located in Texas, Oklahoma and Kansas (TOK) region. The large-scale parametric study tree of Ilhan (2020) results in 1,218,945 nonlinear (NL), equivalent linear (EL), and linear (L) elastic frequency-domain analyses, respectively (adding up to 3,656,835 simulations in total). Moreover, the TOK profiles lead to 6,175 NL, EL, and L analyses (adding up to 18,525 SRAs in total).

The parametric study tree in the Ilhan (2020) branch was constructed considering three (V_S) horizons: i) soil (or sediment), underlain by ii) a Weathered Rock Zone (WRZ), which is the transition from soil to reference rock, underlain by iii) the CENA reference rock condition of V_S = 3000 m/s. Part (i) was represented by 10 geology-based representative seed V_S profiles from Harmon et al. (2019). The WRZ (Part ii) captures the observed V_S gradient of weathered rock profiles in CENA. These profiles were associated with a set of soil properties (unit weight, over-consolidation ratio (OCR), friction angle, and plasticity index (PI)) to compute shear strength and modulus reduction and damping (MRD) curves using the Darendeli (2001) model. Randomizations were applied to V_S and MRD to account for variability and uncertainty in site attributes. In aggregate, we consider 147,420 unique soil columns. The Ilhan (2020) parametric study tree can be detailed as follows:

- A total of 247 rock outcrop motions composed of i) 186 synthetic and recorded rock outcrop motions from NUREG-6729 (McGuire et al., 2001), ii) sixty-one (61) stochastically generated motions representative of CENA conditions (Boore, 2005).
- Thirteen (13) base case V_S profiles, that result from a combination of 10 seed V_S profiles, and 9 geology-dependent soil index and strength properties. These 13 base case V_S profiles are then used as reference profiles for the Toro (1995) randomization approach.
- Thirteen (13) randomizations of each combination of seed V_S profiles and geology-dependent soil properties.
- Three (3) randomizations of modulus reduction and damping curves using the systematically higher, systematically lower, and mean curves from Darendeli (2001)
- Eighteen (18) uniformly distributed WRZ for generic site profile truncation.
- Seven (7) WRZ horizons with their corresponding properties.

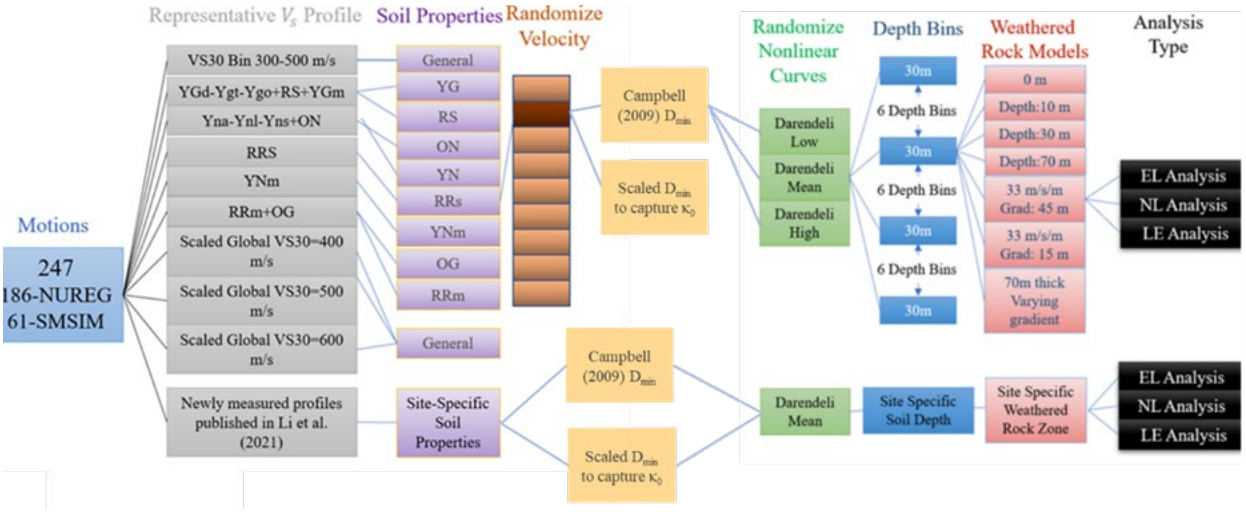

Figure 6.3 Large-scale parametric study

6.3.2 Randomized V_S profiles from Ilhan (2020)

The randomized (or generic) V_S profiles from Ilhan (2020) were produced using the representative seed V_S profiles from Harmon et al. (2019a), which were used as input to the Toro (1995) randomization approach. These seed profiles are listed along with their V_{S30} values in Table 6.2 and are shown in Figure 6.4. Harmon et al. (2019a) also suggested WRZ models dependent on weathered zone thickness, which ranges from 0 m (i.e. the sediment V_S profile is underlined by V_S = 3000 m/s) to variable thicknesses dependent on V_S gradient as depicted in Figure 6.5. All WRZ models in Harmon et al. (2019a) were adopted in Ilhan (2020), and the resultant generic profiles are demonstrated to include sharp impedance between soil V_S horizon and WRZ or between soil V_S and the reference condition of V_S = 3000 m/s. In addition to these impedance profiles, Ilhan (2020) introduced a new WRZ model (Figure 6.5) that linearly increases the V_S at the bottom of the soil region up to V_S = 3000 m/s condition to represent the CENA sites, which do not exhibit as sharp V_S impedance as the other WRZ models and are denoted as gradient profiles in Stewart et al. (2020).

Table 6.2 Representative seed V_S profile names for Ilhan (2020) and corresponding $V_{S,30}$ values. Please see the Table 6.3 for the explanation of the acronyms in the following table.

Representative seed V_S Profile	V_{S30} (m/s)
V_{S30} Bin = 300 – 500 m/s	383
RRs	356
Judgement Soft	148
Scaled Global Log-Mean to V_{S30} = 400 m/s	411
Scaled Global Log-Mean to V_{S30} = 500 m/s	513
Scaled Global Log-Mean to V_{S30} = 600 m/s	616
YNa-YNl-YNs +ON	252
YGd-YGt-YGo + RS + YGm	333
YNm	240
RRm+OG	391

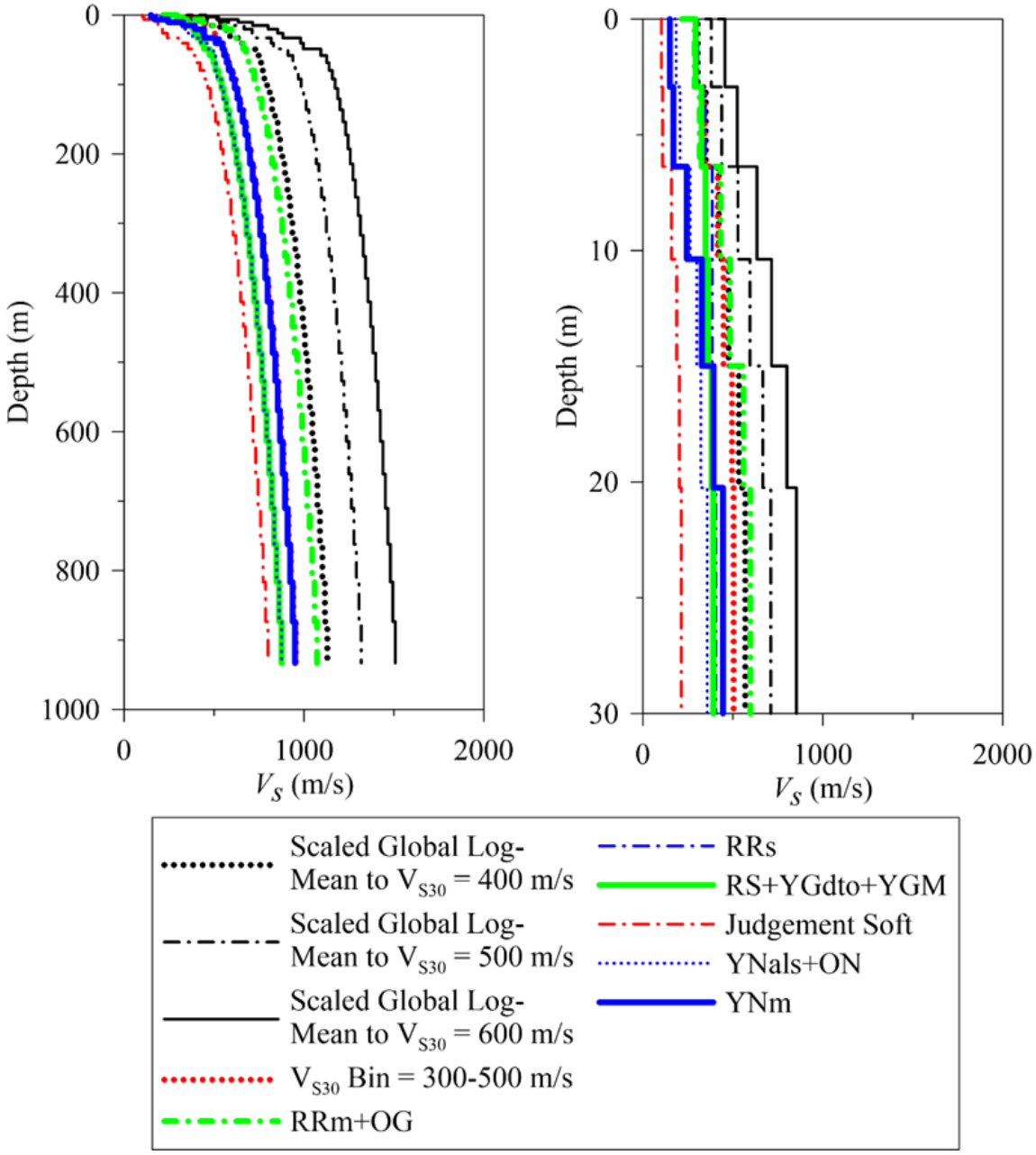

Figure 6.4 Representative seed V_S profiles from Ilhan (2020).

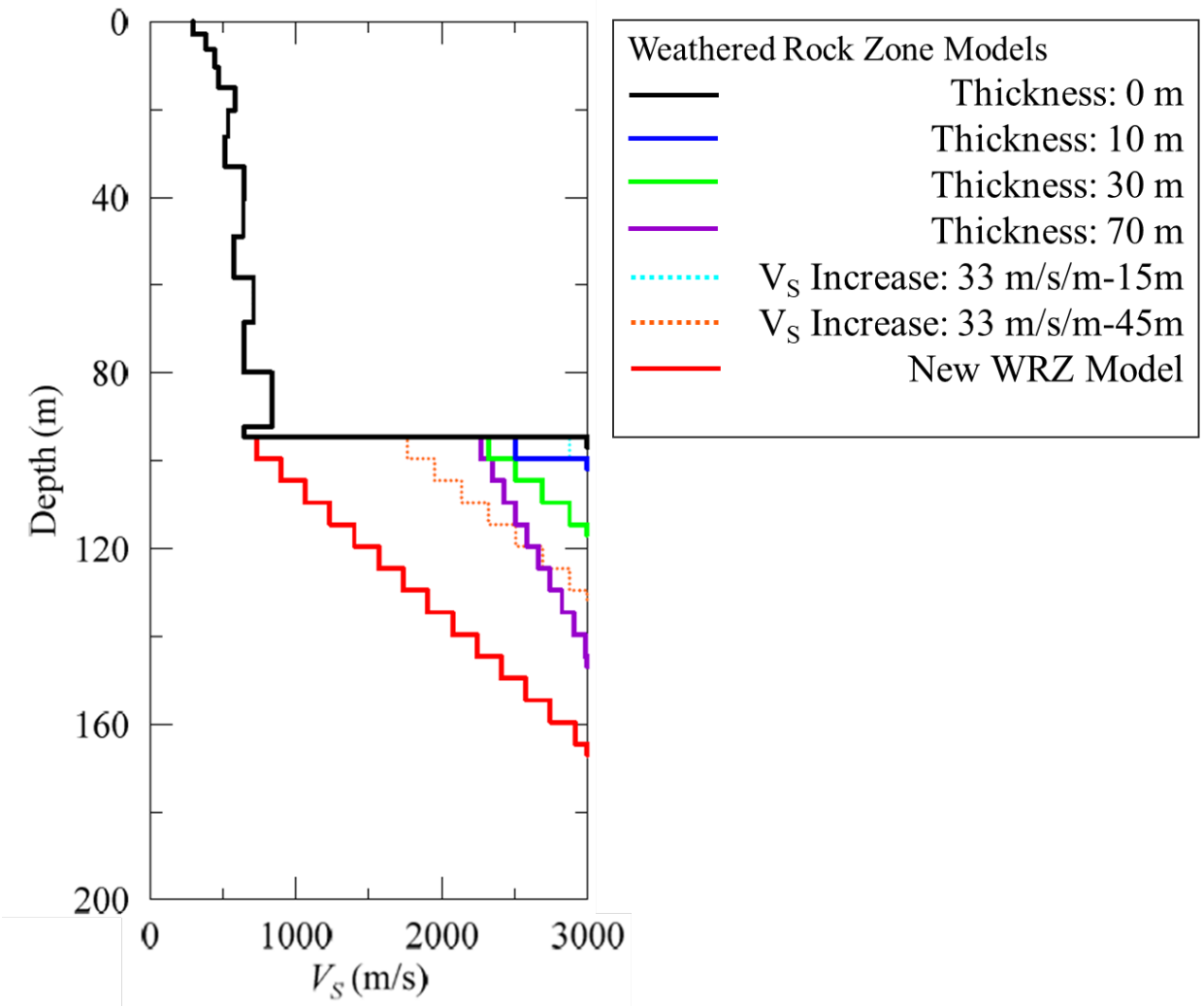

Figure 6.5 Weathered Rock Zone (WRZ) models from Ilhan (2020).

The uncertainty in site amplification models is separated in two components: a) epistemic uncertainty due to limitations in knowledge and data, and b) aleatory variability associated with natural randomness in a process (Rodriguez-Marek, 2020; Abrahamson, 2007). Such classification is applicable for V_S as follows:

- Epistemic uncertainty in V_S is addressed through the development of a series of representative V_S profiles, commonly referred to as seed or base-case profiles, along with upper/lower ranges considering ± 20% to 30%.
- The aleatory variability is addressed by generating a series of random realizations through Monte Carlo simulations.

The Toro (1995) approach, which consists of layering and velocity models, can be used to account for the aleatory variability. The layering model consists of a non-homogeneous Poisson process with a depth-dependent rate (Parzen, 1962) based on the assumption that layer thicknesses increase with depth. In this report we did not employ layer thickness randomization. The velocity

model proposed by Toro (1995) assumes a normalized quantity (Z_i) can be approximated as a log-normal distribution given by:

$$Z_i = \frac{\ln(V_i) - \ln(V_{median}(h_i)}{\sigma_{lnV}} \quad (6.1)$$

where V_i is the randomized V_S at the middle of the layer, V_{median} is the baseline V_S at the layer of interest and σ_{lnv} is the standard deviation of the V_S. The correlation between layers along with the distribution of V_S is characterized by an auto-regressive model given by:

$$Z_1 = \varepsilon_1 \quad (6.2)$$

$$Z_i = \rho Z_{(i-1)} + \sqrt{(1-\rho^2)}\, \varepsilon_i \quad (6.3)$$

where ρ is the interlayer correlation and ε_i is the independent random normal variable with zero mean and unit standard deviation. Ilhan (2020) introduced V_S reversals in the realizations by adopting a ρ value of 0.8 along with a σ_{lnv} value of 0.2 and utilized the Latin Hypercube Sampling Method to produce ε values instead of the Monte Carlo Sampling technique.

For the present study, the V_S realizations used to compute amplification factors are sampled from the complete set of Ilhan (2020) and are required to have V_{S30} values between 700 and 800 m/s to represent the profiles with V_{S30} = 760 m/s. Moreover, the classification of a profile as an impedance and gradient profile in the context of this report is as follows:

- An impedance profile is defined as follows:
  - For layers with V_S <400 m/s, followed by a layer with V_S of 3000 m/.
  - For layers with VS > 400 m/s and the next layer have a V_S greater than double the V_S value.
- Gradient profiles are those that do not meet the requirements of impedance profiles. Generally, these profiles have a gradual increase in V_S until the reference condition is achieved.

The simulations using two sets of profiles from Ilhan (2020), as shown in Figure 6.6a were exploited to develop F_{760} models.

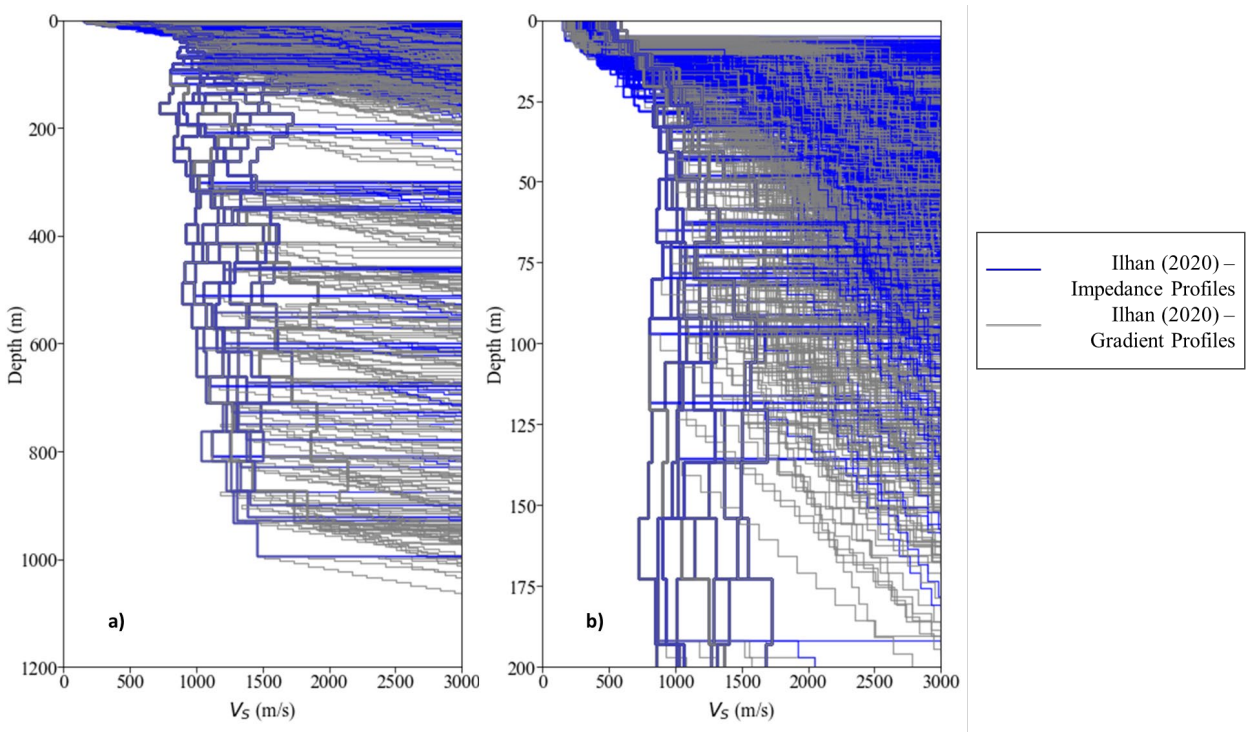

Figure 6.6 Generic profiles used for Ilhan (2020) at different depths: a) Profile depth up to 1200 m, and b) detailed view of the top 200 m.

6.3.3 Texas Oklahoma and Kansas (TOK) V_S profiles

6.3.3.1 Measured Profiles

The measured V_S profiles for the Texas, Oklahoma and Kansas were compiled from a series of openly accessible resource such as Yust (2018) for the Texas profiles, and Stephenson et al. (2021), Mendoza et al. (2017), and EPRI (2013) for the Oklahoma and Kansas profiles. The Texas profiles were derived using near surface seismic characterization, specifically from noninvasive active- and passive-source surface wave testing using a series of modal interpretations and inversion (Yust, 2018). The Oklahoma profiles, as presented in Stephenson et al. (2021), were collected using active-source refraction, reflection and Rayleigh-wave data for P-wave travel-time modeling and multichannel analysis of surface waves (MASW) (Stephenson et al., 2021, Mendoza et al., 2017). Table 6.3 shows the list of profiles used for the TOK branch, along with the V_{S30} values and their classification in terms of type of profile. The approach used to classify the profiles is consistent with that used for the Randomized V_S profiles for Ilhan (2020) branch.

Table 6.3 Measured V_S profile names for TOK simulations.

Region	Station	V_{s30} (m/s)	Type of profile
Stations in Oklahoma	OK033*	670	Gradient
	OK048*	800	Impedance
	OK053	617	Gradient
	OK914*	790	Impedance
	OK031*	807	Impedance
	OK039*	644	Impedance
	OK034*	705	Gradient
	OK008	610	Impedance
	OK010	605	Impedance
	W36A	670	Impedance
	TUL1	694	Gradient
	OK005*	617	Gradient
	OK002	646	Impedance
Stations in Texas	AZWR	743	Impedance
	AZHL	736	Impedance
	DJLW	696	Impedance
	AZWP	800	Impedance
	135A	626	Impedance
	Z35A	667	Impedance
	PB08	776	Impedance
	ALPN	652	Impedance
	ODSA	856	Impedance
	PECS	758	Impedance
	VHRN	769	Impedance
	PB11	865	Impedance
	DAL	637	Impedance

*Profiles marked with an asterisk were extended

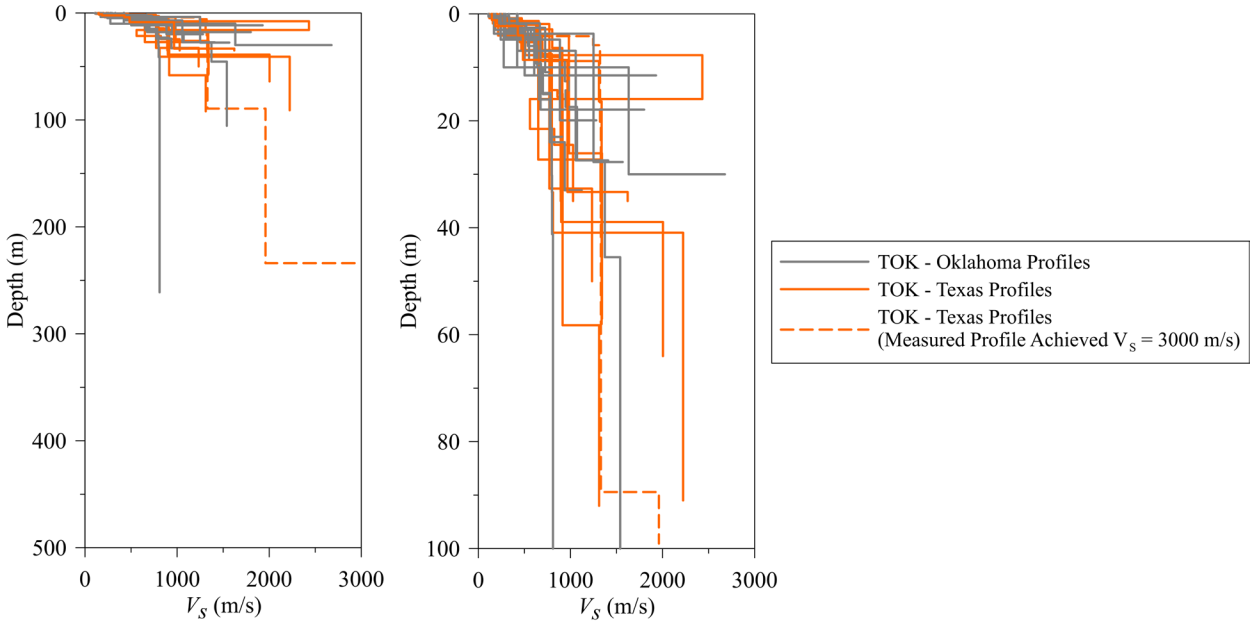

Figure 6.7 Measured Profiles for Texas and Oklahoma compiled in TOK profiles.

6.3.3.2 Extension Methodology

As shown in Figure 6.7, many of the measured profiles do not reach the reference condition of V_S = 3000 m/s. In order to employ these profiles for the development of F_{760} models, the measured profiles need to be extended to reach the reference condition of V_S = 3000 m/s. The extension methodology implemented herein is consistent with the approach adopted in Harmon et al. (2019a) as given by the following equation:

$$log(V_S) = n_v log(z) + C \quad (6.4)$$

where V_S is shear wave velocity, n_v = 0.293 as proposed in Harmon (2017), z is depth, and C is a constant used to adjust the extended profile to intersect the measured profile where it terminates.

The outcome of this approach results in a profile that follows a continuous power-law function, which would be difficult to implement in constant V_S layers for site response analysis applications. As such, the profiles are discretized into 10-m intervals. Figure 6.8 shows the Oklahoma profiles from the TOK simulations and their corresponding extensions. The Texas profiles used in the TOK simulations were not extended due to: a) difficulties associated with V_S reversals and high variability in layer thicknesses, and b) the reference condition being met, making extension unnecessary. Consequently, the Texas profiles were underlain directly by a hard-rock reference condition of V_S = 3000 m/s. The profiles used for the TOK branch analyses are shown in Figure 6.9, including their classification as impedance or gradient profiles based on the same approach described in section 6.3.2.

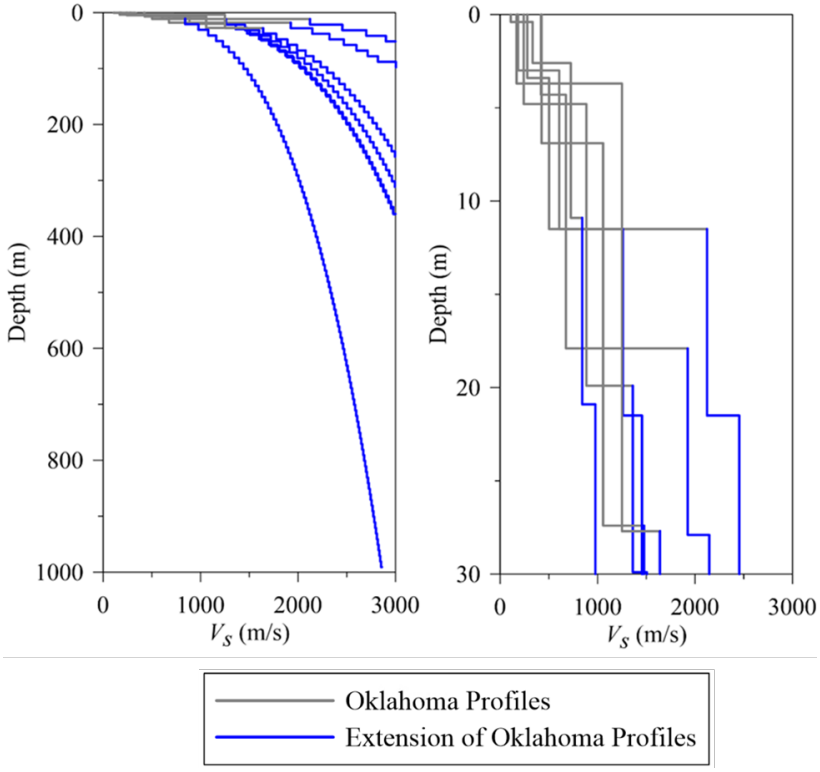

Figure 6.8 Extension of Oklahoma profiles from TOK simulations

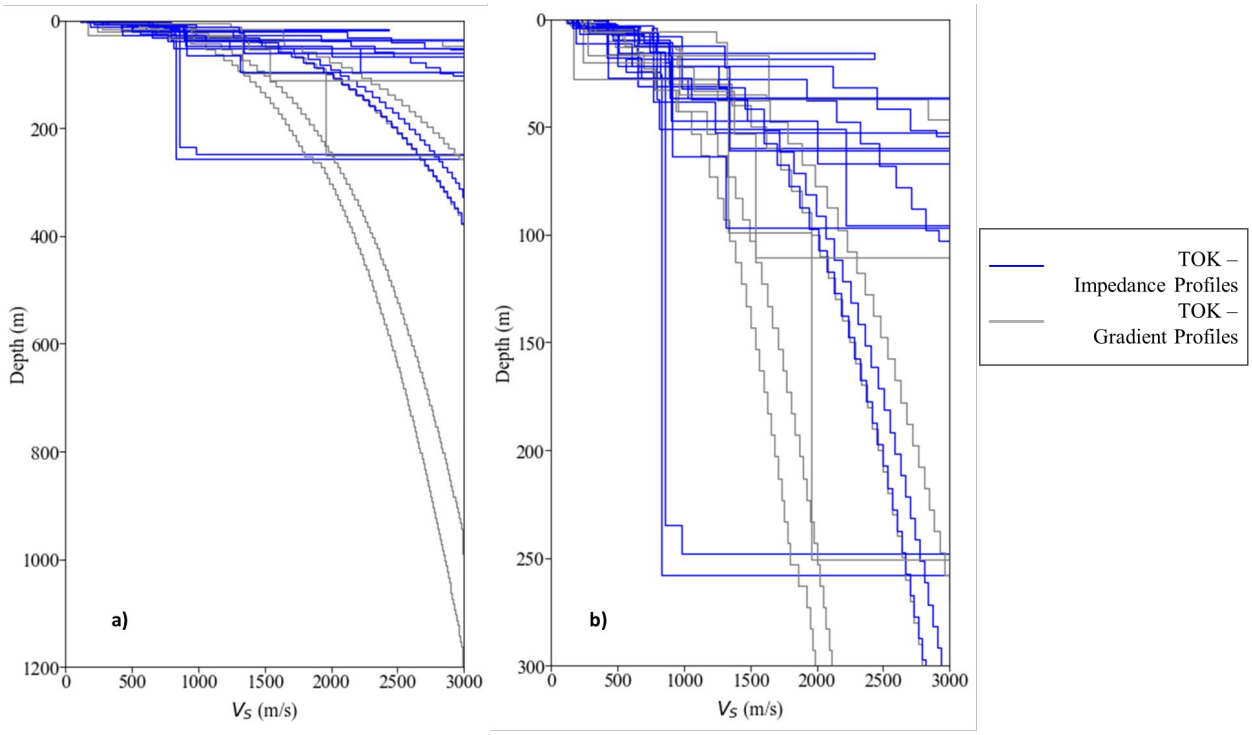

Figure 6.9 Profiles used for TOK Branch for different depths: a) Profile depth up to 1200 m, and b) detailed view of the top 300 m.

6.3.4 Nonlinear behavior of soil and rock

For both the Ilhan (2020) and TOK profiles, the Darendeli (2001) model was selected to construct MRD curves. The Darendeli (2001) model is conditioned on effective stress and various soil index properties. Ilhan (2020) uses the soil index properties proposed in Harmon et al. (2019a) as given in the Table 6.4, except for the soil shear strength which was updated and will be further discussed in the following section. Moreover, the Ilhan (2020) branch undergoes randomization of the MRD curves based Darendeli (2001) (Section 6.3.6), and after the randomization, the curves are subjected to the fitting routine of the GQ/H model (Groholski et al., 2016). The TOK branch uses the geology-based approach to select the soil material properties (Table 6.5) proposed in Harmon et al. (2019a), but the MRD curves are not randomized.

Table 6.4 Geology-based soil properties associated with Ilhan (2020) representative soil V_S profile

Material	PI (%)	Unit Weight (kN/m^3)	OCR	Friction Angle (Degrees)	Associated Characteristic V_S Profiles		
General	15	19	1.5	25	Scaled Global	V_{S30}-Binned	Judgement Soft
Weathered Rock Zone	5	21	3	40	Weathered Rock Zone		
Young Glaciated	15	18.9	1.3	30	YGd-YGt-YGo + RS + YGM		
Old Glaciated	20	18.6	3	30	RRm + OG		
Young Nonglaciated	20	18.5	1.3	30	Yna-YNl-Yns+ON	YNm	
Old Nonglaciated	30	19	2	30	Yna-YNl-Yns+ON		
Residual Soil from Sedimentary Rock	24	19.4	3	25	RRs		
Residual Soil from Metamorphic Rock	10	19	3	25	RRm+OG		
Residual Soil	30	19.3	3	25	YGd-YGt-YGo + RS + YGm		

Table 6.5 Geology-based soil properties associated with TOK measured V_S profiles

Material	PI (%)	Unit Weight (kN/m^3)	OCR	Friction Angle (Degrees)	Associated Characteristic V_S Profiles		
Young Nonglaciated	20	18.5	1.3	30	AZWR, DJLW, Z35A	All Oklahoma Stations	
Residual Soil from Sedimentary Rock	24	19.4	3	25	ALPN, VHRN		
Residual Soil from Metamorphic Rock	10	19	3	25	AZHL, AZWP, 135A, DAL		
Residual Soil	30	19.3	3	25	PB08, PB11, ODSA, PECS		

6.3.5 Soil Shear Strength

G/G_{max} along with V_S and soil density (ρ) can be used to determine the stress-strain response of a given soil material. The implied shear stress at any level of shear strain can be estimated as:

$$\tau_{implied} = \rho {V_S}^2 * (G/G_{max}) * \gamma \quad (6.5)$$

where $\tau_{implied}$ is the implied shear stress, ρ is the soil mass density, γ is shear strain, and G/G_{max} is the modulus reduction at shear strain level γ. The use of this equation might result in unrealistic values of shear strength when unreasonably high or low V_S is encountered. Moreover, if the implied shear strength after undergoing randomization is significantly different than the target shear strength for the soil material, the V_S and the nonlinear dynamic curves become incompatible (Harmon et al., 2019a), and large differences between the implied shear strength and the target shear strength might cause the GQ/H model to be unable to fit the reference dynamic curve. To avoid this issue, the randomized V_S is used to define the soil shear strength as:

$$\tau_{target,implied} = c_{v_s} + \sigma'_v * tan(\phi') \quad (6.6)$$

where c_{V_s} is the V_S-based cohesion. However, the c_{V_s} component might lead to unreasonably high strength values at shallow depths (< 10-20 m). Thus, the soil shear strength used as input to the GQ/H model ($s_{u,proposed}$) is estimated as the combination of the Agaiby and Mayne (2015) s_u - V_S

relationship and the implied shear strength formulation shown in Eq. 6.6. Considering the applicability range of Agaiby and Mayne (2015), the proposed soil shear strength model is as follows:

$$S_{u,proposed}\,(z) = \begin{cases} \max\left[s_{u,mob}(z), s_{u,V_s}(z)\right] \; for\; z \le 30\; m,\; V_s \le 300\frac{m}{s} \\ c_{V_s} + \sigma'_v \cdot \tan\left(\phi'\right) \text{ for all cases where the condition above is not satisfied} \end{cases} \quad (6.7)$$

Where $s_{u,V_s}(z)$ represent the undrained shear strength for clay materials proposed in Agaiby and Mayne (2015), presented in Eq. 6.8, and $s_{u,mob}$ is defined as the mobilized undrained shear strength as proposed by Terzaghi et al. (1996). The shear strength model previously discussed was adopted for both branches, Ilhan (2020) and TOK.

$$s_{u,V_s} = \begin{cases} 0.152 \cdot V_s^{1.142}\; for\; 1 < OCR < 2.5 \\ 0.0672 \cdot V_s^{1.33}\; for\; OCR > 2.5 \end{cases} \quad (6.8)$$

6.3.6 Randomization of modulus reduction and damping curves

Modulus reduction and damping (MRD) curves as provided by the Darendeli (2001) model are uncertain because they are model fits to data from a diverse array of soils, and index properties on which they are conditioned are not perfectly correlated to nonlinear responses. To quantify this uncertainty, Darendeli (2001) proposed strain-dependent relationships for standard deviation of MRD curves along with the median relationships. This standard deviation can be expressed as:

$$\sigma_{NG} = exp(-4.23) + \left(\frac{0.25}{exp(3.62)} - \frac{(G/G_{max} - 0.5)^2)}{exp(3.62)}\right)^{0.5} \quad (6.9)$$

$$\sigma_D = exp(-5.0) + exp(-0.25)\sqrt{D(\%)} \quad (6.10)$$

where σ_{NG} and σ_D are the strain-dependent standard deviations of the modulus reduction and damping curves, respectively, which are assumed to be distributed normally. Moreover, the methodology to perform the dynamic curve randomization was adopted from Kottke and Rathje (2008), where the Darendeli (2001) relationships are used and is given by:

$$\frac{G}{G_{max}(\gamma)} = \left[\frac{G}{G_{max}(\gamma)}\right]_{mean} + \varepsilon_1 * \sigma_{NG} \quad (6.11)$$

$$D(\gamma) = [D(\gamma)]_{mean} + \rho * \sigma_D * \varepsilon_1 + \sigma_D * \quad (6.12)$$

where ε_1 and ε_2 are N(0,1), $[G/G_{max}(\gamma)]_{mean}$ are mean modulus reduction curves, $[D(\gamma)]_{mean}$ are the mean damping curves, and ρ is the intercorrelation between modulus reduction and damping curve. The ρ value is proposed as -0.5 (Kottke and Rathje, 2018) in order to capture the negative correlation between modulus reduction and damping, which means that a higher G/G_{max} curve would lead to a lower damping curve. Harmon et al. (2019a) further developed the procedure described herein, which is implemented in DEEPSOIL V7.0 (Hashash et al., 2017).

The Ilhan (2020) branch adopts three baseline MRD curves for each layer in each generic profile. The three baseline curves consist of:

a. "High" realization represents a systematically higher G/G_{max} with respect to the mean curve generated by a positive ε.
b. "Low" realization represents a systematically lower G/G_{max} with respect to the mean curve generated by a negative ε.
c. "Mean" realization represents the mean G/G_{max} curve.

In this work, ρ = -1 is adopted to ensure a perfectly negative correlation between the baseline modulus reduction curves and damping curves. Randomization was performed about the three baseline curves. In regard to the random variable ε, the following constraints are applied:

- All ε values are bounded by 1.5σ
- G/G_{max} curves are bounded between 0 and 1.
- Damping curves should always have values greater than 0.0%

6.4 Small strain Damping and High Frequency Spectral Decay Parameter in Site Profiles

Considering that soil dissipates energy at strain levels as low as 10^{-4} % under cyclic shearing (Lanzo and Vucetic, 1999), a series of laboratory-based geotechnical models have been developed to capture small-strain damping (D_{min}) in site response analysis. Different models have been developed such as Darendeli (2001) where a series of laboratory tests, more specifically, a combination of resonant column and torsional shear equipment (RCTS), were performed to measure D_{min} and then develop a model to relate it to index parameters for soils. However, the Darendeli (2001) model only captures the hysteretic behavior of soils, and thus additional considerations must be made for the influences on strong ground motion of wave scattering effects. The κ parameter, which is the high frequency spectral decay parameter, is introduced to scale D_{min} to account for these other mechanisms of energy dissipation.

Stochastic point source simulations (Boore, 1983, 2003) produce ground motion time series at the level of the reference condition based on path and source models, which is then convolved with a site amplification function and a model of the decay of acceleration at high frequencies of the Fourier Amplitude Spectrum (FAS), which is described by the κ parameter. This decay is modeled as:

$$A(f) = A_0 * e^{-\pi\kappa f} \quad (6.13)$$

where κ is estimated by measuring the slope of the log-linear FAS of strong motion records (Anderson and Hough, 1984). Furthermore, distance-dependency was introduced in the κ parameter by Hough and Anderson (1988) by separating the attenuation that occurs at the site from the attenuation associated with the travel path. The κ parameter can then be expressed as:

$$\kappa(r) = \kappa_0 + \kappa_1 * R \quad (6.14)$$

Where κ_0 represents the attenuation due to surficial material, and $\kappa_1 * R$ represents the attenuation due to regional attenuation characteristics related to the effective quality factor, Q. The parameter κ_0 can then be estimated as proposed by Hough and Anderson (1988):

$$\kappa_0 = \int \frac{1}{Q(z)*V_s(z)} dz \quad (6.15)$$

The Q(z) parameter is commonly related to D_{min} as $Q = 1/(2 \cdot \mathrm{D}_{\min})$. By separating the κ_0 contributions from the source to the base of the rock ($\kappa_{0,rock}$) and the soil material located on top of the rock ($\Delta\kappa_0$), one can re-arrange (e.q. 6.15) as:

$$\kappa_0 = \kappa_{0,rock} + \Delta\kappa_0 \quad (6.16)$$

$$\kappa_0 = \kappa_{0,rock} + \int \frac{2*D_{min}(z)}{V_s(z)} dz \quad (6.17)$$

where $\kappa_{0,rock}$ is taken as 0.006 s (Hashash et al., 2014). For the present study, D_{min} for each layer is estimated using the Campbell (2009) Q-V_s Model-1 given by:

$$Q = 7.17 + 0.0276 * V_s \quad (6.18)$$

where V_s is in units of m/s. To produce κ-informed site response analyses, the D_{min} values estimated from the Campbell (2009) Q-Vs model were scaled in order to approximate target κ_0 values. The target κ_0 values are as follows:

i) For the Ilhan (2020) branch, the target κ_0 values are obtained from the V_{S30}-based model from Xu et al. (2020), where κ_0 is estimated using V_{s30} and a) $40\,m \leq Z_{2.5} \leq 179\,m$ and b) $179\,m \leq Z_{2.5} \leq 1067\,m$ where $Z_{2.5}$ is depth to $V_s \geq 2500$ m/s

ii) For the TOK branch, the target κ_0 values range between 0.01 s as a lower bound and 0.05 s as an upper bound.

For a number of profiles in both branches of the parametric study tree, there are noticeable discrepancies between the target κ_0 and the current site κ_0 values based on the Campbell (2009) Q-V_s model. These discrepancies can be addressed by adjusting the D_{min} based on the following equation:

$$\kappa_{0,adjusted} = \kappa_{0,rock} + \int \frac{2*[D_{min}(z)\psi(z)]}{V_s(z)} dz \quad (6.19)$$

where $\psi(z)$ is the depth-dependent D_{min} scaling parameter to adjust the κ_0 to a given target value, which is originally proposed in Afshari and Stewart (2015) and can be related to changes in D_{min} as:

$$\psi(z) = \Delta D_{min,0} * (\frac{V_{s,i}}{b})^c \quad (6.20)$$

Where b and c are coefficients established as 200 m/s and 0.3 by Afshari and Stewart (2015), respectively. It should be noted that this value is applied as a multiplicative factor instead of an

additive terms, as originally proposed in Afshari and Stewart (2015). In the present study, b and c are used as proposed by Afshari and Stewart (2015) but the $\Delta D_{min,0}$ is changed for each profile until the target κ_0 is achieved. However, updating D_{min} might lead to unreasonable values of D_{min} for some profiles due to:

- *The small value of* $\kappa_{0,rock} = 0.006\ s$ For shallow sites, D_{min} needs to be unreasonably high to capture target values adopted in the present study.
- *Incompatibility in data used for Xu et al.* (2020): Most of the generic profiles used in the Ilhan (2020) branch have incompatible combinations of V_{S30} and $Z_{2.5}$ as compared to the profiles used in Xu et al. (2020).

Given these issues, an upper limit of D_{min} = 6% is applied to constrain the adjustment of κ_0 values to prevent the generation of unreasonable values of D_{min}. Figure 6.10 and Figure 6.11 show the original and adjusted κ_0 values for both Ilhan (2020) and the TOK branches, in V_{S30}-κ_0 space. As shown in Figure 6.11, most of the TOK profiles using D_{min} from the Campbell (2009) Q-V_s model do not have κ_0 values that fall within the target κ_0 range of 0.01 to 0.05 s. However, after adjusting κ_0 by scaling D_{min}, nearly all of the TOK profiles fall within the target κ_0 range. Figure 6.12 plots histograms of κ_0 for profiles classified as gradient and impedance as defined in Sections 6.3.2-6.3.3 (V_{S30} ranges of 700-800 and 600-900 m/s respectively, for Ilhan and TOK). Values of κ_0 vary from 0.01 to 0.03 sec for both impedance and gradient profiles. For the Ilhan (2020) gradient profiles, there is distinct group of profiles that fall in the bin with κ_0 values 0.0275 to 0.0325 s. This group consists of profiles with a large depth to reference condition, specifically, profiles with depth to reference condition between 200 m and 1200 m. When comparing between gradient and impedance profiles for both branches, there are distinct clusters of profiles at κ_0 ~0.01 s for the impedance profiles, which may suggest that impedance profiles generally are shallower. On the other hand, for gradient profiles, κ_0 values are generally evenly distributed between 0.01 s and 0.03 s.

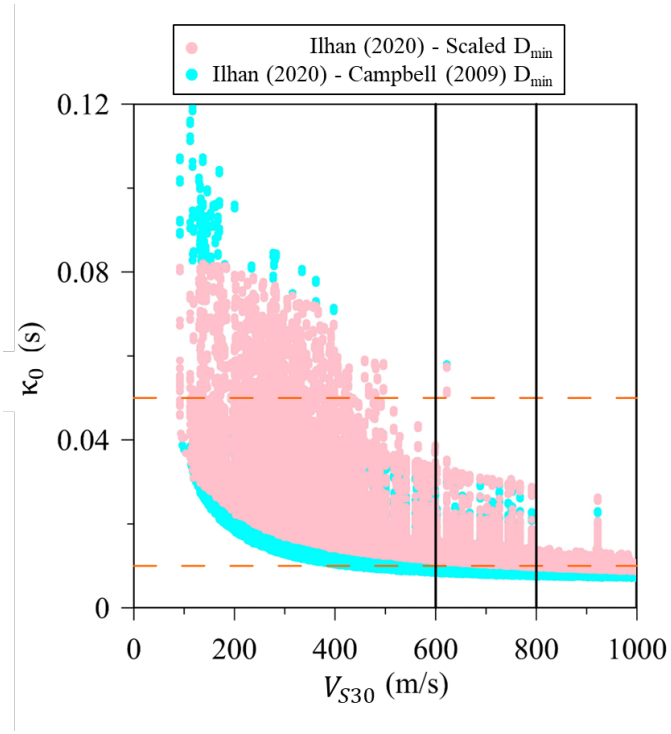

Figure 6.10 Distribution of Ilhan (2020) Profiles for original D_{min} and scaled D_{min} simulations

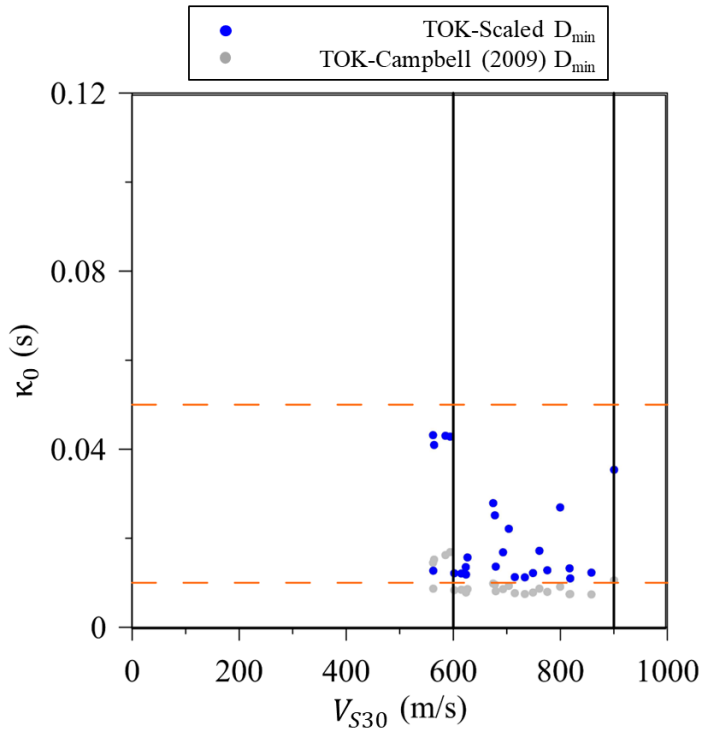

Figure 6.11 Distribution of TOK Profiles for original D_{min} and scaled D_{min} simulations

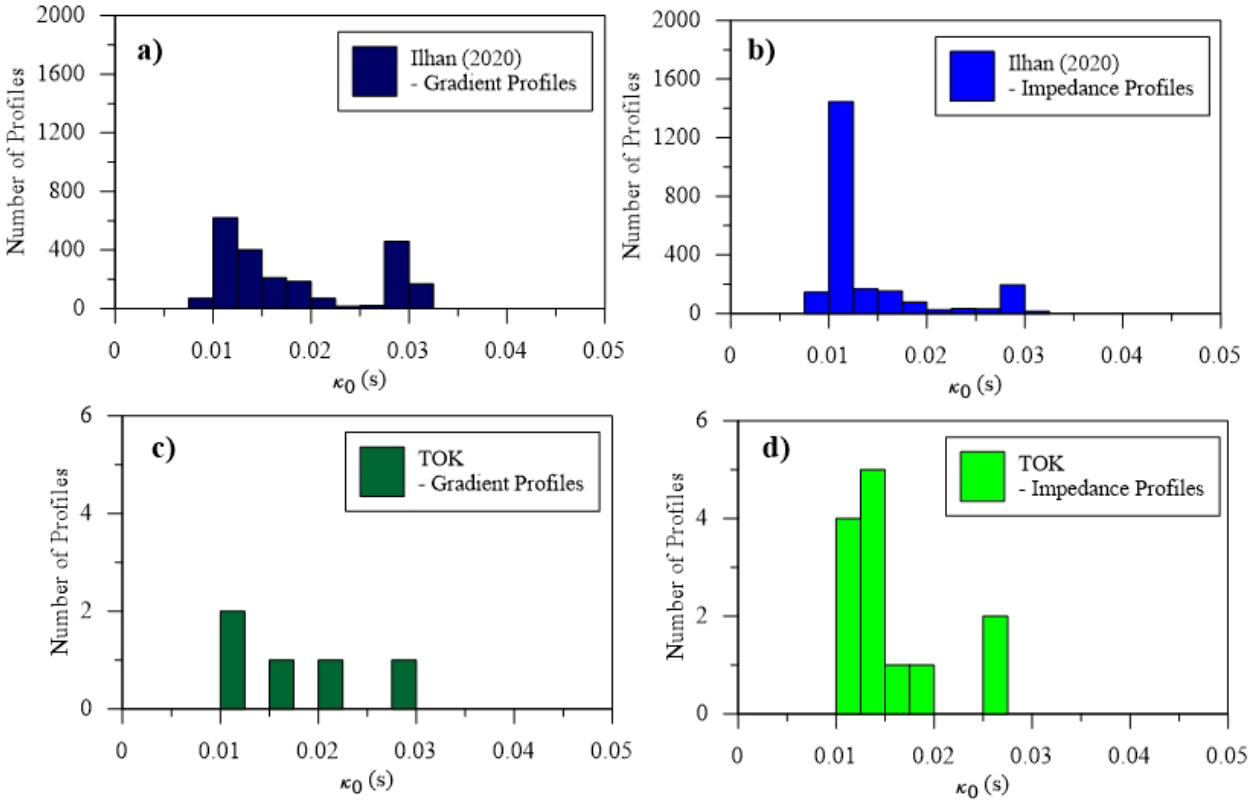

Figure 6.12 Histograms of κ_0 for scaled D_{min} simulations for a) Ilhan (2020) gradient, b) Ilhan (2020) impedance, c) TOK gradient, and d) TOK impedance profiles.

6.5 Simulated Site Response Results

6.5.1 Study Workflow

The parametric study tree used for this study is composed of 148,050 generic site profiles and 26 measured profiles corresponding to the Ilhan (2020) and TOK branches, respectively, along with 247 rock outcrop motions distributed over the site profiles. The analyses were conducted on two platforms, the Ilhan (2020) branch analyses were conducted using the High-Performance Computing (HPC) resources in Stampede2 (Stanzione et al., 2017) of the Texas Advanced Computing Center (TACC), and the TOK branch analyses were performed using Dell PowerEdge workstations, which are part of PI Hashash's research group servers.

The workflow for this study is composed of four main stages:

1. Generate DEEPSOIL V7.0 inputs
2. Run site response analyses
3. Construct database of site response simulation results
4. Develop simulation-based site amplification model

6.5.2 Generation of Input Profile

The parametric study tree consists of two main branches as described in Section 6.3: Ilhan (2020) and TOK. The Ilhan (2020) branch's DEEPSOIL V7.0 (Hashash et al., 2017) input profiles are generated using a Python (Rossum, 2007) code originally developed for previous CENA studies, specifically Harmon et al., (2019a) but modified to account for the different improvements adopted for the current study. This python code is designed to perform i) V_S and MRD curve randomizations, ii) GQ/H curve fitting procedure for the MRD curves, iii) truncation of site profiles based on Z_{soil} bins, and iv) output each input file as a .txt file. The whole parametric study is divided into 14 batches and each batch is ran using 1 SKX node with 94 cores in Stampede2. Each batch consists of 11,340 profiles and 630 near surface rock sites.

The TOK profiles were manually developed using the DEEPSOIL V7.0 (Hashash et al., 2017) Graphical User Interface (GUI). The TOK branch consists of 26 profiles, and each profile was developed individually and saved as a .dpz file.

6.5.3 Site Response Analyses

The simulations were conducted using DEEPSOIL V7.0 (Hashash et al., 2017). The analyses for the two branches of the parametric study tree were conducted differently. For the Ilhan (2020) branch, the DEEPSOIL V7.0 (Hashash et al., 2017) computational core was compiled for a Linux Operation System to be used in Stampede2 (Stanzione et al., 2017) SKX nodes, and the analyses were divided also in a similar fashion to the generation of the input files, more specifically:

- The total number of simulations (3,656,835 NL, EL, and LE) is divided into 14 batches.
- Each batch consists of 280,098 NL, EL, and LE analyses except for near-surface rock simulations. Each batch is then divided into 18 subsets consisting of 15,561 analyses
- Each subset composed of 15,561 analyses is submitted as a separate job using 1 SKX node with 80 cores in Stampede2.

The TOK simulations were conducted in a research server at University of Illinois Urbana-Champaign because of the considerably fewer number of simulations that needed to be conducted for this branch. The server is a Dell PowerEdge with an Intel Xeon E5-2630 v3, 16 physical cores and 32 logical cores. In this case, each of the profiles were analyzed using NL, EL, and LE methods, each of which was performed for 247 motions. All of the analysis were run using the DEEPSOIL V7.0 (Hashash et al., 2017) Graphical User Interface (GUI).

6.5.4 Database for simulation results

Site response analysis were archived in a database format, specifically an SQLite3 database that contains the following information:

- Time series and spectral response information at the surface (or first soil layer) for NL, EL, and LE analyses:
    - Time series: Arias Intensity (AI), acceleration, velocity, displacement time series at the top of the first layer, and shear stress, and shear strain time series at the middle point of the first layer.

    - Spectral response: 5% damped response spectra computed using the frequency domain approach as described in Kramer (1996) at 435 periods from 0.001 s to 10.0 s, and FAS at frequencies equally spaced from Nyquist frequency of rock outcrop motion to 0 Hz (not included) at N/2-1 points where N is the first power of 2 that contains the number of points in the rock outcrop motion.
- Profiles of maximum responses as a function of depth in terms of: i) acceleration (PGA), ii) velocity (PGV), iii) peak AI, iv) minimum and maximum displacement at the top of each later, and vi) effective stress, vii) maximum shear strain, and viii) maximum shear stress at the middle point of each layer.

For each of the branches, two large databases of all site response analyses are generated to be used for further research and development of site amplification models. The first database consists of NoSQL databases using MongoDB (Banker, 2011) for each branch, consistent with the approach used in Hashash et al. (2018) and the second database, referred to as flatfiles, include all of the profiles' relevant information (e.g. $V_{S,30}$, T_{nat}, $\Delta\kappa$, etc) along with information regarding the input motion and the results of each simulation. These flatfiles are used for the development of site amplification models and other related applications.

6.5.5 Characterization of Amplification Data

The present study aims to produce new simulation result for F_{760} models using a large-scale parametric study composed of two branches (Section 6.3): the Ilhan (2020) branch and the TOK branch. The TOK branch contains 26 profiles with V_{S30} values between ~ 600 to 900 m/s. For the Ilhan (2020) branch, a subset of the 36780 profiles for which results are available in the Ilhan (2020) dataset are used to estimate F_{760} models using simulation results for V_{S30} values between ~ 700 to 800 m/s. Here we present amplification data for both branches as a function of V_{S30} for different periods, focusing on results near 760 m/s. Amplification is calculated as:

$$ln(Amp[T]) = ln(\frac{S_{a,surface}[T]}{S_{a,input}[T]}) \quad (6.21)$$

where $S_{a,surface}[T]$ is the spectral acceleration at the surface for oscillator period T, and $S_{a,input}[T]$ is the spectral acceleration of the input motion for that same period. Figure 6.13 and Figure 6.14 show linear site amplification for different periods from simulations with D_{min} from the Campbell Q-V_S Model (Eq. 6.17) and with scaled-D_{min} as a function of V_{S30} for a series of periods for both branches. The subset of the Ilhan (2020) simulations being used to develop the F_{760} models is highlighted with dashed lines. For this range of V_{S30}, linear amplification for both branches show consistent results, especially for the simulations that use the original D_{min} values. For short periods (T < 0.05 s) the TOK simulations with D_{min} estimated directly from the Campbell (2009) Q-V_s model estimate higher amplification than the Ilhan (2020) simulations. However, the TOK simulations with scaled D_{min} to capture the target κ_0 show higher attenuation compared to the Ilhan (2020) simulations. For periods higher than T = 0.05 s, comparable amplification results were estimated for both TOK and Ilhan (2020) branches. Moreover, no significant differences were observed between simulations with scaled D_{min} to capture the target κ_0 and the simulations with original D_{min} values, specifically for periods T > 0.05 s, due the lack of influence of κ_0 on long periods.

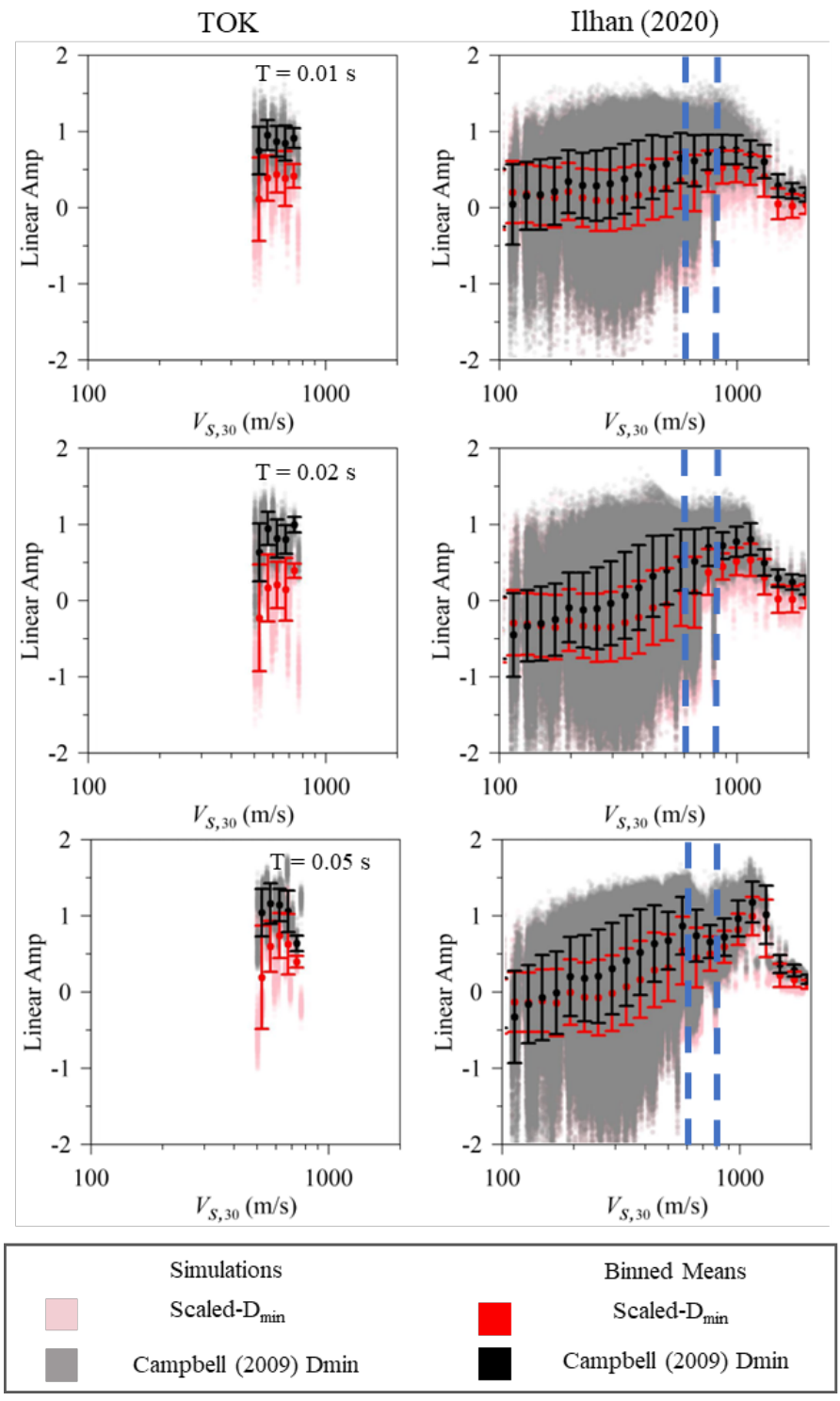

Figure 6.13 Linear amplification for Ilhan (2020) and TOK branches as a function of V_{S30} for periods T = 0.01 s, 0.02 s, and 0.05 s.

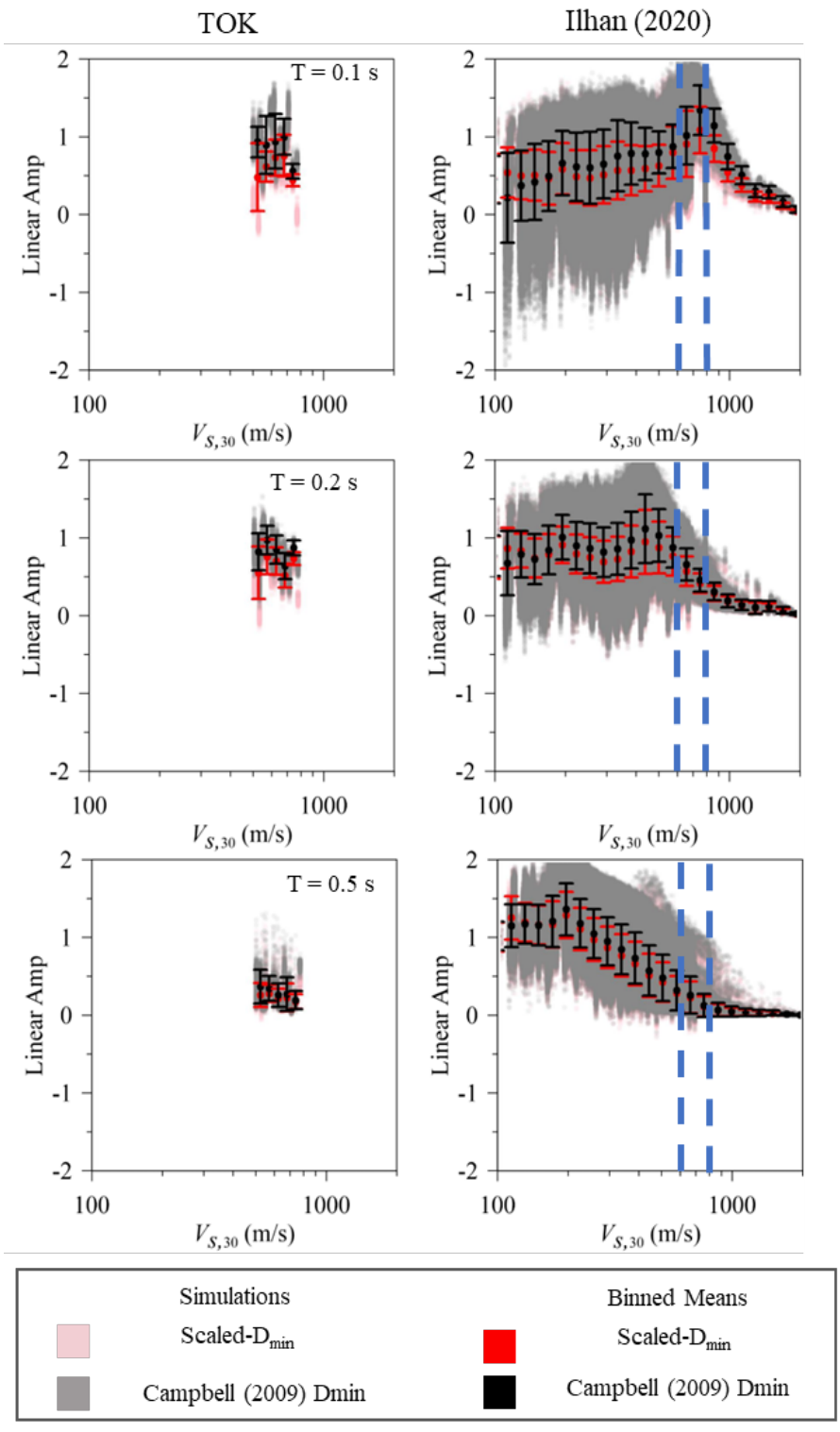

Figure 6.14 Linear amplification for Ilhan (2020) and TOK branches as a function of V_{S30} for periods T = 0.1 s, 0.2 s, and 0.5 s.

The results for equivalent linear analysis, as shown in Figure 6.15 and Figure 6.16 exhibit a slightly different behavior due to the attenuating effects of nonlinearity. For short periods, specifically T <

0.05 s, the simulations with the original D_{min} values show higher amplification for the TOK simulations compared to the Ilhan (2020) simulations, and an increase in amplification with increasing V_{S30} in the range relevant to F_{760} models, which is consistent with sites with higher V_{S30} showing lower levels of nonlinearity. Similarly, for the simulations with the scaled D_{min} values to capture a target κ_0, the same trend is observed but overall, both branches show lower amplification due to the effects of κ_0. However, for longer periods (T > 0.05 s), the trend is the opposite. With increasing V_{S30}, there is a decrease in amplification. This is observed for both branches, and for both sets of simulations, specifically the simulations with original D_{min} values and the simulations with scaled D_{min} to capture target κ_0. In terms of the differences between the simulations with original D_{min} values and the simulations with scaled D_{min} to capture target κ_0, the effect of κ_0 is clearly observed at short periods (T < 0.05 s). For longer periods, the effect of κ_0 is negligible, especially for stiffer sites.

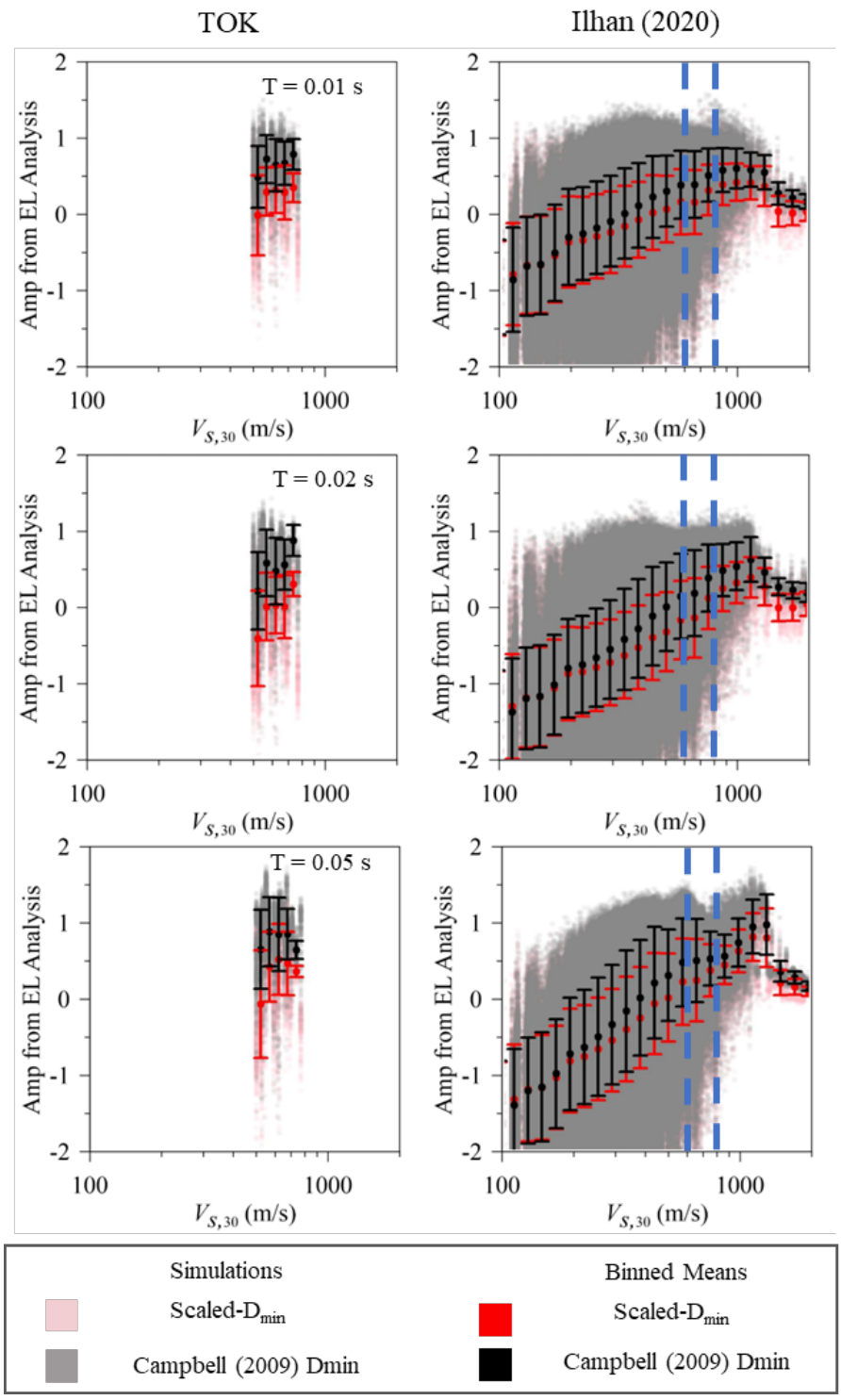

Figure 6.15 Binned mean amplification from Equivalent Linear analysis for Ilhan (2020) and TOK branches as a function of V_{S30} for periods T = 0.01 s, 0.02 s, and 0.05 s.

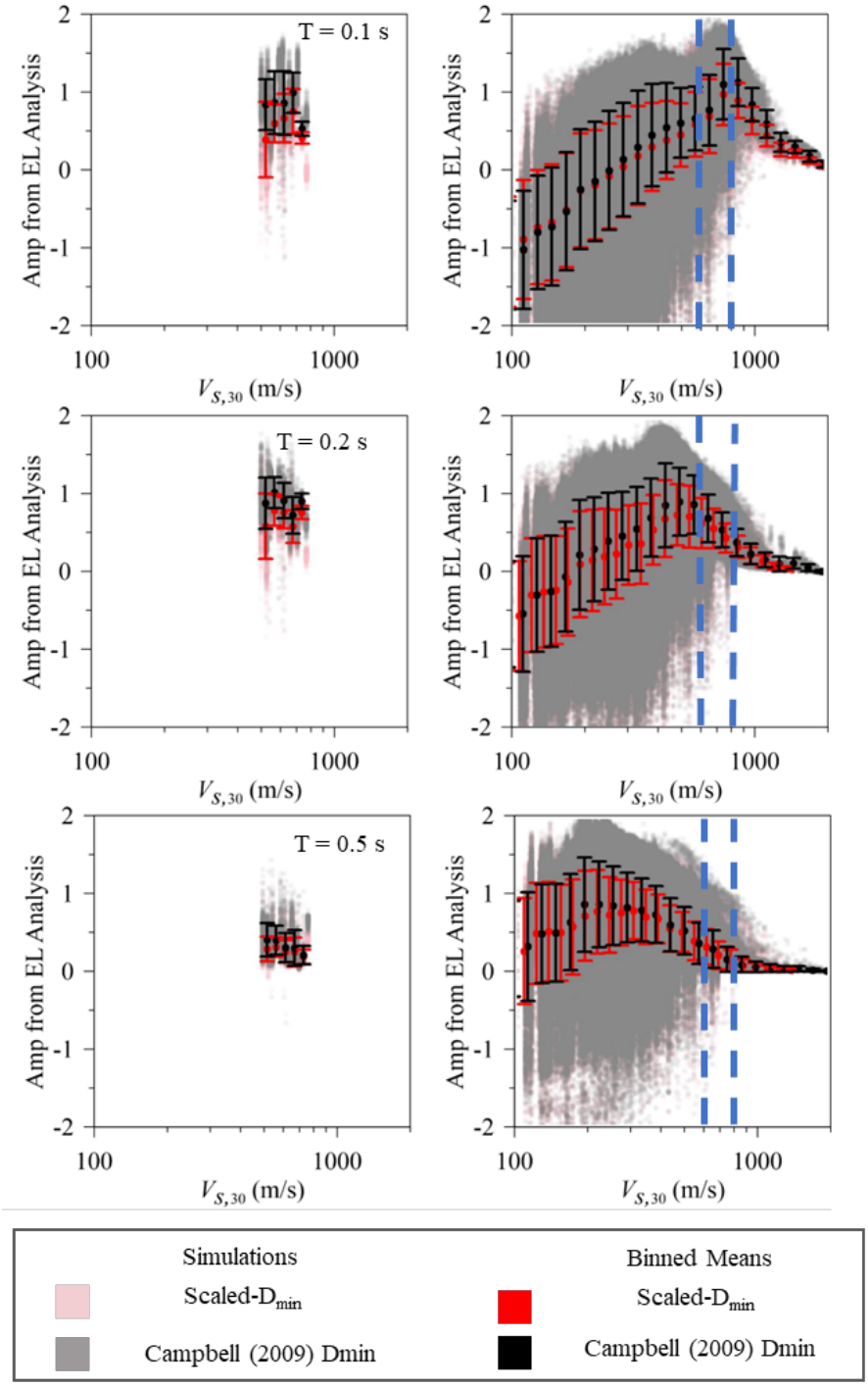

Figure 6.16 Binned mean amplification from Equivalent Linear analysis for Ilhan (2020) and TOK branches as a function of V_{S30} for periods T = 0.1 s, 0.2 s, and 0.5 s.

Lastly, Figure 6.17 and Figure 6.18 show the amplification calculated from nonlinear site response analysis as a function of V_{S30}. As expected, the amplification results for nonlinear analysis and equivalent linear analysis show consistent behavior, nonetheless, some differences were observed. Overall, amplification factors from nonlinear analysis show systematically lower values,

for low V_{S30} sites. This might be related to stronger effects of nonlinearity observed in nonlinear analysis. More specifically, for short periods, specifically T < 0.05 s, the simulations with the original D_{min} values show slightly higher amplification for the TOK simulations compared to the Ilhan (2020) simulations, and an increase in amplification with increasing V_{S30} in the range relevant to F_{760} models, which is consistent with sites with higher V_{S30} showing lower levels of nonlinearity. For longer periods (T > 0.05 s), there is a decrease in amplification with increasing V_{S30}. This is observed for both branches, and for both sets of simulations. In terms of the differences between the simulations with original D_{min} values and the simulations with scaled D_{min} to capture target $\kappa_{0,}$ the effect of κ_0 is clearly observed at short periods (T < 0.05 s). For longer periods, the effect of κ_0 is negligible, especially for stiffer sites.

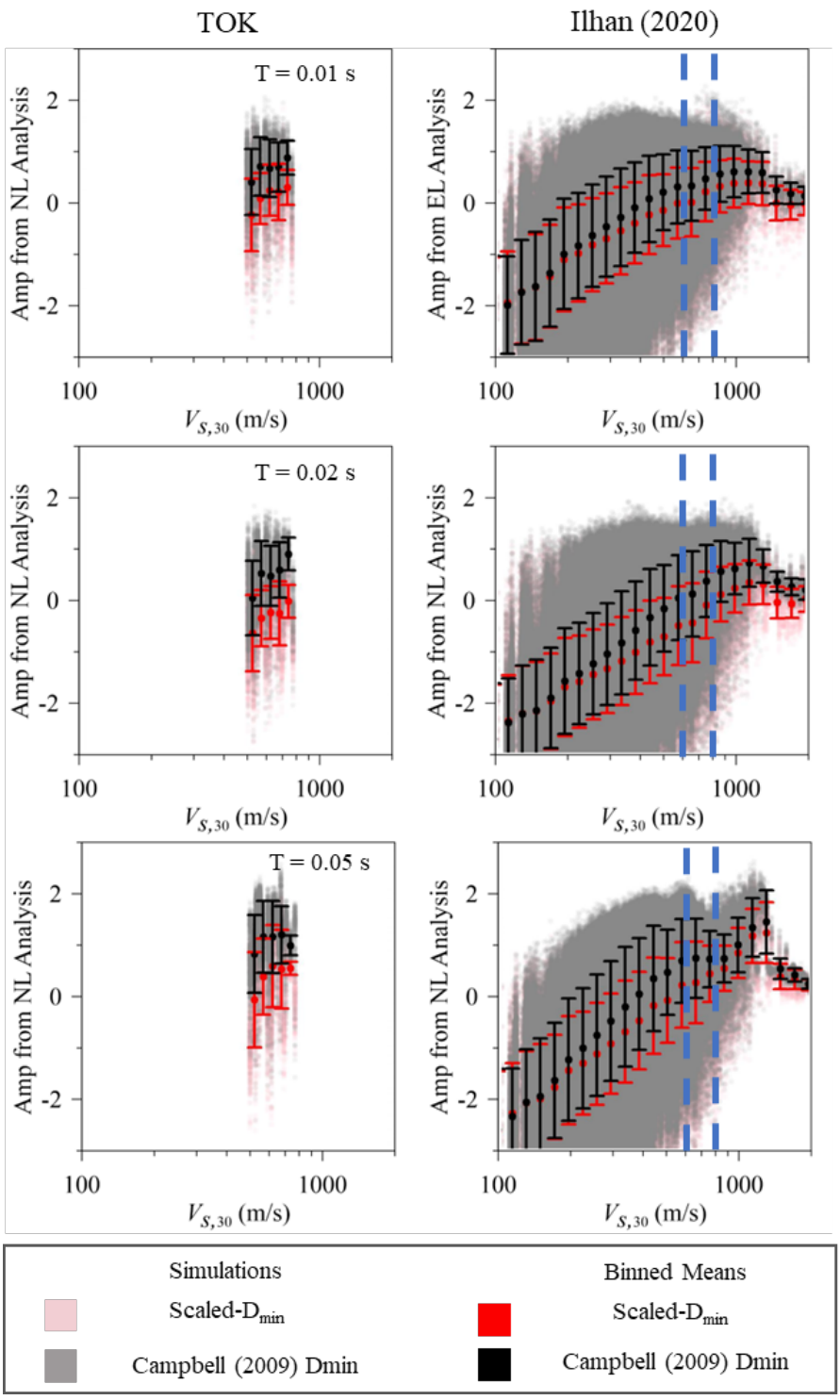

Figure 6.17 Binned mean amplification from Nonlinear analysis for Ilhan (2020) and TOK branches as a function of V_{S30} for periods T = 0.01 s, 0.02 s, and 0.05 s.

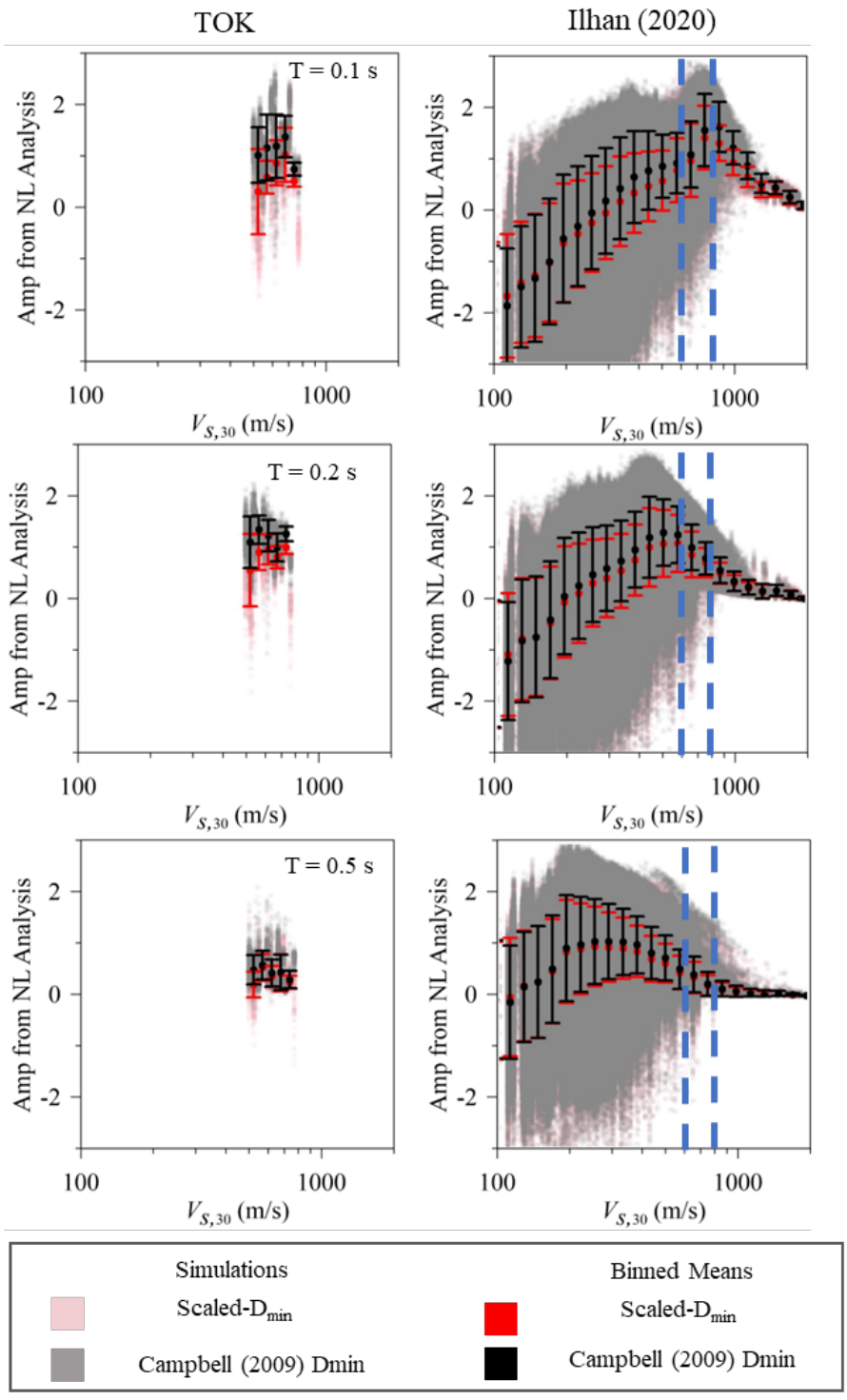

Figure 6.18 Binned mean amplification from Nonlinear analysis for Ilhan (2020) and TOK branches as a function of V_{S30} for periods T = 0.1 s, 0.2 s, and 0.5 s.

7 Implications for F_{760} Models

7.1 F_{760} Models

Simulation-based F_{760} models, which are the factors used to adjust the site amplification relative to V_{S30} = 760 m/s from the CENA reference of V_S = 3000 m/s, were developed by estimating the amplification using Eq. 6.21 from profiles where V_{S30} values are approximately equal to 760 m/s. Because of the complications associated with identifying profiles with V_{S30} = 760 m/s (actual range of 700-800 m/s and 600-900 m/s for Ilhan and TOK branches; Chapter 6), the F_{760} models for each branch are calculated as the mean of the period-dependent amplification of the batch of simulations along with the associated uncertainty.

A series of F_{760} models for each branch (i.e., Ilhan (2020) and TOK) were produced considering i) three types of analyses (Linear elastic, equivalent linear, and nonlinear analysis), and ii) a series of D_{min} formulations. Initially, two D_{min} formulations were used: a) D_{min} from Campbell (2009) Q-V_S Model-1, referred to as the original D_{min} throughout, and b) the scaled version of D_{min} from Campbell (2009) to capture target κ_0 from Xu et al. (2020). The later set was then subdivided into 4 sets whereby each set would only contain the simulations that meet specific κ_0 ranges. These κ_0 ranges are: κ_0 = 0.005 to 0.015 s (labeled 0.01 s), κ_0 = 0.015 to 0.025 s (labeled 0.02 s), κ_0 = 0.025 to 0.035 s (labeled 0.03 s), and all κ_0. This leads to the following numbers of F_{760}, i) 2 branches (Ilhan 2020 and TOK), ii) 3 types of analysis (LE, EL, and NL), and iii) 5 sets of simulations with different D_{min} formulations (original D_{min}, scaled D_{min} for 4 different κ_0 ranges, resulting in total of 30 F_{760} models.

Table 7.1. and Table 7.2. show the nomenclature used for each F760 factor, as well as a description of what set of simulations was used to develop each F_{760} factor, for the Ilhan (2020) branch and the TOK branch, respectively.

Table 7.1 Nomenclature for F_{760} models from Ilhan (2020)

F_{760} Nomenclature	Branch	D_{min} Formulation	Type of Analysis
$F_{760,I20,C,LE}$	Ilhan (2020)	Original Campbell (2009) D_{min}	Linear Elastic
$F_{760,I20,C,EL}$	Ilhan (2020)	Original Campbell (2009) D_{min}	Equivalent Linear
$F_{760,I20,C,NL}$	Ilhan (2020)	Original Campbell (2009) D_{min}	Nonlinear
$F_{760,I20,All\text{-}\kappa0,LE}$	Ilhan (2020)	Scaled D_{min} to capture target κ_0 (All κ_0 values)	Linear Elastic
$F_{760,I20,All\text{-}\kappa0,EL}$	Ilhan (2020)	Scaled D_{min} to capture target κ_0 (All κ_0 values)	Equivalent Linear
$F_{760,I20,All\text{-}\kappa0,NL}$	Ilhan (2020)	Scaled D_{min} to capture target κ_0 (All κ_0 values)	Nonlinear
$F_{760,I20,\kappa0=0.01,LE}$	Ilhan (2020)	Scaled D_{min} to capture target κ_0 (Only κ_0 = 0.005-0.015 s)	Linear Elastic
$F_{760,I20,\kappa0=0.01,EL}$	Ilhan (2020)	Scaled D_{min} to capture target κ_0 (Only κ_0 = 0.005-0.015 s)	Equivalent Linear
$F_{760,I20,\kappa0=0.01,NL}$	Ilhan (2020)	Scaled D_{min} to capture target κ_0 (Only κ_0 = 0.005-0.015 s)	Nonlinear
$F_{760,I20,\kappa0=0.02,LE}$	Ilhan (2020)	Scaled D_{min} to capture target κ_0 (Only κ_0 = 0.015-0.025 s)	Linear Elastic
$F_{760,I20,\kappa0=0.02,EL}$	Ilhan (2020)	Scaled D_{min} to capture target κ_0 (Only κ_0 = 0.015-0.025 s)	Equivalent Linear
$F_{760,I20,\kappa0=0.02,NL}$	Ilhan (2020)	Scaled D_{min} to capture target κ_0 (Only κ_0 = 0.015-0.025 s)	Nonlinear
$F_{760,I20,\kappa0=0.03,LE}$	Ilhan (2020)	Scaled D_{min} to capture target κ_0 (Only κ_0 = 0.025-0.035 s)	Linear Elastic
$F_{760,I20,\kappa0=0.03,EL}$	Ilhan (2020)	Scaled D_{min} to capture target κ_0 (Only κ_0 = 0.025-0.035 s)	Equivalent Linear
$F_{760,I20,\kappa0=0.03,NL}$	Ilhan (2020)	Scaled D_{min} to capture target κ_0 (Only κ_0 = 0.025-0.035 s)	Nonlinear

Table 7.2 Nomenclature for F_{760} models from TOK simulations

F_{760} Factor Nomenclature	Branch	D_{min}	Type of Analysis
$F_{760,TOK,C,LE}$	TOK	Original Campbell (2009) D_{min}	Linear Elastic
$F_{760,TOK,C,EL}$	TOK	Original Campbell (2009) D_{min}	Equivalent Linear
$F_{760,TOK,C,NL}$	TOK	Original Campbell (2009) D_{min}	Nonlinear
$F_{760,TOK,All-\kappa0,LE}$	TOK	Scaled D_{min} to capture target κ_0 (All κ_0 values)	Linear Elastic
$F_{760,TOK,All-\kappa0,EL}$	TOK	Scaled D_{min} to capture target κ_0 (All κ_0 values)	Equivalent Linear
$F_{760,TOK,All-\kappa0,NL}$	TOK	Scaled D_{min} to capture target κ_0 (All κ_0 values)	Nonlinear
$F_{760,TOK,\kappa0=0.01,LE}$	TOK	Scaled D_{min} to capture target κ_0 (Only κ_0 = 0.005-0.015 s)	Linear Elastic
$F_{760,TOK,\kappa0=0.01,EL}$	TOK	Scaled D_{min} to capture target κ_0 (Only κ_0 = 0.005-0.015 s)	Equivalent Linear
$F_{760,TOK,\kappa0=0.01,NL}$	TOK	Scaled D_{min} to capture target κ_0 (Only κ_0 = 0.005-0.015 s)	Nonlinear
$F_{760,TOK,\kappa0=0.02,LE}$	TOK	Scaled D_{min} to capture target κ_0 (Only κ_0 = 0.015-0.025 s)	Linear Elastic
$F_{760,TOK,\kappa0=0.02,EL}$	TOK	Scaled D_{min} to capture target κ_0 (Only κ_0 = 0.015-0.025 s)	Equivalent Linear
$F_{760,TOK,\kappa0=0.02,NL}$	TOK	Scaled D_{min} to capture target κ_0 (Only κ_0 = 0.015-0.025 s)	Nonlinear
$F_{760,TOK,\kappa0=0.03,LE}$	TOK	Scaled D_{min} to capture target κ_0 (Only κ_0 = 0.025-0.035 s)	Linear Elastic
$F_{760,TOK,\kappa0=0.03,EL}$	TOK	Scaled D_{min} to capture target κ_0 (Only κ_0 = 0.025-0.035 s)	Equivalent Linear
$F_{760,I20,\kappa0=0.03,NL}$	TOK	Scaled D_{min} to capture target κ_0 (Only κ_0 = 0.025-0.035 s)	Nonlinear

7.2 Comparison between F_{760} calculated for LE, EL, and NL analysis

This section compares F_{760} models estimated using amplification from LE, EL and NL simulations along with their corresponding standard deviations (σ_{760} in ln units) for each branch and different D_{min} formulations. Figure 7.1 illustrates the comparison of F_{760} for Ilhan (2020) simulations with original D_{min} values from Campbell (2009). For F_{760} from LE simulations ($F_{760,I20,C,LE}$), there is a

distinct amplification peak at T 0.1 s. This peak is evident in F_{760} from EL ($F_{760,I20,C,EL}$) and NL ($F_{760,I20,C,NL}$) simulations, but is slightly shifted to the longer periods probably due to period elongation behavior in NL and EL analyses. Furthermore, $F_{760,I20,C,EL}$ and $F_{760,I20,C,NL}$ exhibit a lower level of amplification relative to $F_{760,I20,C,LE}$ for periods T < ~0.1 s as expected because of the effects of damping in NL and EL analyses as compared to LE simulations. For periods T > ~0.16 s, the differences between LE ($F_{760,I20,C,LE}$), EL ($F_{760,I20,C,EL}$), and NL ($F_{760,I20,C,NL}$) models are negligible. Uncertainties represented by σ_{760} decrease with increasing period. Figure 7.2 shows a similar comparison but in this case the LE ($F_{760,I20,\kappa0,LE}$), EL ($F_{760,I20,\kappa0,EL}$) and NL ($F_{760,I20,\kappa0,NL}$) simulations are from the Ilhan (2020) branch with scaled D_{min} to capture target κ_0. The trend that is observed is consistent with Figure 7.1 except that (a) systematically lower levels of amplification occur due to the increased D_{min} values, and (b) the trough at T ~ 0.02 sec becomes larger in Figure 7.2.

Figure 7.3 compares F_{760} for LE ($F_{760,I20,\kappa0=0.01,LE}$), EL ($F_{760,I20,\kappa0=0.01,EL}$) and NL ($F_{760,I20,\kappa0=0.01,NL}$) simulations from the Ilhan (2020) branch using scaled D_{min} to capture target $\kappa_0 \approx 0.01$ s values. Overall, the behavior is consistent with that observed in Figure 7.2, with minor differences. Among the differences, a slight amplification peak is observed for LE ($F_{760,I20,\kappa0=0.01,LE}$) at a period T ~ 0.05 s. This slight peak is also observed for EL ($F_{760,I20,\kappa0=0.01,EL}$) and NL ($F_{760,I20,\kappa0=0.01,NL}$), but the magnitude of this peak is lower, which is expected due to the effects of nonlinearity at short periods in EL and NL analyses. Overall, the behavior is consistent in Figure 7.2 and Figure 7.3, which suggests that the subset of simulations with $F_{760,I20,\kappa0=0.01,EL}$ is representative of the majority of the profiles.

Figure 7.4 shows a similar comparison but considering only the simulations with target $\kappa_0 \approx 0.02$ s. The behavior of F_{760} models for this subset differ from the other in two main ways: (1) the amplification peak shifts from 0.1 s to 0.4 s for LE ($F_{760,I20,\kappa0=0.02,LE}$), EL ($F_{760,I20,\kappa0=0.02,EL}$) and NL ($F_{760,I20,\kappa0=0.02,NL}$), and (2) lower amplification is observed at periods T < 0.1 s. Both differences are caused by different attributes in the profiles associated with the different κ_0 values. As suggested by Eq. 6.20, deeper profiles produce higher κ_0, which will also produce longer resonant periods and less short period amplification. Both of these features are observed in Figure 7.4. In terms of comparison between analyses, the F_{760} from EL ($F_{760,I20,\kappa0=0.02,EL}$) and NL ($F_{760,I20,\kappa0=0.02,NL}$) analyses show greater decreases in amplification at periods T < 0.1 s than those for LE analysis, due to the effects of soil nonlinearity.

Figure 7.5 compares F_{760} for LE ($F_{760,I20,\kappa0=0.03,LE}$), EL ($F_{760,I20,\kappa0=0.03,EL}$) and NL ($F_{760,I20,\kappa0=0.03,NL}$) simulations from the Ilhan (2020) branch with scaled D_{min} to capture target $\kappa_0 \approx 0.03$ s. These F_{760} models have amplification peaks that shift from 0.4 s to 2 s and smaller low-period amplification, which is again consistent with deeper profiles. F_{760} from EL ($F_{760,I20,\kappa0=0.03,EL}$) and NL ($F_{760,I20,\kappa0=0.03,NL}$) analyses show decreased amplification at periods T < 3 s, in comparison to LE ($F_{760,I20,\kappa0=0.03,LE}$).

Figure 7.6 shows results of TOK simulations with original D_{min} values from the Campbell (2009) model. The behavior observed for this branch is slightly different compared to the Ilhan (2020) simulations shown in Figure 7.1, as follows:

- The $F_{760,TOK,C,LE}$ shows a slight trough at T ≈ 0.015 s.
- No distinct peak is observed for this branch; however, for 0.04 s < T < 0.1 s, there is an observable increase in amplification.

For EL ($F_{760,TOK,C,EL}$), the trend is consistent with LE ($F_{760,TOK,C,LE}$), with slightly lower amplifications at periods between 0.02 < T < 0.1 s, and slightly higher amplification at periods T > 0.1 s. The F_{760} models developed from NL analysis ($F_{760,TOK,C,NL}$) show clear differences in terms of the level of amplification compared to LE and EL simulations but a similar variation with period. The amplification between periods 0.01 s < T < 0.1 s is considerably lower, most likely related to the effects of nonlinearity which are stronger for NL analysis. At long periods (T > 1 s), the 3 types of analysis converge to small amplification at long periods. In terms of the uncertainties, the standard deviations decrease with increasing periods.

Figure 7.7 shows a similar comparison for the TOK simulations that employ the scaled D_{min} values to capture target κ_0, in this case considering all of the simulations. For this set of simulations, there is a similar trend for the F_{760} for the three types of analysis, compared to the F_{760} models computed from the original D_{min} values, but systematically lower short-period amplification is observed due to the scaling of D_{min} to capture the target κ_0. When compared to the original (unscaled) D_{min} F_{760} models obtained from Ilhan (2020) and TOK simulations, similarities include the amplification trough at T ≈ 0.02 s, peaks near T ≈ 0.1 s, and a transition towards small amplification as period increases for T > 1 s. Differences in the scaled-D_{min} results are in the shape of the F_{760} models for T = 0.05 and 0.1 s.

Figure 7.8 shows TOK F_{760} for the simulations with κ0 = 0.01 s ± 0.005 s; results are shown for the LE ($F_{760,TOK,\kappa0=0.01,LE}$), EL ($F_{760,TOK,\kappa0=0.01,EL}$) and NL ($F_{760,TOK,\kappa0=0.01,NL}$) cases and all results have scaled D_{min}. The results show two distinct amplification peaks, specifically at 0.04 s and 0.2 s. Figure 7.9 and Figure 7.10 similarly show F_{760} models for the simulations with κ_0 = 0.02 s ± 0.005 s and the simulations with κ_0 = 0.03 s ± 0.005 s .The κ_0 ~ 0.02 s case is qualitatively similar to the 0.01 s case, but with lower amplifications at short periods. For the κ_0 ~ 0.03 s case, the amplification peak previously observed at 0.04 s is shifted towards 0.1 s, and the amplification peak at 0.2 s is no-longer present. At periods T < 0.05 s, lower amplification is observed due to higher κ_0 values.

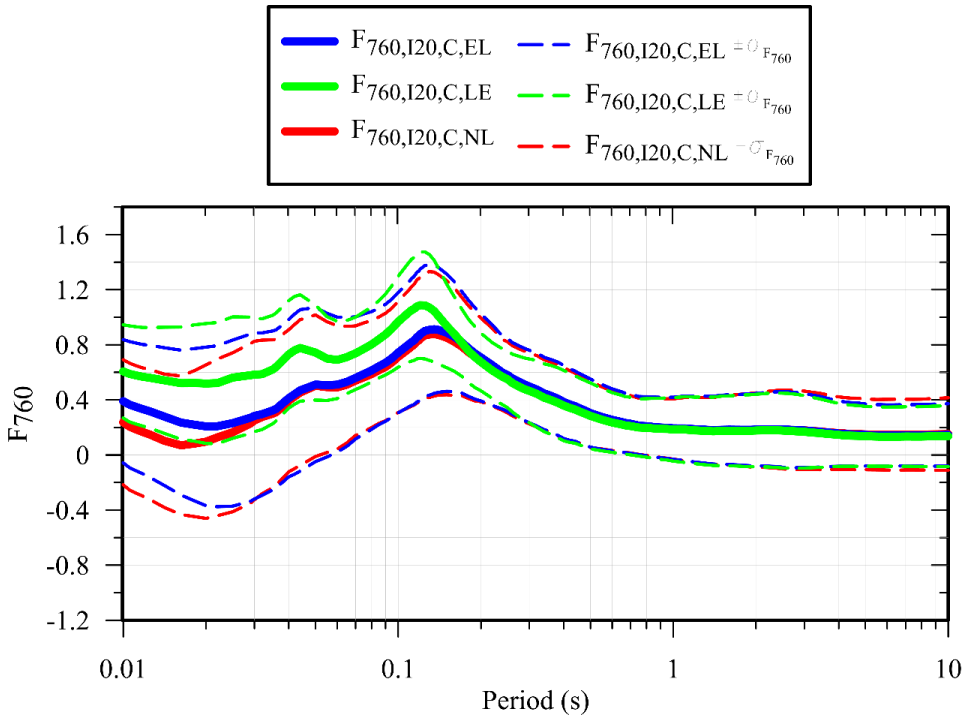

Figure 7.1 F_{760} models from LE, EL, and NL simulations for Ilhan (2020) simulations using the Campbell (2009) D_{min} model.

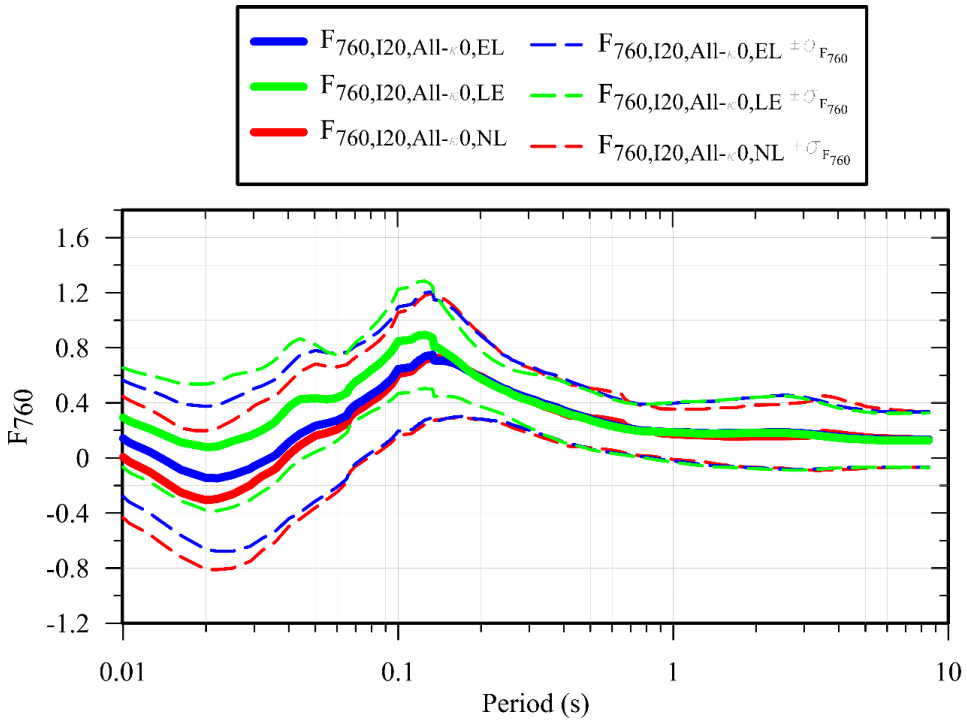

Figure 7.2 F_{760} models from LE, EL, and NL simulations for Ilhan (2020) simulations using scaled D_{min} to capture target κ_0. (All κ_0 values considered)

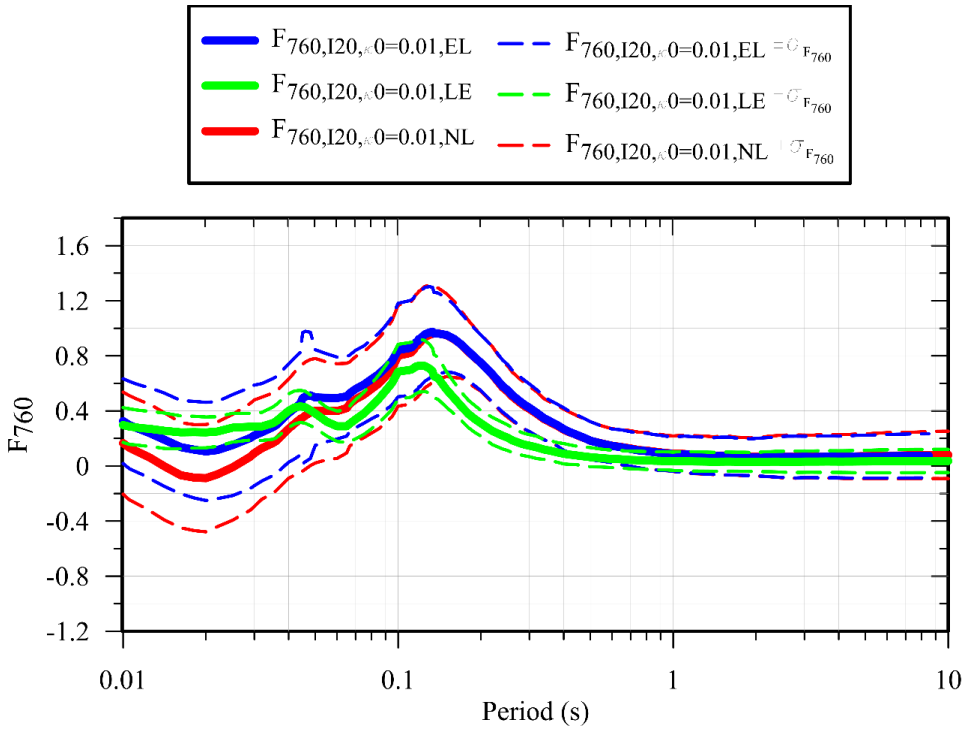

Figure 7.3 F_{760} models from LE, EL, and NL simulations for Ilhan (2020) simulations using scaled Dmin to capture target κ_0. (Only simulations with κ_0 = 0.01 s ± 0.005 s considered)

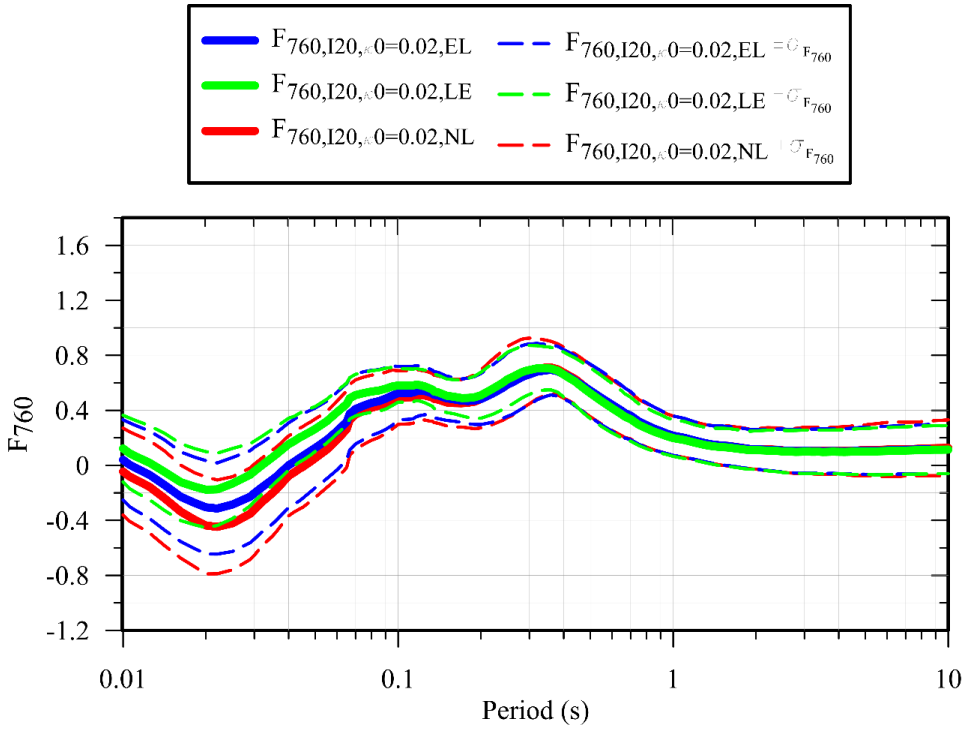

Figure 7.4 F_{760} models from LE, EL, and NL simulations for Ilhan (2020) simulations using scaled D_{min} to capture target κ_0. (Only simulations with κ_0 = 0.02 s ± 0.005 s considered)

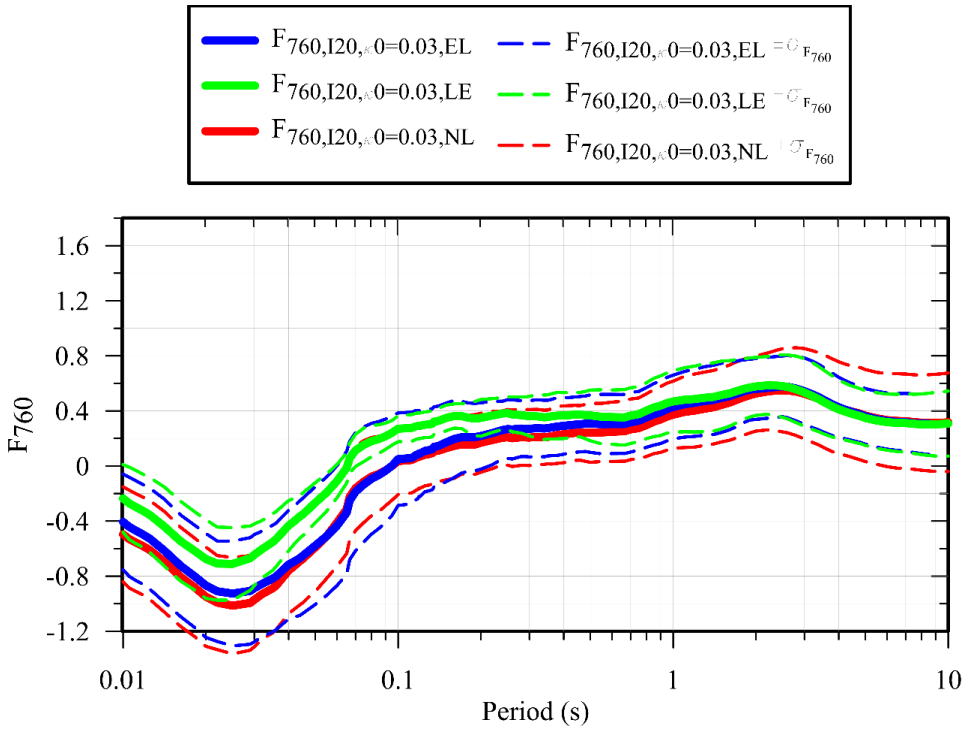

Figure 7.5 F_{760} models from LE, EL, and NL simulations for Ilhan (2020) simulations using scaled D_{min} to capture target κ_0. (Only simulations with κ_0 = 0.03 s ± 0.005 s considered)

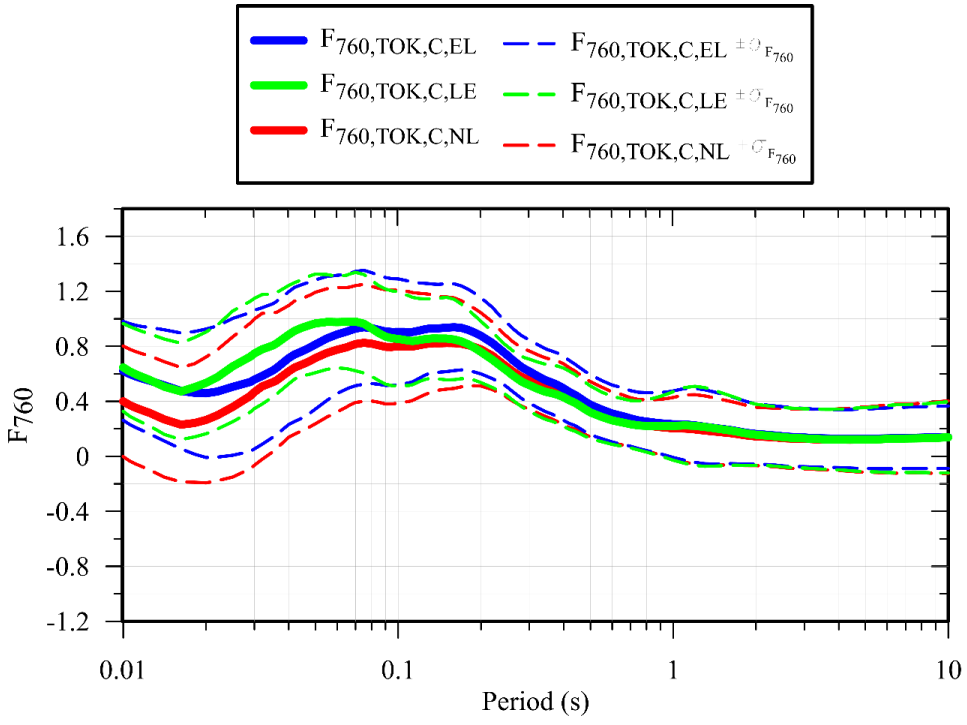

Figure 7.6 F_{760} models from LE, EL, and NL simulations for TOK simulations using Campbell (2009) D_{min} model.

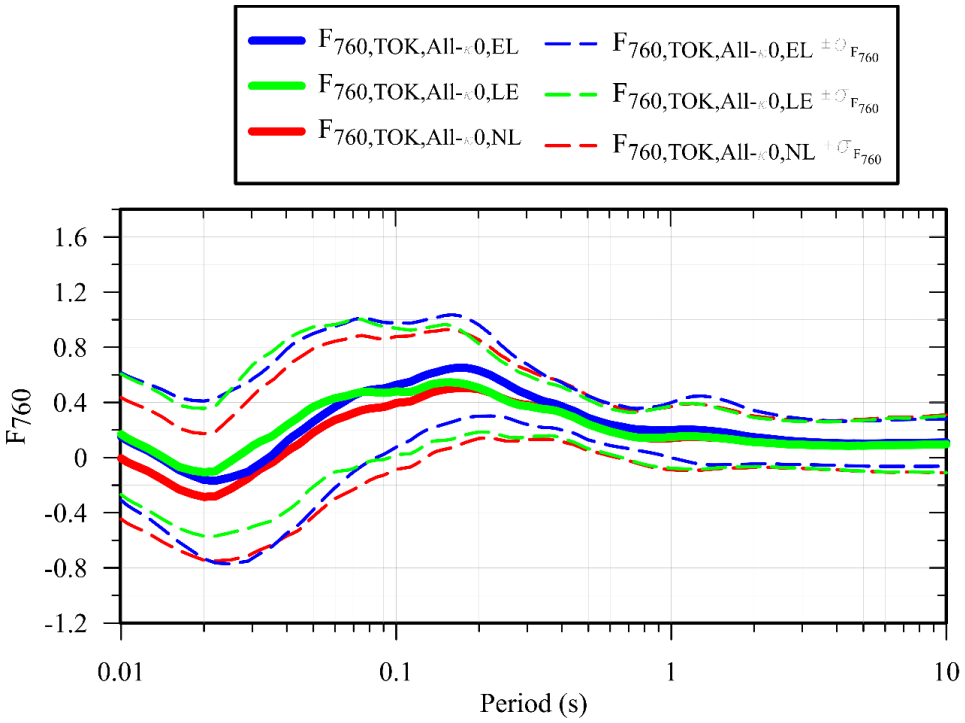

Figure 7.7 F_{760} models from LE, EL, and NL simulations for TOK simulations using scaled D_{min} to capture target κ_0. (All κ_0 values considered)

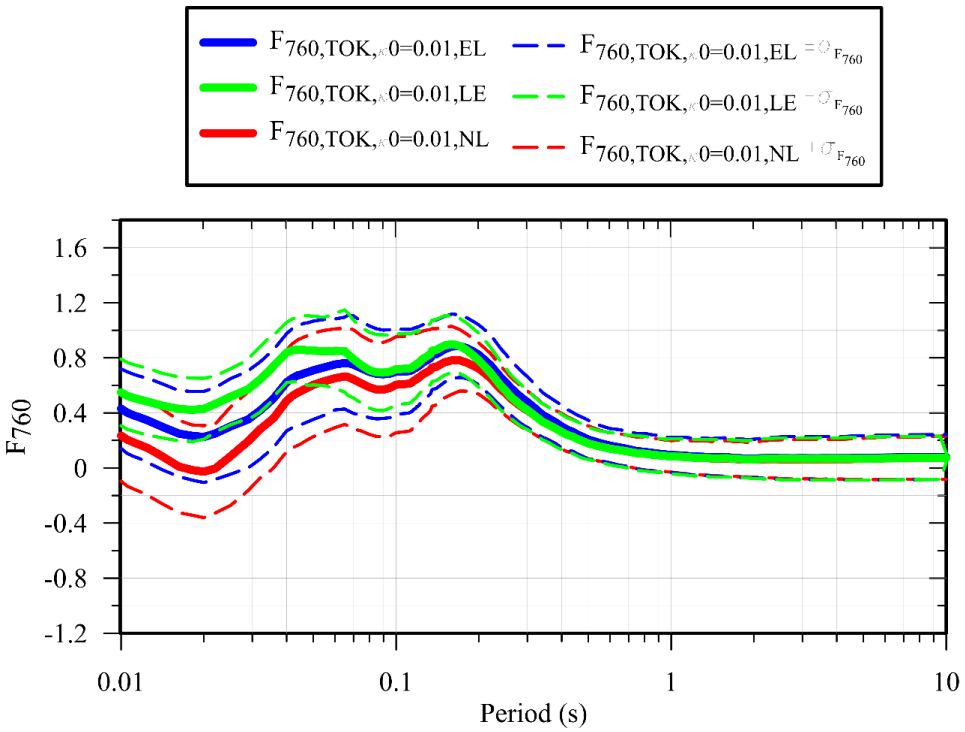

Figure 7.8 F_{760} models from LE, EL, and NL simulations for TOK simulations using scaled D_{min} to capture target κ_0. (Only simulations with κ_0 = 0.01 s ± 0.005 s considered)

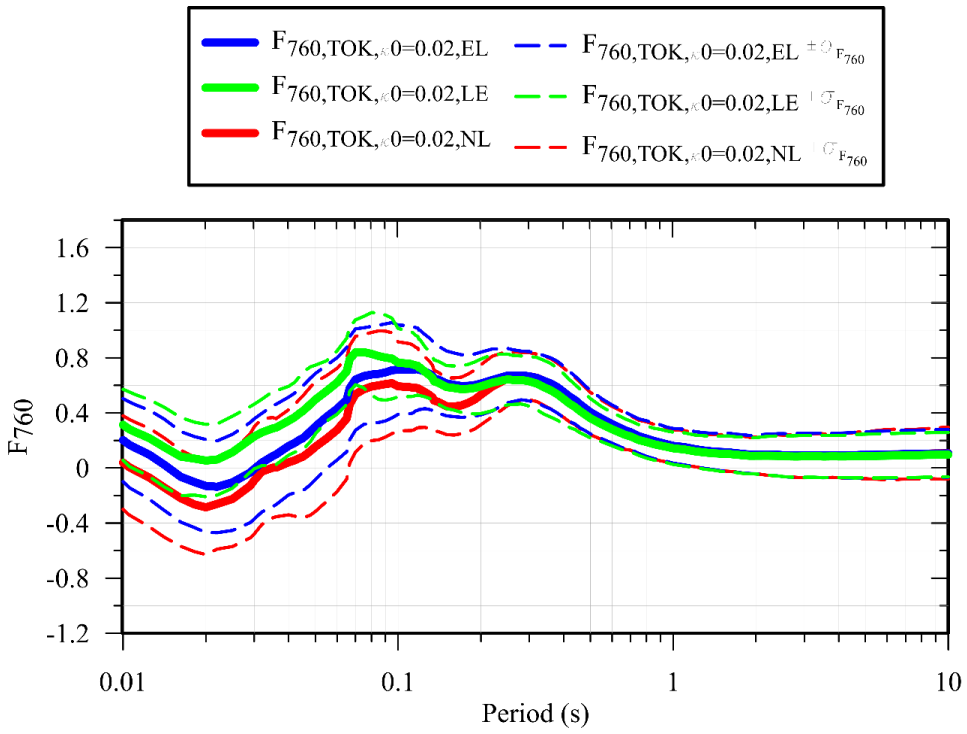

Figure 7.9 F_{760} models from LE, EL, and NL simulations for TOK simulations using scaled D_{min} to capture target κ_0. (Only simulations with κ_0 = 0.02 s ± 0.005 s considered)

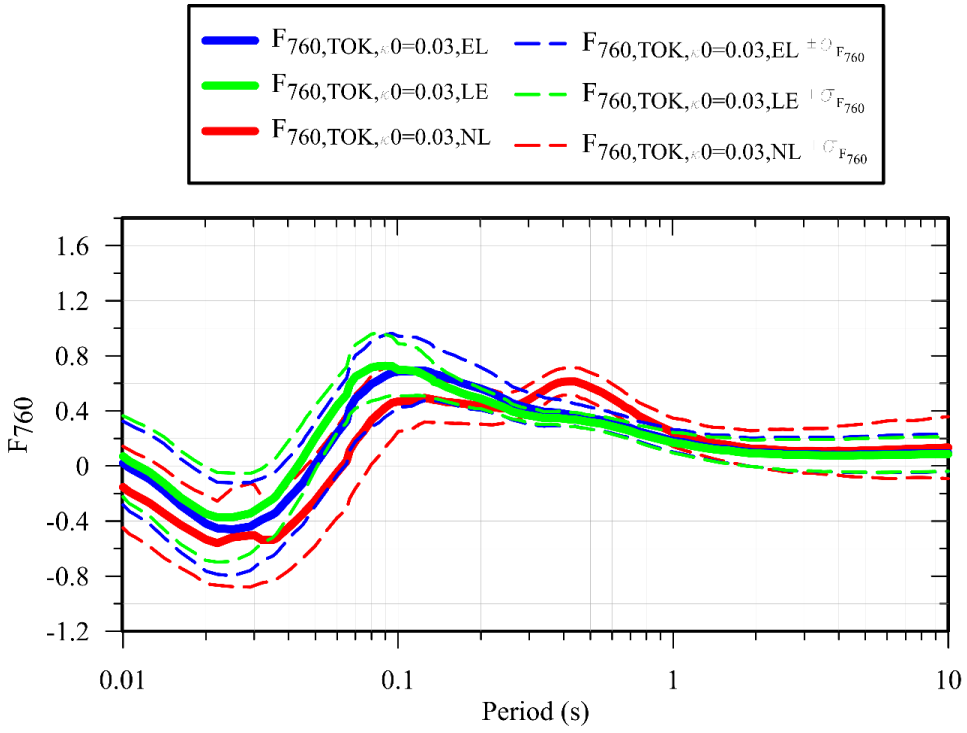

Figure 7.10 F_{760} models from LE, EL, and NL simulations for TOK simulations using scaled D_{min} to capture target κ_0. (Only simulations with κ_0 = 0.03 s ± 0.005 s considered)

7.3 Simulation-based F_{760} models

Based on the different sets of simulations previously discussed, two sets of F_{760} were developed: one based on grouping analyses based on κ_0 values and the other based on grouping analyses based on profile type (i.e., "impedance" vs. "gradient", as defined in Sections 6.3.2 and 6.3.3). For each of these groups, F_{760} models were combined for the different types of analysis (LE, EL, NL) and branches (Ilhan 2020, TOK). To achieve this, the 30 F_{760} models presented in Section 7.2 were grouped into 6 groups.

The first set of F_{760} includes four groups: one based on the unscaled D_{min} values from Campbell (2009), and three based on the scaled D_{min} values for different κ_0 values. For these groups, a weighted average is computed across the F_{760} models for the 3 different types of analysis (LE, EL, NL) and the 2 different branch profile types (Ilhan 2020, TOK) using:

$$F_{760,k} = \sum_{j=1}^{2} \sum_{i=1}^{3} w_i * w_j * F_{760,i,j,k} \quad (7.1)$$

where subscript "k" represents C for the unscaled D_{min} values or the specific κ_0 values of ~0.01 s, 0.02 s, and 0.03 s, subscript "i" represents the three different types of analysis, subscript "j" represents the two branch profile types, and w_i and w_j represent the weights assigned to each analysis or profile.

Similarly, the standard deviations are estimated as:

$$\sigma_{F760,k} = \sum_{j=1}^{2} \sum_{i=1}^{3} w_j * w_i * \sigma_{F760,i,j,k} \quad (7.2)$$

For this study, a weight of 0.4 was given to LE analysis, and 0.3 was given to both EL and NL analysis. These weights can be justified by evaluating the level of strain to which the profiles are subjected. In this study, the approach used in Kim et al. (2016) was used, whereby the strain index computed as the ratio between the Peak Ground Velocity (PGV) and the V_{S30} is calculated. Based on this, over 95% of the simulations, have a strain index values less than 0.1%, justifying the use equal weights to the equivalent linear and nonlinear simulations. Moreover, the level of strain associated with the analyses conducted herein are generally lower than 0.1%, justifying the use of a higher weight to the linear elastic simulations. For the branch profile types, equal weight of 0.5 was used for both the Ilhan (2020) and TOK branches. The resulting four F_{760} models are shown and compared in Figure 7.11. The F_{760} factor corresponding to the original simulations using the D_{min} from Campbell (2009) ($F_{760,C}$) show the highest amplification at periods T < 0.15 s, which can be explained by the lower κ_0 values of this set of simulations. The rest of the F_{760} models show a consistent trend, with increasing κ_0 values, lower amplification at periods T < 0.12 s is observed. The lowest amplification at T < 0.15 s is observed for the simulations with κ_0 ~ 0.03 s. Moreover, an amplification peak can be observed at T ~ 0.15 s for $F_{760,C}$ and $F_{760,\kappa0=0.01}$,whereas for the simulations with higher κ_0 values, the peak is not observed. For longer periods T > 0.2 s, $F_{760,\kappa0=0.03}$ is showing the highest amplification, which is consistent with the fact that higher κ_0 values might also indicate deeper profiles with resonances at higher periods. On the other hand, $F_{760,\kappa0=0.02}$ exhibits its peak at T = 0.3 s. The rest of the F760 show comparable behavior at periods T > 0.2 s.

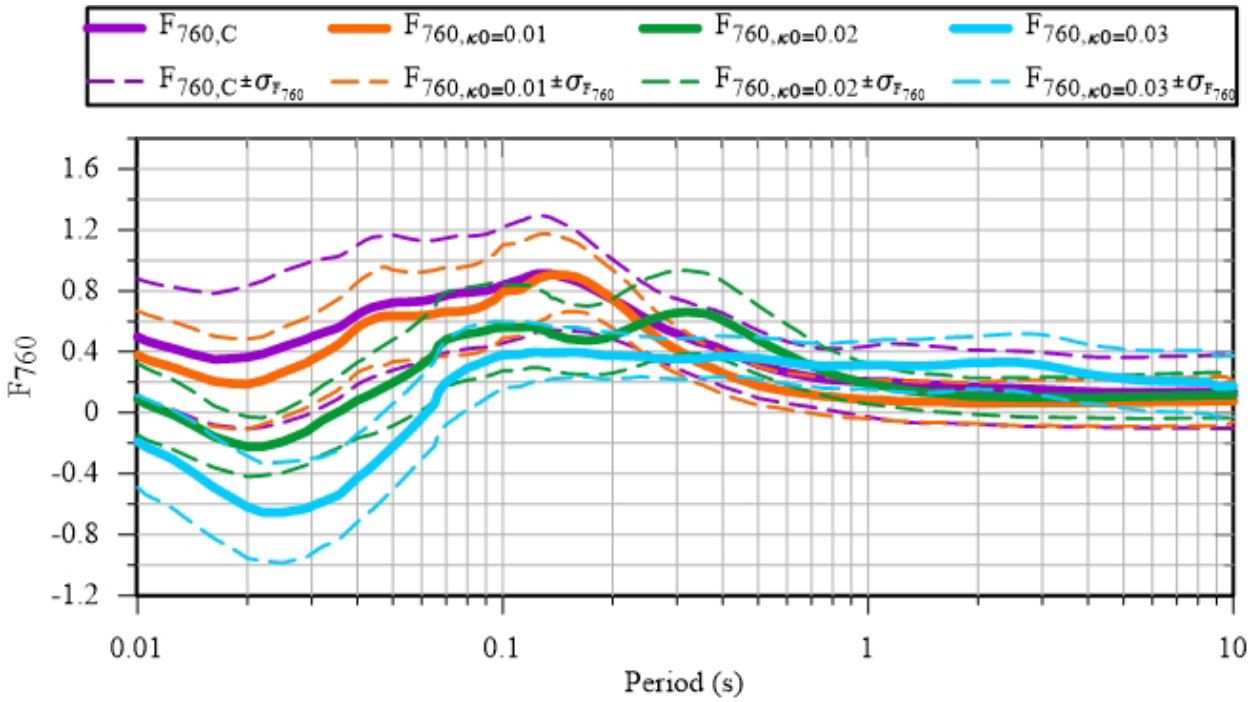

Figure 7.11 F_{760} models for selected κ_0 values

The second set of F_{760} models includes two groups: one for impedance profiles and one for gradient profiles. For these groups, a weighted average is computed across the F_{760} models for the 3 different types of analysis (LE, EL, NL) the 2 different branch profile types (Ilhan 2020, TOK), and the 4 different κ_0 (C, 0.01 s, 0.02 s, and 0.03 s) using:

$$F_{760,v} = \sum_{k=1}^{4}\sum_{j=1}^{2}\sum_{i=1}^{3} w_i * w_j * w_k * F_{760,i,j,k,v} \quad (7.3)$$

where subscript "v" represents impedance or gradient profiles, and subscripts i, j, and k represent analysis type, branch profile type, and κ_0 type, respectively.

Similarly, the standard deviations are estimated as:

$$\sigma_{F760,v} = \sum_{k=1}^{4}\sum_{j=1}^{2}\sum_{i=1}^{3} w_i w_j w_k * \sigma_{F760,i,j,k,v} \quad (7.4)$$

The same weights w_i and w_j are used here, but the new weight w_k is used to combine the results for the different κ_0 values. The weights selected are 0.4 for C (i.e., all unscaled Campbell D_{min} results), 0.3 for simulations with κ_0 ~ 0.02 s, and 0.15 for both simulations with κ_0 ~ 0.01 s and κ_0 ~ 0.03 s. The resulting two F_{760} models are shown in Figure 7.12, along with the impedance and gradient F_{760} models from Stewart et al. (2020).

Figure 7.12a compares the gradient model proposed in the present study against the gradient model proposed in Stewart et al. (2020), which will be referred to as the $SEA20_{GRAD}$ model in this report. In general, there are differences which can be attributed to the differences in the gradient profiles used in Stewart et al. (2020) and the profiles used herein. At short periods T < 0.02 s,

both models give comparable levels of amplification. Between T ≈ 0.025 s and T ≈ 0.30 s, the $F_{760,GRAD}$ suggested in the present study shows significantly slightly higher amplification compared to the $SEA20_{GRAD}$. At periods T > 0.3 s, the SEA20 gradient model shows slightly higher or consistent amplification compared to the $F_{760,GRAD}$ presented herein. These differences might be attributed to the fact that SEA20 used, in general, deeper profiles for its gradient model, namely the profiles from Frankel et al. (1996) and Darragh et al. (2015). Figure 7.12b compares the impedance models from SEA20 and the present study. In this case, $F_{760,IMP}$ and $SEA20_{GRAD}$ appear to be in better agreement throughout the complete range of periods except periods between T ≈ 0.15 s and T ≈ 2 s, where the $F_{760,IMP}$ exhibits higher amplification. In general, differences between SEA20 models and the models proposed herein could be explained by differences in the profiles used to obtain these models.

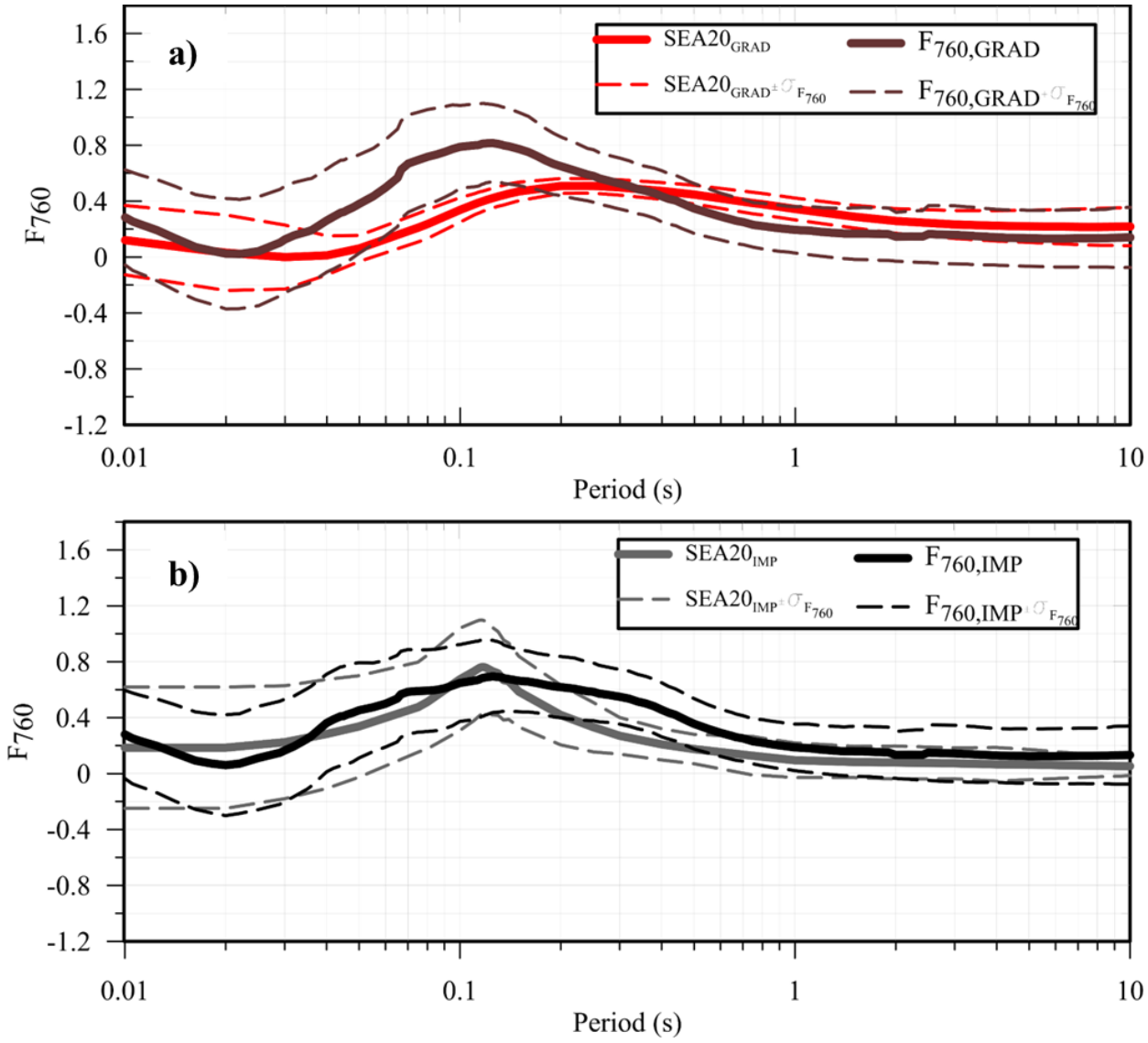

Figure 7.12 F_{760} models for a) Gradient profiles and b) impedance profiles,

8 Summary and Conclusions

8.1 Bias in NGA-East Ground Motion Models

The USGS National Seismic Hazard Model uses hard-rock reference site GMMs from the NGA-East project (Goulet et al., 2021a) and site amplification models recommended by an expert panel (Stewart et al., 2020; Hashash et al., 2020) to estimate ground-motions in CENA. Ultimately, the solution to this incompatibility is the development of new GMMs with compatible site factors. The work presented herein essentially serves as a bridge to those future models, allowing current models to be used with modification so as to remove observed bias.

Using an expanded CENA data set (relative to that used in the NGA-East project), we examine residuals of the recommended GMMs. While expanded, the range of magnitudes in the database remains limited (**M** ~4.0-5.8), hence our focus in this paper was mainly on assessments of model bias within the range of the data, rather than scaling relationships (e.g., changed of ground motions with magnitude) that are also important for hazard applications). Using the central branch GMM, these residuals analyses indicate that for data outside of the TOK region, there is no evidence for bias in the magnitude- and distance-scaling components of the GMM for **M** > 4 events and R_{rup} < 600 km, except for faster attenuation in the Gulf Coast region that manifests at distances > 300 km. However, persistent period-dependent bias is observed from the model-to-data comparisons for a wide range of alternate NGA-East GMMs and alternate data selection criteria (i.e., excluding data from selected regions). This bias is towards overprediction at short periods and underprediction at long periods.

We anticipate that these biases are associated with both the hard-rock GMMs and the F_{760} factors, although the breakdown of bias contributions among these models is uncertain. For forward applications for commonly encountered site conditions in the range of the F_V model (200 to 2000 m/s), we recommend to apply the bias and its uncertainties to the sum of the hard-rock GMM and site response. The levels of uncertainty to be used depend on how the PSHA is conducted, as follows:

1. For PSHA in which all 17 NGA-East GMMs are used (such as in the 2023 NSHM), the smoothed bias should be used with the epistemic uncertainty given in Table 1 as $\sigma_{e,\,data}$.
2. For PSHA in which only the central branch GMM is used, the smoothed bias should be used with the uncertainty given in Table 1 as σ_e.

For applications where nonlinear site response is expected (i.e., the F_{nl} term in Eq. 1 is non-zero), the PGA term that drives the nonlinearity should be modified by the PGA bias term.

For applications in which only the hard-rock GMMs are to be applied, contributions to the bias from the site factors (F_{lin} in Eq. 2) should be removed. The amount of this adjustment is uncertain, and will depend on how models for F_{760} evolve in future work. Increases in F_{760} at long periods, and decreases at short periods, which seem likely based on recent results shown in Figure 13, would reduce the bias. For these hard-rock applications, we suggest the use of a logic tree in which different fractions of the smoothed bias are attributed to the hard-rock GMM. Logic tree

branches in which the full bias, various percentages of the full bias, and no bias are applied are recommended. Weights given to these branches would be guided by the degree to which the bias can be attributed to the Sea20 F_{760} model, particularly for impedance conditions.

8.2 Ground Motion Model Adjustments for Texas, Oklahoma, and Kansas

To evaluate potential bias in the NGA-East median model, we created a database for ground motion recordings in Texas, Oklahoma, and Kansas for natural and potentially induced earthquakes and developed a GMM for the study region using the newly available data. The reference empirical approach (Atkinson 2008) is utilized where residuals between the observed data and the ground motion intensity prediction from the NGA-East weighted median GMM were used to develop adjustment factors to correct for overall bias, magnitude, distance, and site effects. The developed GMM is applicable to moment magnitudes M_w from 3.5 to 5.8, and rupture distance up to 500km, as represented by the dataset.

The overall bias adjustment factor C_{adj} developed in this study is interpreted to represent both overall differences in the TOK data relative to the NGA-East median GMM, but also the site amplification relative to $V_{S30} = 3000$ m/s, F_{760}. The negative values of the empirical C_{adj} factors at short periods (< 0.1 s) indicates appear to represent the F_{760} effects associated with a larger κ_0, although these empirically derived values are more negative than the simulation-based F_{760}. The C_{adj} factors at periods between T = 0.15 and 0.5 s are consistent with the simulation-based F_{760}, but at longer periods the C_{adj} factors are much larger than the simulation-based F_{760}. The source of these large values of C_{adj} at long periods is not fully understood.

We compared the GMM developed from this study with existing GMMs models for the CENA region, including the weighted median NGA-East GMM (Goulet et al. 2021a) and ZR19 (Zalachoris and Rathje 2019). The GMM from this study compares well with the ZR19 model and the predictions match well with the observed ground motions. The F_V site amplification model derived in this study relative to $V_{S30} = 760$ m/s compares well with to the site amplification model from Parker et al. (2019), suggesting similar F_V site amplification effects for TOK and the broader CENA region.

8.3 Simulation-based F_{760} Models

A suite of 30 simulation-based F_{760} models was developed based on linear elastic frequency-domain, equivalent linear, and nonlinear 1D site response analysis using (1) generic site profiles developed as part of a large-scale parametric study for CENA and (2) measured profiles at sites in Texas, Oklahoma, and Kansas (TOK) regions. From the first set of profiles, only those with V_{S30} values between 700-800 m/s were selected to develop F_{760} models, and from the second set, the V_{S30} range was selected between 600-900 m/s. For each set of profiles, two values of κ_0 are considered, a) Original κ_0 (generally < 0.01 s), and b) 0.01 s< κ_0 <0.05 s. A total of 6 F_{760} weighted models are then developed as follows:

- The first set is dependent on κ_0 conditions, from which four F_{760} models (original κ_0, $\kappa_0 \approx$ 0.01 s, $\kappa_0 \approx$ 0.02 s, $\kappa_0 \approx$ 0.03 s) are proposed. In general, the increase in κ_0 leads to lower

F_{760} at short periods (< 0.1 s) due to the cumulative damping effect, but higher F_{760} are observed for mid-to-long periods (> 0.1 s) mainly due to contributions from deeper profiles. The opposite behavior is applicable in the case of decreasing κ_0 values. In terms of the uncertainties associated with the F_{760}, a decrease in standard deviations is generally observed as period increases.

- The second set of F_{760} models are developed for impedance or gradient conditions ($F_{760,GRAD}$, $F_{760,IMP}$). The $F_{760,GRAD}$ and $F_{760,IMP}$ are compared with those from previous published models (i.e., $SEA20_{GRAD}$ and $SEA20_{IMP}$). For the short periods (< 0.02 s), $SEA20_{GRAD}$ and $F_{760,GRAD}$ seem to be consistent, but from T ≈ 0.025 s to T ≈ 0.45 s, the $SEA20_{GRAD}$ model exhibits significantly lower levels of amplification compared to $F_{760,GRAD}$. Additionally, at longer periods (> 0.5 s), $F_{760,GRAD}$ shows lower amplification at long periods (> 0.5 s) compared to previously published gradient model. For the impedance model, similar behavior is observed between $SEA20_{IMP}$ and $F_{760,IMP}$ models except for slight differences at periods between T ≈ 0.15 s and T ≈ 2 s, where the $SEA20_{IMP}$ exhibits lower amplification.

It should be noted that the variations between the models presented in this study and those from SEA20 may arise from differences in the velocity profile attributes and the criteria employed to categorize profiles as either impedance or gradient.

9 References

Afshari K, & Stewart JP (2015). Uncertainty of site amplification derived from ground response analysis. *Proc. 6th Int. Conf. Earthquake Geotech. Eng.*, Christchurch, New Zealand, Paper No. 227 (electronic file).

Afshari K, & Stewart, JP (2019). Insights from California vertical arrays on the effectiveness of ground response analysis with alternative damping models. *Bulletin of the Seismological Society of America*, 109(4), 1250-1264.

Agaiby SS & Mayne PW (2015). Relationship between undrained shear strength and shear wave velocity for clays. In *6th Symp. on Deformation Characteristics of Geomaterials* (pp. 358-365). IOS Press, Argentina.

Anderson JG & Hough SE (1984). A model for the shape of the Fourier amplitude spectrum of acceleration at high frequencies. *Bulletin of the Seismological Society of America*, 74(5), 1969-1993.

Atik LA, Gregor NJ, Abrahamson NA, Kottke AR (2022). GMPE-consistent hard-rock site adjustment factors for Western North America. *Earthquake Spectra*. 38(4), 2371-2397.

Atkinson, G (2008). Ground-motion prediction equations for eastern North America from a referenced empirical approach: Implications for epistemic uncertainty, *Bulletin of the Seismological Society of America*, 98, 1304–1318.

Atkinson GM (2012). Evaluation of attenuation models for the northeastern United States/southeastern Canada, *Seismol. Res. Let.*, 83, 166–178.

Bates D, Maechler M, Bolker B, and Walker S (2015). Fitting linear mixed-effects models using lme4. *Journal of Statistic Software*, 67, 1–48.

Banker K (2011). MongoDB in action. Manning Publications Co

Boore, DM (1983). Stochastic simulation of high-frequency ground motions based on seismological models of the radiated spectra. *Bulletin of the Seismological Society of America*, 73(6A), 1865-1894.

Boore, DM (2003). Simulation of ground motion using the stochastic method. *Pure and Applied Geophysics*, 160, 635-676.

Boore DM (2010). Orientation-independent, nongeometric-mean measures of seismic intensity from two horizontal components of motion. *Bulletin of the Seismological Society of America* 100(4), 1830–1835.

Boore DM (2015). Adjusting ground-motion intensity measures to a reference site for which V_{S30} = 3000 m/s, *PEER Report 2015/06*, Pacific Earthquake Engineering Research Center, UC Berkeley (headquarters).

Boore DM (2018). Ground-motion models for very-hard-rock sites in eastern North America: An update, *Seismol. Res. Lett.* 89, 1172-1184.

Boore DM (2020). Revision of Boore (2018) Ground-motion predictions for central and eastern North America: Path and offset adjustments and extension to 200 m/s < V_{S30} < 3000 m/s, *Seismol. Res. Lett.* 91, 977-991.

Boore DM and Campbell KW (2017). Adjusting central and eastern North America ground-motion intensity measures between sites with different reference-rock site conditions, *Bull. Seismol. Soc. Am.* 107, 132-148.

Boore DM, Stewart JP, Seyhan E, and Atkinson GM (2014). NGA-West 2 equations for predicting response spectral accelerations for shallow crustal earthquakes. *Earthquake Spectra* 30.

Boyd OS, Churchwell D, Moschetti MP, Thompson EM, Chapman MC, Ilhan O, Pratt TL, Ahdi SK and Rezaeian S (2023) Sediment Thickness Map of Atlantic and Gulf Coastal Plain Strata, Central and Eastern U.S., and Their Influence on Earthquake Ground Motions, *Earthquake Spectra*. Accepted

Brandenberg SJ, & Yang Y (2021). 'ucla_geotech_tools: A set of Python packages developed by the UCLA geotechnical group' (Version 1.0.2) [Computer software]. https://doi.org/10.5281/zenodo.5621169.

Buckreis TE, Nweke CC, Wang P, Brandenberg SJ, Mazzoni S and Stewart JP (2023a). Relational database for California strong ground motions, Geo-Congress 2023: Geotechnical Data Analysis and Computation, Los Angeles, CA, March 2023, *Geotechnical Special Publication No. 342*, EM Rathje, B Montoya, and MH Wayne (Eds.), 461-470, ASCE Geo-Institute

Buckreis TE, Stewart JP, Brandenberg SJ, Wang P (2023b). Subregional anelastic attenuation model for California, *Bull. Seismol. Soc. Am.,* https://doi.org/10.1785/0120220173..

Budnitz RJ, Apostolakis G, Boore DM, Cluff LS, Coppersmith KJ, Cornell CA and Morris PA (1997). Recommendations for probabilistic seismic hazard analysis: Guidance on uncertainty and use of experts, US Nuclear Regulatory Commission, *Report NUREG/CR-6372*.

Campbell KW (2003). Prediction of strong ground motion using the hybrid empirical method and its use in the development of ground-motion (attenuation) relations in eastern North America, *Bull. Seismol. Soc. Am.* 93, 1012–1033.

Campbell KW (2009). Estimates of shear-wave Q and κ 0 for unconsolidated and semiconsolidated sediments in Eastern North America. Bulletin of the Seismological Society of America, 99(4), 2365-2392.

Chapman MC and Guo Z (2021). A response spectral ratio model to account for amplification and attenuation effects in the Atlantic and Gulf Coastal Plain. *Bull Seismol Soc Am*, 111, 1849–1867.

Chiou BS-J, and Youngs RR (2008) NGA model for average horizontal component of peak ground motion and response spectra. Report no. 2008/09, November. Berkeley, CA: Pacific Earthquake Engineering Research Center (PEER), November 2008. UC Berkeley.

Coleman JL, and Cahan SM (2012). Preliminary catalog of the sedimentary basins of the United States, USGS Open-File Report 2012–1111, U.S. Geological Survey, available at http://pubs.usgs.gov/of/2012/1111/ (last accessed 1 June 2017).

Contreras V, Stewart JP, Kishida T, Darragh RB, Chiou BSJ, Mazzoni S, Youngs RR, Kuehn NM, Ahdi SK, Wooddell K, Boroschek R, Rojas F and Ordenes J (2022). NGA-Sub source and path database. *Earthquake Spectra*, 38, 799-840.

Darragh RB, Abrahamson NA, Silva WJ, and Gregor N (2015). Development of hard rock ground-motion models for Region 2 of Central and Eastern North America, *PEER Report No. 2015/04*, Pacific Earthquake Engineering Research Center, University of California, Berkeley, CA, pp. 51–69.

Darendeli, MB (2001). Development of a new family of normalized modulus reduction and material damping curves. The University of Texas at Austin.

Douglas J, Boore DM (2011). High-frequency filtering of strong-motion records. *Bull Earthquake Eng* 9, 395–409 https://doi.org/10.1007/s10518-010-9208-4

Dreiling J, Isken MP, Mooney WD, Chapman MC, and Godbee RW (2014). NGA-East regionalization report: Comparison of four crustal regions within central and eastern North America using waveform modeling and 5%-damped pseudo-spectral acce leration response, *PEER Report 2014/15*, Pacific Earthquake Engineering Research Center, UC Berkeley (headquarters).

EPRI (2013): EPRI (2004, 2006) Ground-Motion Model Review Project: Shear Wave Velocity Measurements at Seismic Recording Stations in the Central and Eastern United States. EPRI, Palo Alto, CA: 2012. EPP43952/C19088.

Frankel AD, Mueller CS, Barnhard T, Perkins D, Leyendecker EV, Hanson S and Hopper M (1996). National seismic hazard maps: Documentation. *Open-file report no. 96-532*. U.S. Geological Survey, Reston, VA.

Goulet CA, Kishida T, Cramer CH, Darragh RB, Silva WJ, Hashash YMA, Harmon J, Stewart JP, Wooddell KE and Youngs RR (2014). PEER NGA-East Database, *Report 2014/17*, Pacific Earthquake Engineering Research Center, UC Berkeley (headquarters).

Goulet CA, Bozorgnia Y, Kuehn N, Al Atik L, Youngs RR, Graves RW and Atkinson GM (2021a). NGA-East Ground-Motion Characterization model part I : Summary of products and model development. *Earthquake Spectra*, 37, 1231–1282.

Goulet CA, Kishida T, Ancheta TD, Cramer CH, Darragh RB, Silva WJ, Hashash YMA, Harmon J, Parker GA, Stewart JP and Youngs RR (2021b). PEER NGA-East database, *Earthquake Spectra*, 37, 1331-1353.

Graizer V (2015). Ground-motion prediction equations for the central and eastern United States, *PEER Report No. 2015/04*, Pacific Earthquake Engineering Research Center, University of California, Berkeley, CA, pp. 51–69.

Groholski DR, Hashash YMA, Kim B, Musgrove M, Harmon J, & Stewart, JP (2016). Simplified model for small-strain nonlinearity and strength in 1D seismic site response analysis. *Journal of Geotechnical and Geoenvironmental Engineering*, 142(9), 04016042.

Guo Z, Chapman MC (2019). An examination of amplification and attenuation effects in the Atlantic and Gulf Coastal Plain using spectral ratios. *Bull Seismol Soc Am*, 109, 1855–1877

Harmon J, Hashash YMA, Stewart JP, Rathje EM, Campbell KW, Silva WJ, Xi B and Ilhan O (2019a). Site amplification functions for Central and Eastern North America – Part I: Simulation data set development. *Earthquake Spectra*, 35, 787–814.

Harmon J, Hashash YMA, Stewart JP, Rathje EM, Campbell KW, Silva WJ and Ilhan O (2019b). Site amplification functions for Central and Eastern North America – Part II: Modular simulation-based models. *Earthquake Spectra*, 35, 815–847.

Hashash YMA, Kottke AR, Stewart JP, Campbell KW, Kim B, Moss C, Nikolaou S, Rathje EM, and Silva WJ (2014). Reference rock site condition for Central and Eastern North America. *Bull Seismol Soc Am*, 104, 684–701.

Hashash YMA, Ilhan O, Harmon JA, Parker GA, Stewart JP, Rathje EM, Campbell KW and Silva WJ (2020). Nonlinear site amplification model for ergodic seismic hazard analysis in Central and Eastern North America. *Earthquake Spectra*, 36, 69–86.

Hassani B, and Atkinson GM (2015). Referenced empirical ground-motion model for eastern North America, Seismological Research Letters 86, 477–491.

Hearne M, Thompson EM, Schovanec H, Rekoske J, Aagaard BT and Worden CB (2019). USGS automated ground motion processing software, USGS Software Release, doi: 10.5066/P9ANQXN3.

Kishida T, Darragh RB, Chiou BS, Bozorgnia Y, Mazzoni S, Contreras V, Boroschek R, Rojas F and Stewart JP (2020). Chapter 3: Ground Motions and Intensity Measures, in Data Resources for NGA-Subduction Project, *PEER Report 2020/02*, J.P. Stewart (editor), Pacific Earthquake Engineering Research Center, University of California, Berkeley, California (headquarters).

Hough SE & Anderson JG (1988). High-frequency spectra observed at Anza, California: implications for Q structure. Bulletin of the Seismological Society of America, 78(2), 692-707.

Ilhan O (2020). Conventional and deep learning-based site amplification models for central and eastern North America (Doctoral dissertation).

Kramer, SL (1996). *Geotechnical Earthquake Engineering*. Pearson Education India.

Ktenidou OJ, Abrahamson NA (2016). Empirical estimation of high-frequency ground motion on hard rock. Seismol. Res. Lett., 87(6), 1465–1478.

Kwak DY, Ahdi SK, Wang P, Zimmaro P, Brandenberg SJ, Stewart JP (2021). Web portal for shear wave velocity and HVSR databases in support of site response research and applications. UCLA Geotechnical Engineering Group. DOI:10.21222/C27H0V

Lanzo G & Vucetic M (1999). Effect of soil plasticity on damping ratio at small cyclic strains. *Soils and Foundations*, 39(4), 131-141.

Leonard M (2014). Self-consistent earthquake fault-scaling relations: Update and extension to stable continental strike-slip faults. Bull. Seismol. Soc. Am., 104, 2953–2965.

Li M, Rathje EM, Cox BR, Yust M (2022). A Texas-specific V_{S30} map incorporating geology and V_{S30} observations. Earthquake Spectra. 38(1). 521-542.

Li M, Ramos-Sepulveda ME, Brandenberg S, Stewart JP, Rathje EM (2023) "2023 Texas, Oklahoma, and Kansas Dataset for Investigating NGA-East GMM and Site Amplification Models." DesignSafe-CI. https://doi.org/10.17603/ds2-nadf-h758

Mendoza C, Turner J, & O'Connell D (2017). Ground motion characterization and site-specific IMASW Vs-Depth measurements at CEUS seismic stations: The 2011 Prague, OK earthquake. US Geol. Survey Earthquake Hazards Program Final Tech. Rep. G17AP00021.

Moschetti MP, Aagaard BT, Ahdi SK, Altekruse JM, Boyd OS, Frankel AD, Herrick JA, Petersen MD, Powers PM, Rezaeian S, Shumway AM, Smith J, Stephenson WJ, Thompson EM, Withers KB (2023). The 2023 U.S. National Seismic Hazard Model: Ground-motion characterization for conterminous U.S., *Earthquake Spectra*, accepted

Moschetti MP, Thompson EM, Powers PM, Hoover SM, and McNamara DE (2019). Ground motions from induced earthquakes in Oklahoma and Kansas. *Seismol. Res. Lett.*, 90(1), 160-170.

Nuclear Regulatory Commission (2012). Practical implementation guidelines for SSHAC Level 3 and 4 Hazard Studies. Nuclear Regulatory Commission, Office of Nuclear Regulatory Research, *Report NUREG/CR-2117*.

Parker GA, Harmon JA, Stewart JP, Hashash YMA, Kottke AR, Rathje EM, Silva WJ, and Campbell KW (2017). Proxy-based V_{S30} estimation in central and eastern North America. *Bull. Seismol. Soc. Am.* 107, 117–131.

Parker GA, Stewart JP, Hashash YMA, Rathje EM, Campbell KW and Silva WJ (2019). Empirical linear seismic site amplification in Central and Eastern North America, *Earthquake Spectra*, 35, 849–881.

Pacific Earthquake Engineering Research Center (2015) NGA-East: Median ground-motion models for the Central and Eastern North America region. Pacific Earthquake Engineering Research Center, *PEER Report No. 2015/04*, April.

Petersen MD, Shumway AM, Powers PM, Muller CS, Moschetti MP, Rezaeian S, McNamara D, Luco N, Boyd OS, Rukstales KS, Jaiswal KS, Thompson EM, Hoover SM, Clayton BS, Field EH and Zeng Y (2020). The 2018 update of the US National Seismic Hazard Model: Overview of model and implications. *Earthq Spectra*, 36, 5–41.

Pezeshk S, Zandieh A and Haji-Soltani A (2021). A ground motion model for the Gulf Coast Region of the United States. *Bull. Seismol. Soc. Am.* 111, 3261–3277.

Pratt TL and Schleicher LS (2021). Characterizing ground-motion amplification by extensive flat-lying sediments: The seismic response of the eastern U.S. Atlantic Coastal Plain strata. *Bull. Seismol. Soc. Am.*, 111, 1795–1823.

RCoreTeam (2019). R: A Language and Environment for Statistical Computing. vol. ISBN 3-900.

Ramos-Sepulveda ME, Parker GA, Li M, Ilhan O, Hashash YMA, Rathje EM, Stewart JP (2022). Performance of NGA-East GMMs and site amplification models relative to CENA ground motions, *12th National Conference on Earthquake Engineering*, EERI, Salt Lake City, UT, Jun 27 - Jul 1, 2022 (electronic file)

Ramos-Sepulveda ME, Parker GA, Thompson EM, Brandenberg SJ, Li M, Ilhan O, Hashash YMA, Rathje EM and Stewart JP (2023a). High-pass corner frequency selection for implementation in the USGS automated ground-motion processing tool, Geo-Congress 2023: Geotechnical Data Analysis and Computation, Los Angeles, CA, March 2023, *Geotechnical Special Publication No. 342*, EM Rathje, B Montoya, and MH Wayne (Eds.), 327-335, ASCE Geo-Institute

Ramos-Sepulveda ME, Buckreis TE, Li M, Parker GA, Brandenberg SJ, Rathje EM, Stewart. JP (2023b). 2023 NGA-compatible CENA database for GMM validation and site response studies, DesignSafe-CI. https://doi.org/10.17603/ds2-ywqs-sp29

Ramos-Sepúlveda ME, JP Stewart, GA Parker, MP Moschetti, EM Thompson, SJ Brandenberg, YMA Hashash, EM Rathje (2023c). Bias of NGA-East ground-motion and site amplification models relative to Central and Eastern North America ground-motion database, *Earthquake Spectra*, in review.

Rezaeian S, Powers PM, Shumway AM, Petersen MD, Luco N, Frankel AD, et al. (2021). The 2018 update of the US National Seismic Hazard Model: Ground motion models in the central and eastern US. *Earthquake Spectra*, 37, 1354-1390.

Schleicher LS and Pratt TL (2021). Characterizing fundamental resonance peaks on flat-lying sediments using multiple spectral ratio methods: An example from the Atlantic Coastal Plain, Eastern United States. *Bull. Seismol. Soc. Am.* 111, 1824–1848.

Seabold, S., & Perktold, J. (2010). statsmodels: Econometric and statistical modeling with python. In 9th Python in Science Conference.

Seyhan E and Stewart JP (2014) Semi-empirical nonlinear Site amplification from NGA-West2 data and simulations. *Earthquake Spectra*, 30, 1241–1256.

Silva WJ, Gregor N, Darragh RB and Abrahamson NA (2015) Development of hard rock ground-motion models for region 2 of central and eastern North America. *Report PEER 2015/04201504*. Pacific Earthquake Engineering Research Center, University of California.

Stanzione D, Barth B, Gaffney N, Gaither K, Hempel C, Minyard T, ... & Teller AP (2017). Stampede 2: The evolution of an xsede supercomputer. In *Proceedings of the Practice and Experience in Advanced Research Computing 2017 on Sustainability, Success and Impact* (pp. 1-8).

Stephenson WJ, Odum JK, Hartzell SH, Leeds AL, & Williams RA (2021). Shear-wave velocity site characterization in Oklahoma from joint inversion of multimethod surface seismic measurements: Implications for central US ground-motion prediction. *Bulletin of the Seismological Society of America*, 111(4), 1693-1712.

Stewart JP, Parker GA, Atkinson GM, Boore DM, Hashash YMA and Silva WJ (2020). Ergodic site amplification model for Central and Eastern North America. *Earthquake Spectra*, 36, 42–68.

Terzaghi K, Peck RB, & Mesri G (1996). *Soil Mechanics in Engineering Practice*. John wiley & sons.

Tiwari A (2018) Engineering ground motion characteristics and site characterization for earthquakes in Texas. Master's Thesis, Department of Civil Engineering, University of Texas at Austin, Austin, TX.

Xu B, Rathje, EM, Hashash YMA, Stewart J, Campbell KW, & Silva WJ (2020). κ 0 for soil sites: Observations from Kik-net sites and their use in constraining small-strain damping profiles for site response analysis. *Earthquake Spectra*, 36(1), 111-137.

Yenier E, and Atkinson GM (2015). Regionally adjustable generic ground-motion prediction equation based on equivalent point source simulations: Application to central and eastern North America, *Bulletin of the Seismological Society of America* 105, 1989–2009.

Youngs RR, Goulet CA, Bozorgnia Y, Kuehn N, Al Atik L, Graves RW and Atkinson GM (2021). NGA-East ground-motion characterization model part II: Implementation and hazard implications. *Earthquake Spectra*, 37,1283-1330.

Yust M (2018) Dynamic site characterization of TexNet ground motion stations. Master's Thesis, Department of Civil Engineering, University of Texas at Austin, Austin, TX.

Zalachoris G and EM Rathje (2017) Ground motion models for earthquake events in Texas, Oklahoma, and Kansas, 3rd International Conference on Performance Based Design in Earthquake Geotechnical Engineering, Vancouver, BC, Canada

Zalachoris G, Rathje EM. (2019) Ground Motion Model for Small-to-Moderate Earthquakes in Texas, Oklahoma, and Kansas. *Earthquake Spectra*. 35(1), 1-20.

Zalachoris G, He J and Rathje EM (2020) Earthquake time series from events in Texas, Oklahoma, and Kansas. DesignSafe-CI. https://doi.org/10.17603/ds2-v310-qc53

Zalachoris G, Rathje EM and Paine JG (2017) V_{S30} characterization of Texas, Oklahoma, and Kansas using the P-wave seismogram method. *Earthquake Spectra* 33, 943–961.